Design, Modeling and Control of Vibration Systems with Electromagnetic Energy Harvesters and their Application to Vehicle Suspensions

Yilun Liu

Dissertation submitted to the faculty of the Virginia Polytechnic Institute and State University in partial fulfillment of the requirements for the degree of

Doctor of Philosophy
In
Mechanical Engineering

Lei Zuo (Chair)
Robert G. Parker
Corina Sandu
John B. Ferris
Khai D. T. Ngo

09/30/2016
Blacksburg, VA

Keywords: Vibration control, Semi-active suspension control, Energy harvesting, Electromagnetic damper, Mechanical motion rectifier (MMR)

Design, Modeling and Control of Vibration Systems with Electromagnetic Energy Harvesters and their Application to Vehicle Suspensions

Yilun Liu

ABSTRACT

Vibration has been a serious concern in many vibration systems, such as vehicle suspensions, tall buildings, long-span bridges, etc. For instance, it is well recognized that large vibration induced by road roughness will cause discomfort of vehicle occupants and deteriorate vehicles' road handling. In order to mitigate the vibration, large amount of vibration energy is converted to wasted heat by conventional viscous dampers in most vibration systems. Instead of dissipating vibration energy into heat waste via viscous damping elements, this dissertation proposes an innovative vibration control method which can simultaneously mitigate vibration and harvest the associated vibration energy by using electromagnetic energy harvesters.

Through theoretical and experimental studies, this dissertation proves that the electromagnetic energy harvester can act as a constant viscous damper when connected to a proper electrical load. Its effectiveness in vibration mitigation has been experimentally demonstrated using a small-scale dual-mass vibration system with a linear electromagnetic energy harvester. Furthermore, this dissertation shows that the electromagnetic energy harvester can also work as a controllable damper. The semi-active control of a linear electromagnetic energy harvester, for improvement of suspension performance, has been experimentally implemented in a scaled-down quarter-car suspension system. While improving performance, power produced by the harvester can be harvested through energy harvesting circuits.

This dissertation also proposes a mechanical-motion-rectifier(MMR)-based electromagnetic energy harvester using a ball-screw mechanism and two one-way clutches for the application of replacing the viscous damper in vehicle suspensions. Compared to commercial linear harvesters, the proposed design is able to provide large damping forces and increase power-dissipation density, making it suitable to vehicle suspensions. In addition, the proposed MMR-based harvester can convert reciprocating vibration into unidirectional rotation of the generator. This feature significantly increases energy-harvesting efficiency by enabling the generator to rotate

at a relatively steady speed during irregular vibrations and improves the system reliability by reducing impact forces among transmission gears. Extensive theoretical and experimental analysis have been conducted to characterize the proposed MMR-based energy harvester. The coupled dynamics of the suspension system with the MMR-based energy harvester are also explored and optimized. Furthermore, a new control algorithm is proposed to control the MMR-based energy harvester considering its unique dynamics induced by the one-way clutches. The results show that the controlled proposed electromagnetic energy harvester can possibly improve ride comfort of vehicles over conventional oil dampers and simultaneously harvest the associated vibration energy.

Design, Modeling and Control of Vibration Systems with Electromagnetic Energy Harvesters and their Application to Vehicle Suspensions

Yilun Liu

GENERAL AUDIENCE ABSTRACT

Instead of dissipating vibration energy into heat waste via viscous damping elements, this dissertation proposes an innovative vibration control method which can simultaneously mitigate vibration and harvest the associated vibration energy using electromagnetic energy harvesters. This dissertation shows that the electromagnetic energy harvester can work as a controllable damper as well as an energy harvester. The semi-active control of a linear electromagnetic energy harvester, for improvement of suspension performance, has been experimentally implemented in a scaled-down quarter-car suspension system. While improving performance, power produced by the harvester can be harvested through energy harvesting circuits.

This dissertation also proposes a mechanical-motion-rectifier(MMR)-based electromagnetic energy harvester using a ball-screw mechanism and two one-way clutches for the application of replacing the viscous damper in vehicle suspensions. Compared to commercial linear harvesters, the proposed design is able to provide large damping forces and increase power-dissipation density, making it suitable to vehicle suspensions. In addition, the proposed MMR-based harvester can convert reciprocating vibration into unidirectional rotation of the generator. This feature significantly increases energy-harvesting efficiency by enabling the generator to rotate at a relatively steady speed during irregular vibrations and improves the system reliability by reducing impact forces among transmission gears. Extensive theoretical and experimental analysis have been conducted to characterize the proposed MMR-based energy harvester. The coupled dynamics of the suspension system with the MMR-based energy harvester are also explored and optimized. Furthermore, a new control algorithm is proposed to control the MMR-based energy harvester considering its unique dynamics induced by the one-way clutches. The results show that the controlled proposed electromagnetic energy harvester can possibly improve ride comfort of vehicles over conventional oil dampers and simultaneously harvest the associated vibration energy.

Acknowledgments

I would like to express my sincere gratitude to everyone who helped, supported me in this endeavor. Without them, I won't be able to accomplish this work.

I would like to give great thanks to my advisor, Professor Lei Zuo. It is my luck to have Professor Zuo as my advisor. He has been giving me valuable instructions and guidance, which greatly helps me in the process of this project. His talent and encouragement amaze me and drive me to convey my enthusiasm to work on the project. His creativity and his attitude to work also influence me on my work and life.

I also would like to thank Professor Robert Parker, Professor Corina Sandu, Professor John Ferris and Professor Khai Ngo for serving on my dissertation committee. Their comments, ideas and suggestions have been very helpful for my research and significantly improved the quality of my dissertation.

I also gratefully acknowledge the funding support from Virginia Commonwealth Research Commercialization Fund (CRCF) and Ford Motor Company.

Next, I propose my appreciation to my lab mates, Xiudong Tang, Wanlu Zhou, You Wu, Yalu Pei, Sijing Guo, Yu Pan, Tim Cerilli, Jackson Klein, Jason Parker, Peng Li, Changwei Liang and Xiaofan Li, for providing help and technical discussions. Especially, thanks to Dr. Lin Xu for his help on the collaboration and experiment preparation. In addition, thanks to Bill Songer for parts machining.

At last, I want to give my deepest thanks to my parents, Liu, Dongbo and Yuan, Shiying, and my girlfriend, Yan Cao. Their support and devotion make my life better.

Sincerely

Contents

List of figures

List of tables

Nomenclature

A	The amplitude of sinusoid excitations [m]
c_1	Dissipative damping in dual-mass vibration systems $[\mathrm{N/(m/s)}]$
c_e	Equivalent damping of the engaged MMR-based energy harvester$[\mathrm{N/(m/s)}]$
c_{min}	Minimum damping of a semi-active damper $[\mathrm{N/(m/s)}]$
c_{max}	Maximum damping of a semi-active damper$[\mathrm{N/(m/s)}]$
c_m	Equivalent torsional damping of the generator $[\mathrm{Nm/(rad/s)}]$
c_n	Nominal constant damping of a suspension system $[\mathrm{N/(m/s)}]$
c_v	Viscous damping of the generator $[\mathrm{Nm/(rad/s))}]$
$c(t)$	Adjustable damping of a semi-active damper $[\mathrm{N/(m/s)}]$
C	Total capacitance of the circuit [F]
d_m	Screw diameter [mm]
e_{EMF}	Induced voltage of an electromagnetic generator [V]
f	Ball-screw friction factor
f_1	Mechanical tuning ratio in a dual-mass vibration system
$f_{crossover}$	Crossover frequency [Hz]
f_e	Electrical tuning ratio in a dual-mass vibration system
f_{EMF}	Electromagnetic force of an electromagnetic generator [N]
F_e	The force of the engaged MMR-based energy harvester [N]
F_d	The force of the disengaged MMR-based energy harvester [N]
F_w	External wind loads [N]
g	Gravitational acceleration [m/s^2]
G_r	Road-roughness coefficient
J_{bg}	Screw inertia [$\mathrm{kgcm^2}$]
J_{lg}	Large gear inertia [$\mathrm{kgcm^2}$]
J_m	Generator inertia [$\mathrm{kgcm^2}$]
J_{sg}	Small gear inertia [$\mathrm{kgcm^2}$]
k_1	Stiffness of the vibration absorber $[\mathrm{N/m}]$

k_e	Generator voltage constant [V/rads]
k_f	Force constant of the electromagnetic transducer [N/A]
k_s	Stiffness of the primary structure [N/m]
k_t	Generator torque constant [Nm/A]
k_u	Equivalent stiffness of the tire [N/m]
k_v	Voltage constant of the electromagnetic transducer [V/(m/s)]
K_s	Suspension stiffness of the MMR-based suspension system [N/m]
K_{us}	Equivalent tire stiffness of the MMR-based suspension system [N/m]
l	Ball-screw lead [mm]
L	Total inductance of an electromagnetic transducer [H]
L_i	External inductance of an electromagnetic transducer [H]
m_1	The mass of vibration absorber [kg]
m_e	Equivalent inertance of the engaged MMR-based energy harvester [kg]
m_s	The mass of primary structure or car body [kg]
m_u	The mass of unsprung mass in a 2DOF suspension system [kg]
M_s	Mass of the sprung mass of the MMR-based suspension system [kg]
M_{us}	Mass of the unsprung mass of the MMR-based suspension system [kg]
$\dot{q}$	Electrical current inside the coil [A]
r_b	MMR bevel gear transmission ratio
r_g	Generator gearhead ratio
R	Total resistance of an electromagnetic transducer [Ω]
R_e	External resistance of an electromagnetic transducer [Ω]
R_i	Coil resistance of an electromagnetic transducer [Ω]
S_0	Degree of road roughness $[m^2/(cycle/m)]$
S_{F}	Uniform power spectrum density of the white-noise input force
T_s	Sampling interval [s]
V	Vehicle moving velocity [m/s]
V_{sb}	Rolling over speed bump [m/s]
x_1	Displacements of the primary structure [m]
x_s	Displacements of the vibration absorber [m]

$\ddot{x}_g$	Ground acceleration [m/s^2]
z_0	Road displacements disturbance of the MMR-based suspension system [m]
z_1	Displacements of unsprung mass of the MMR-based suspension system [m]
z_2	Displacements of sprung mass of the MMR-based suspension system [m]
z_r	Road displacement roughness [m]
z_s	Displacement of the sprung mass [m]
z_{su}	Suspension displacement [m]
z_u	Displacement of the unsprung mass [m]
α	Excitation frequency ratio
β	Semi-active dampers' response rate
ζ_e	Damping ratio
θ	Angular displacement of the generator [Rad/s]
θ_{in}	Input rotational speed of the MMR-based energy harvester [Rad/s]
μ	Mechanical mass ratio in a dual-mass vibration system
μ_k	Electromagnetic mechanical coupling coefficient
ρ	Scaled-down factor
τ_0	Coulomb friction torque of the generator [Nm]
τ_{bs}	Torque of the screw shaft [Nm]
τ_{emf}	Torque caused by electrical damping of the three-phase generator [Nm]
τ_{fric}	Friction torque the three-phase generator [Nm]
τ_{lg}	Torque of the large gear [Nm]
τ_m	Input mechanical torque of the generator [Nm]
τ_{sg}	Torque of the small gear [Nm]
v_0	Reference spatial frequency [$cycle/m$]
ω_e	Resonant frequency of the circuit [Rad/s]

Publications

Journal Articles:

[1] **Liu, Y.** and Zuo, L., "Mixed Skyhook and PDD: A New Low-jerk Semi-active Suspension Control Based on Power Flow Analysis," *Journal of Dynamic Systems, Measurement, and Control, ASME Transaction on,* vol. 138, no. 8, pp.081009, 2016.

[2] **Liu, Y.** and Zuo, L., "A Computation-efficient Framework for the Integrated Design of Structural and Control Systems," *Journal of Dynamic Systems, Measurement, and Control, ASME Transaction on,* vol. 138, no. 9, pp.091001, 2016.

[3] **Liu, Y.**, Zuo, L., Lin, C.C., and Parker, J., "Exact H_2 Optimal Tuning and Experimental Verification of Energy-harvesting Series Electromagnetic Tuned-mass Dampers," *Journal of Vibration and Acoustics, ASME Transaction on*, vol. 138, no. 6, pp.061003, 2016.

[4] Guo, S., **Liu, Y.**, Xu, L., Guo, X., Zuo, L., "Performance Evaluation and Parameter Sensitivity of Energy-Harvesting Shock Absorbers on Different Vehicles," *Vehicle System Dynamics*, vol. 54, no. 7, pp.918-942, 2016.

[5] Tang, X., **Liu, Y.**, Cui, W., and Zuo, L., "Analytical Solutions to H_2 and H_∞ Optimizations of Resonant Shunted Electromagnetic Tuned Mass Damper and Vibration Energy Harvester," *Journal of Vibration and Acoustics*, vol. 138, no.1, p.011018, 2016.

[6] **Liu, Y.**, Xu, L., Zuo, L., "Design, Modeling and Experimental Characterization of a Mechanical-Motion-Rectifier(MMR)-based Energy-harvesting Shock Absorber Using a Ball-screw Mechanism," *IEEE Transaction on Mechatronics*, Revision under review, 2016.

[7] Guo, S., Xu, L., **Liu, Y.**, Guo, X. and Zuo, L., "Modeling and Experiments of a Hydraulic Electromagnetic Energy-harvesting Shock Absorber," *IEEE Transaction on Mechatronics*, Submitted, 2016.

Peer-reviewed Conference Proceedings:

[1] **Liu, Y.**, Zuo, L. and Tang, X., Regenerative Vibration Control of Tall Buildings Using Model Predictive Control. *ASME Dynamic Systems and Control Conference (DSCC)*, pp. V001T15A012-V001T15A012, 2013.

[2] **Liu, Y.** and Zuo, L., Energy-flow-driven (EFD) semi-active suspension control. *IEEE/ASME American Control Conference (ACC)*, pp. 2120-2125, 2014.

[3] **Liu, Y.**, Lin, C.C. and Zuo, L., Evaluation and optimum design of dual-functional electromagnetic tuned mass dampers, *the 12th International Conference on Motion and Vibration Control (MOVIC)*, 2014.

[4] **Liu, Y.** and Zuo, L., Integrating Structure and Controller Design to Mechanical Systems via Decentralized Control Techniques. *ASME Dynamic Systems and Control Conference (DSCC), pp. V002T25A003-V002T25A003*. 2015.

[5] Xu, L., **Liu, Y.**, Guo, S., Guo, X. and Zuo, L., Damping Characteristics of a Hydraulic Electric Rectifier Shock Absorber and its Effect on Vehicle Dynamics. *ASME International Design Engineering Technical Conferences and Computers and Information in Engineering Conference (IDETC)*, pp. V003T01A009-V003T01A009, 2015.

[6] Guo, S., Xu, L., **Liu, Y.**, Guo, X. and Zuo, L., Performances of Energy-Harvesting Shock Absorbers on Various Types of Vehicles. *ASME Dynamic Systems and Control Conference (DSCC)*, pp. V002T36A004-V002T36A004, 2015.

[7] **Liu, Y.**, Lin, X., Zuo, L., Design, modelling and experimental characterization of a novel energy-harvesting shock absorber with a ball-screw-based mechanical motion rectifier, *the 14th International Conference on Motion and Vibration Control (MOVIC)*, 2016.

[8] **Liu, Y.,** and Zuo, L., Review of Mechanical System Design via Decentralized Control Techniques, *International Symposium on Flexible Automation (ISFA)*, 2016.

[9] Guo, S., Xu, L., **Liu, Y.,** Liu, M., Guo, X. and Zuo, L., Modeling, Experiments, and Parameter Sensitivity Analysis of Hydraulic Electromagnetic Shock Absorber, *ASME International Design Engineering Technical Conferences (IDETC)*, 2016.

Design Patents:

[1] Zuo, L., Lin, X., Wu, Y., **Liu, Y.**, Ocean Wave Energy Harvester Using Mechanical Modified Rectifier, Serial Number: 62/311,985, 2016

1 Introduction

1.1 Background

Vibration has been a serious concern in most vibration systems, such as tall buildings, vehicle suspension systems, long-span bridges, etc. For instance, the structures and secondary components of tall buildings can be quickly damaged by huge dynamic loadings from winds or earthquakes, which also cause discomfort to its human occupants, whose symptoms range from anxiety, fear to dizziness, headaches, and nausea [1]. In 1972 wind-induced vibration caused more than 65 panels of window glass, weighing 500 pounds each, to fall and crash on the sidewalks hundreds of feet below the Hancock Tower in Boston [2]. Figure 1.1 shows the picture taken after the incident where the missing glasses can be clearly seen.

Figure 1.1 Wind induced vibration causes the fall of window glass on Hancock Tower [2]

Another example of vibration systems is the large vibration induced by road roughness when vehicles are running on roads. Actually only 10-16% of fuel energy burned by engines is used to drive vehicles. Besides the thermal inefficiency of engines, one important mechanism of energy loss in automobiles is the dissipation of kinetic energy during vehicle vibration and motion. Moreover, the vibration induced by road irregularities will also cause discomfort of vehicle occupants and deteriorate vehicles' road handling. Figure 1.2 shows the vehicle energy loss for combined city/highway driving [3].

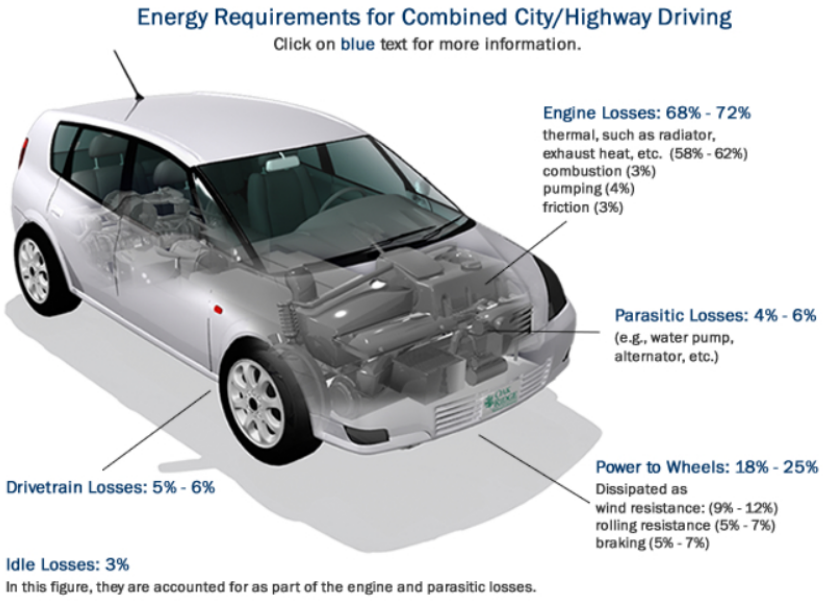

Figure 1.2 Vehicle energy loss for combined city/highway driving [3]

Suspensions play an important role in mitigating vehicles' vibration to achieve increased ride comfort and enhanced road handling. Passive, active, and semi-active suspension systems have been investigated in various vehicles in the past several decades. Among them, semi-active suspension with adjustable damping was introduced in 1970s and is able to provide better trade-offs between performances and costs than passive or active suspensions. After first proposed by Karnopp et al. in 1974 [4], the semi-active suspension has been widely studied in academia and automotive industries as a means to improve ride comfort and road holding of vehicles. In order to mitigate the vibration and improve ride comfort, many semi-active control algorithms, including Sky-Hook (SH) [5], Acceleration-Driven-Damper (ADD) [6] and the mixed SH and ADD (SH-ADD) [7], have been proposed to reduce the acceleration of the sprung mass, while some algorithms also try to lower the jerk of the sprung mass, such as Power-Driven-Damper (PDD) [8] and No-Jerk Skyhook [9]. In addition to ride comfort, road holding oriented methods have also been proposed, such as Ground-Hook (GH) [10]. There are also many modern control methods in which both ride comfort and road holding are considered as a trade-off by adding different weights on them, such as clipped-optimal (LQ-clip) [11], hybrid Model Predictive Control (hMPC) [12] and Linear Parameter Varying (LPV) [13].

On the other hand, large amount of vibration energy is converted to wasted heat by the oil damper in conventional suspensions, which decrease the fuel efficiency of vehicles. In order to improve ride performances and save the above wasted energy, a new type of suspensions, energy-harvesting regenerative suspensions, has been proposed in the past two decades [14-28]. The idea is to harvest energy from suspension vibration while using the harvested energy to implement the suspension control. As a result, the energy-harvesting suspensions are able to improve fuel efficiency by 2-4% [29] through harvesting the kinetic energy otherwise dissipated by the traditional shock absorbers and achieve increased ride performances through the self-powered semi-active suspension control.

Various energy-harvesting regenerative shock absorbers are designed and developed, which can be generally classified into three main categories: linear regenerative electromagnetic shock absorbers (LESAs) [14-20], rotary regenerative electromagnetic shock absorbers (RESAs) [21-25], and MMR-based regenerative electromagnetic shock absorbers (MMRSAs) [26-28]. The linear electromagnetic shock absorbers have a set of voice coils moving in an array of magnetic fields and produce a back electromotive force (EMF) attenuating the suspension vibration. However, their energy-harvesting efficiency is generally high, but power density is too small. For instance, the linear energy-harvesting shock absorber proposed in [20] can achieve 70% - 78% energy-harvesting efficiency, but it can only provide a damping of 940 Ns/m under a short circuit condition, which is even not sufficient for a compact-size passenger car.

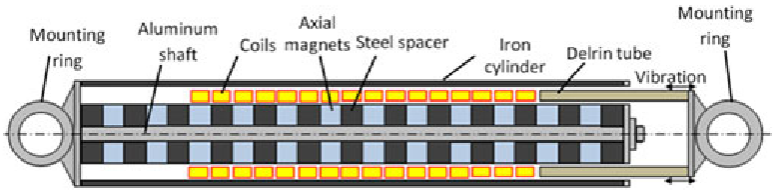

Figure 1.3 Diagram of linear electromagnetic shock absorber [20]

To overcome low-damping drawbacks, rotary energy-harvesting shock absorbers have been proposed, which utilize some mechanisms, such as ball-screw mechanism [21-23], rack-pinion mechanism [24] or some other motion conversion mechanisms [25], to transfer reciprocating linear vibration into bi-directional rotation of rotary generators to produce electricity. Due to converting low-speed linear motion into high-speed rotation, the power density and damping of rotary energy

harvesters are significantly increased. However, the irregular oscillation of the motion transmission mechanism in rotary energy harvesters causes numerous problems such as low efficiency and bad vibration performance due to large impact forces. For example, the rack-pinion rotary energy-harvesting shock absorber investigated in [24] has a good power density and damping range of 1800Ns/m – 8000Ns/m, but it also has large backlash which leads to a relatively low energy-harvesting efficiency 33% - 56%. Figure 1.4 shows three types of RESAs.

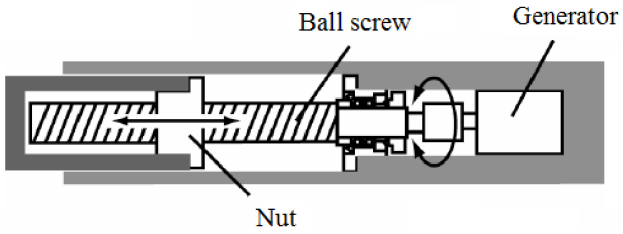

(a)

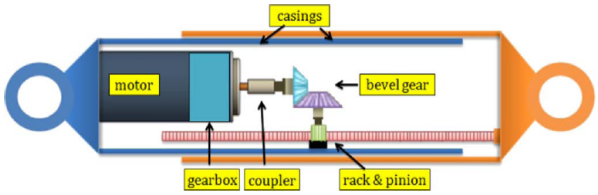

(b)

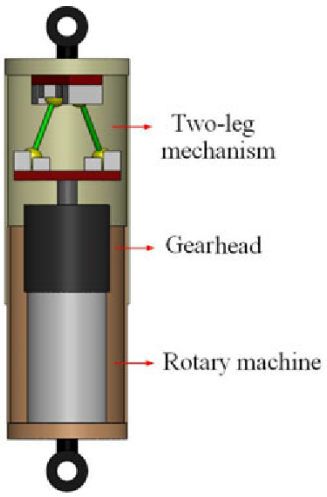

(c)

Figure 1.4 Rotary regenerative electromagnetic shock absorbers (a) Using ball-screw mechanism [21] (b) Using Rack-and-pinion mechanism [24] (c) Using two-leg motion conversion mechanism [25]

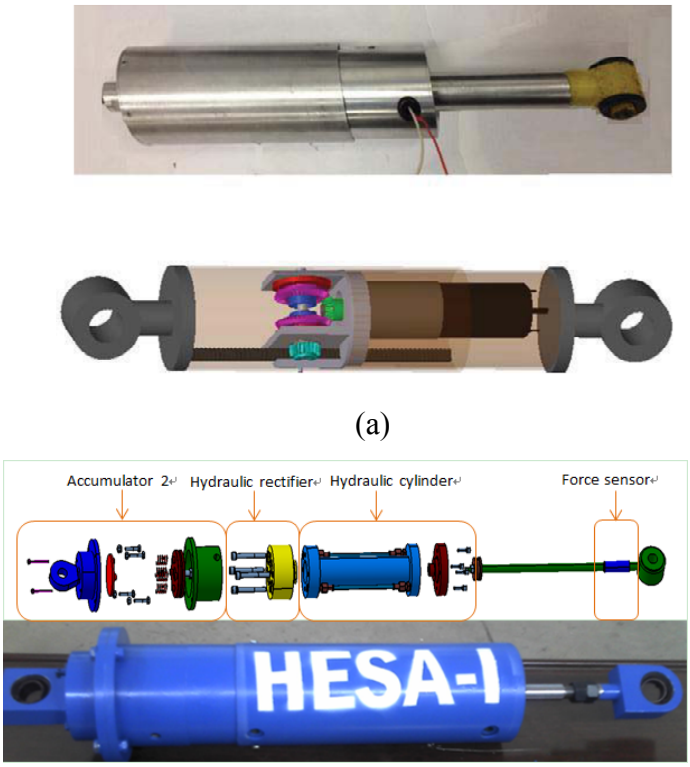

(a)

(b)

Figure 1.5 MMR-based regenerative electromagnetic shock absorbers (a) Using rack-and-pinion based MMR [26] (b) Using hydraulic MMR [27]

MMR-based regenerative electromagnetic shock absorbers (MMRSAs) have been newly developed to convert reciprocating linear vibration into the unidirectional rotation of generators and produce a stable voltage with small ripples. Compared to RESAs, MMR-based design has demonstrated many superior characteristics. The unidirectional operation of the system reduces impact force and thus increases the durability of the system. Recently, hydraulic MMRSAs have been proposed [27-28], in which the suspension vibration drives a hydraulic pump which pushes high-pressure hydraulic oil to drive a hydraulic motor then rotates an electric generator. One-way check valves have been used to convert the up-and-down suspension vibration into unidirectional rotation of the generator. However, similar as the hydraulic active suspensions, it suffers from the huge efficiency loss due to the large friction caused by pipes and valves. Very recently, Li *et al* [26] developed a rack-pinion-based MMR shock absorber, which converts the reciprocating suspension vibration into a regular unidirectional rotation of a generator by using rack-pinion and

bevel gears with embedded one-way roller clutches. It increases the energy harvesting efficiency over hydraulic MMRSAs, whose energy harvesting efficiency is increased to around 60%. However, backlash still exists in the system due to the reciprocating motion between the rack and pinion. This backlash decreases the energy-harvesting efficiency when the shock absorber is subjected small high-frequency vibration, which corresponds to the vehicles driving on the flat highways. In addition, racks and pinions are difficult to be aligned, some of the rack teeth were broken during the short periods of the testing. Moreover, the racks are hard to seal, which resulted in an exposed gear transmission system. This significantly reduces the transmission durability and efficiency. Figure 1.5 shows the two types of MMR-based regenerative electromagnetic shock absorbers.

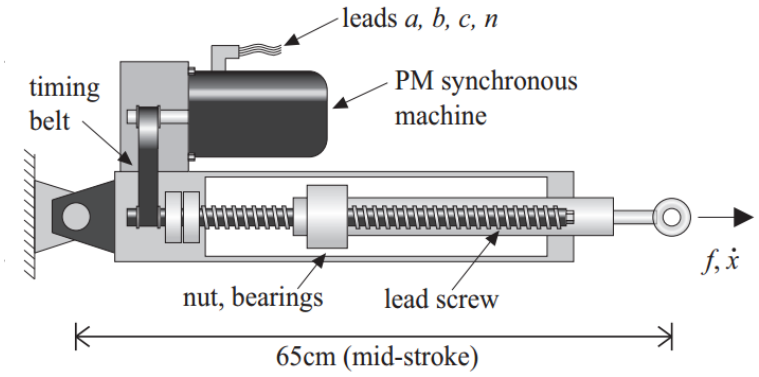

Figure 1.6 Rotary regenerative electromagnetic dampers in the application of civil structures [23]

During the development of various regenerative electromagnetic shock absorbers applied to automotive engineering, regenerative electromagnetic dampers are also proposed to simultaneously mitigate vibration and harvest energy in other vibration systems, such as the rotary regenerative electromagnetic dampers in tall buildings [23]. Figure 1.6 shows the rotary regenerative electromagnetic dampers for tall buildings.

Although many types of regenerative electromagnetic shock absorbers or dampers have been developed for various vibration systems, including vehicle suspension systems, tall buildings, etc., the research on the coupled dynamics of the primary vibration system with the regenerative electromagnetic shock absorber (damper) is still limited. Therefore, the overall dynamics of the primary vibration system with the regenerative electromagnetic shock absorber (damper) is still

unclear, which restricts this new promising technology from practical implementation. Moreover, the regenerative electromagnetic shock absorber (damper) can work as a controllable damper as well as an energy harvester [24]. The research about the control of the regenerative electromagnetic shock absorber (damper) in improving the dynamics of the primary vibration systems is also important but not explored yet.

1.2 Objectives and Contributions of the Dissertation

The objectives of the dissertation are listed below:

1. Analyze and optimize the coupled dynamics of the primary vibration system with the regenerative electromagnetic dampers. Experimentally verify the feasibilities of using regenerative electromagnetic dampers to simultaneously mitigate vibration and harvest energy in vibration systems.

2. Propose a new control algorithm to control the regenerative electromagnetic shock absorber in vehicle suspension systems, one type of dual-mass vibration systems. Experimentally verify the concept and feasibilities of using regenerative electromagnetic shock absorbers to semi-actively control the vibration of a vehicle suspension system.

3. Develop a novel regenerative electromagnetic shock absorber aiming to provide enhanced performance in terms of vibration mitigation as well as energy harvesting. Apply it in a real vehicle suspension system.

4. Study the coupled dynamics of the suspension system with the proposed regenerative electromagnetic shock absorber. In addition, propose a new control algorithm suitable to controlling the proposed regenerative electromagnetic shock absorbers in improving the vehicle suspension performance in terms of vibration mitigation and energy harvesting.

The research accomplished in this dissertation includes:

1) Dynamics and modeling of dual-mass vibration systems with the regenerative electromagnetic tuned-mass dampers (EMTMDs). Additionally, deriving ready-to-use analytical tuning laws for this vibration system when the primary structure is subjected to force or base excitations. Both vibration mitigation and energy harvesting performances are optimized using H_2 criteria to minimize root-mean-square values of the deformation of the primary structure, or maximize the average harvestable power. Beyond simulations, experiments are also conducted to experimentally verify the effectiveness of the regenerative electromagnetic damper in both vibration mitigation and energy harvesting.
2) Propose an advanced semi-active control algorithm, named mixed Skyhook and Power-Driven-Damper (SH-PDD), to control the vehicle suspensions with a linear regenerative electromagnetic shock absorber. The superior characteristics of the SH-PDD are verified in numerical analysis as well as experiments. A 10-to-1 scaled-down quarter car test rig is built for the experiments to verify the feasibilities of controlling the vehicle suspension using the regenerative electromagnetic shock absorber.
3) Develop an innovative MMR-based shock absorber using a ball screw mechanism and bevel gears with one-way sprag clutches embedded. Analyze the dynamics of the proposed ball-screw-based MMR shock absorber. The analysis presented in this dissertation can be extended to other types of energy-harvesting regenerative shock absorbers involving clutches-embedded gear transmissions, not only limited to the proposed ball-screw-based MMR shock absorber. In addition to the theoretical analysis, lab and road tests are also carried out to experimentally analyze and characterize the superior characteristics of the proposed shock absorber.
4) The coupled dynamics of the suspension system with the proposed MMR-based shock absorber is explored and optimized. Meanwhile, a new control algorithm is proposed to control the proposed shock absorber considering its unique dynamics. The results show that the controlled proposed shock absorber can potentially improve ride comfort compared to conventional oil dampers.
5) Develop a new integrated design method to simultaneously optimize the coupled structural parameters and controllers of mechanical vibration systems by combining decentralized control techniques and Riccati-based control theories. Therefore, the overall performance

of the vibration system with a controllable electromagnetic shock absorber can be further improved.

The research in this dissertation has several scientific merits. (1). the research is interdisciplinary since it blends concepts of mechanical engineering and structural engineering with power system and electrical engineering concepts. It will bridge several separate areas and create new multidisciplinary knowledge. (2). it has the potential to revolutionize the approach of vibration mitigation from energy dissipation to electricity generation. Meanwhile, the harvested energy can be utilized to self-powered control the vibration system to further improve the vibration mitigation (3). The new-developed integrated design method can be extended to design the general mechanical systems including the structural components design and controller design.

1.3 Dissertation Organization

The introduction of this dissertation is presented in Chapter 1. Chapter 2 introduces the concept and optimization of dual-mass vibration systems with the energy-harvesting regenerative electromagnetic damper. Then, Chapter 3 proposes a new semi-active control algorithm aiming to control the vehicle suspension system, simplified as a dual-mass vibration system, using a linear regenerative electromagnetic shock absorber. In Chapter 4, a novel regenerative electromagnetic damper with a ball-screw-based mechanical motion rectifier (MMR) is proposed, which can perform as a controllable damper and meanwhile increase the power-dissipating density. In Chapter 5, develop an advanced semi-active control algorithm to control the proposed MMR-based shock absorber. In Chapter 6, a new integrated design framework for the general vibration system is proposed to further improve the performance of the vibration system. The conclusions and future works of this project are stated in Chapter 7.

2 Concept and Optimization of Dual-Mass Vibration Systems with the Regenerative Electromagnetic Damper

2.1 Chapter Introduction

This chapter proves that the regenerative electromagnetic damper or shock absorber is able to effectively mitigate the vibration of vibration systems. It can act as a traditional viscous damper when connected to a constant external resistive load. Moreover, the vibration mitigation performance can be further improved when the regenerative electromagnetic damper is connected to high-order electrical impedances. The numerical analysis and experimental verifications are presented based on a tall building system with the regenerative electromagnetic tuned-mass damper (EMTMD). This chapter also derives ready-to-use analytical tuning laws for the series EMTMD system when the primary structure is subjected to force or ground excitations. Both vibration mitigation and energy harvesting performances are optimized using H_2 criteria to minimize root-mean-square values of the deformation of the primary structure, or maximize the average harvestable power. Later, extensive numerical analysis is presented to show the effectiveness of the series EMTMDs. The numerical analysis shows that the series EMTMD is superior to mitigate the vibration of the primary structure nearly across the whole frequency spectrum, as compared to that of classic tuned-mass damper. Simultaneously, the series EMTMD can better harvest the energy due to broader bandwidth effect. Beyond simulations, this chapter also experimentally demonstrates the effectiveness of the regenerative electromagnetic tuned-mass damper, for the first time, in both vibration mitigation and energy harvesting performance. In our experimental setup, we built a small-scale dual-mass vibration system, in which a 3kg primary mass with a 10% mass ratio auxiliary mass is used. The experimental results match the numerical analysis closely.

2.2 Dual-mass Vibration System with the Regenerative Electromagnetic Tuned-mass Dampers (EMTMDs), and its Optimization Problem Formulation

2.2.1 Regenerative EMTMDs.

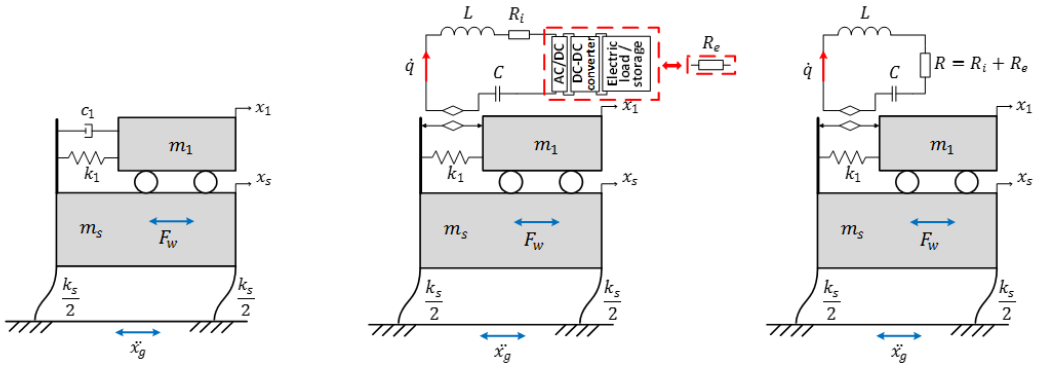

Figure 2.1. (a) Classic TMD, (b) EMTMD for energy harvesting and vibration control, (c) Simplified model of dual-functional series EMTMD

Figure 2.1(b) shows the series electromagnetic TMD (EMTMD) in which the original energy dissipative damping c_1 in classic TMDs, shown in Figure 2.1(a), is replaced by an electromagnetic transducer of coil resistance R_i and inductance L. The electromagnetic transducer is then shunted with a circuit including a capacitor C, an AC-DC converter, a DC-DC converter, energy storage elements and electric loads. The electromagnetic transducer and the circuit can be modeled as an ideal transducer shunted with an RLC circuit [30-31], shown in Figure 2.1(c). The dynamics of series EMTMDs are summarized as follows. The relative motion between the absorber m_1 and the primary structure m_s produce an induced voltage,e_{EMF}, which is proportional to their relative velocity

$$e_{EMF} = k_v(\dot{x_1} - \dot{x_s}) \tag{2.1}$$

where the proportional gain k_v [V/(m/s)] is the voltage constant of the electromagnetic transducer. The electrical current in the electromagnetic transducer will produce a force, f_{EMF}, proportional to the electrical current, $\dot{q}$,

$$f_{EMF} = k_f \dot{q} \tag{2.2}$$

where the proportional gain k_f [N/A] is the force constant. The constants k_v and k_f are only determined by transducer itself. Moreover the relation $k_v = k_f$ is held for an ideal transducer without energy loss. In the resonator circuit, the closed-loop voltage drop is zero according to Kirchhoff's voltage law [32], Thus we have

$$e_{EMF} + L\ddot{q} + R\dot{q} + \frac{1}{C}q = 0 \tag{2.3}$$

where the total resistance $R = R_i + R_e$ and R_e is the equivalent external load. The resonant frequency of the circuit itself is

$$\omega_e = 1/\sqrt{LC} \tag{2.4}$$

The electrical damping ratio of the circuit itself is

$$\zeta_e = \frac{R}{2L\omega_e} \tag{2.5}$$

And the electromagnetic mechanical coupling coefficient μ_k, defined in [57], is

$$\mu_k = \frac{k_v k_f}{L k_1} \tag{2.6}$$

where k_1 is the stiffness of the absorber. μ_k is actually a stiffness ratio (the electromagnetic mechanical coupling stiffness $\frac{k_v k_f}{L}$ divided by the stiffness of the mechanical shock absorber) which stands for the coupling capability of the mechanical system and the electrical system. For example, if u_k is very large, a slow movement between the absorber m_1 and the primary structure m_s will also create a very large equivalent electrical damping force.

The overall dynamic equations of the series EMTMD system, shown in Figure 1(c), are given by

$$\begin{cases} m_s\ddot{x}_s + k_f\dot{q} + (k_s{+}k_1)x_s - k_1x_1 = F_w - m_s\ddot{x}_g \\ m_1\ddot{x}_1 - k_f\dot{q} - k_1x_s + k_1x_1 = -m_1\ddot{x}_g \\ L\ddot{q} - k_v(\dot{x}_s - \dot{x}_1) + R\dot{q} + \frac{1}{C}q = 0 \end{cases} \tag{2.7}$$

where x_s and x_1 are the displacements of the primary structure and the absorber, respectively. m_s and m_1 are the mass of the primary structure and the absorber, respectively. k_s and k_1 are the stiffness of the primary structure and the absorber, respectively. F_w is external wind loads and $\ddot{x}_g$ is the ground acceleration caused by earthquakes.

2.2.2 Optimization problem formulation.

As mentioned in the introduction, large-scale civil structures mainly suffer from wind loads and earthquakes. Therefore, for the series EMTMD system, we wish to tune the parameters to minimize the building's vibration and maximize the average harvestable energy when the primary structure is subjected to force excitations ($\ddot{x_g} = 0$ in Figure 2.1(c)) or ground excitations ($F_w = 0$ in Figure 2.1(c)), respectively. In detail, the optimization problem of the EMTMD system is how to optimize the parameters of the absorber stiffness k_1, the inductance L, the capacitance C and the total resistance R for a given primary structure m_s, k_s with the absorber mass m_1 so that the buildings' deformation x_s is minimized and the average harvestable energy $R_e\dot{q}^2$ is maximized. Or equivalently, how to optimize the dimensionless parameters of

- mechanical tuning ratio $f_1 = \frac{\omega_1}{\omega_s} = \frac{\sqrt{k_1/m_1}}{\sqrt{k_s/m_s}}$,
- electromagnetic mechanical coupling coefficient $\mu_k = \frac{k_v k_f}{L k_1}$,
- electrical tuning ratio $f_e = \frac{\omega_e}{\omega_s} = \frac{\sqrt{1/LC}}{\sqrt{k_s/m_s}}$,
- electrical damping ratio $\zeta_e = \frac{R}{2L\omega_e} = \frac{R}{2\sqrt{L/C}}$,

for a given mechanical mass ratio $\mu = \frac{m_1}{m_s}$, where $\omega_s = \sqrt{k_s/m_s}$ is the natural frequency of the primary structure.

2.3 H_2 Optimization for the Force Excitation System

2.3.1 Vibration mitigation for the force excitation system.

Since the wind force that excites civil structures is of broad bandwidth [33], H_2 norm is better for evaluating the system performance because it is the root mean square (RMS) value of the performance under unit Gaussian white noise input [34]. In order to more completely mitigate the vibration of the primary structure, we minimize the H_2 norm from the excitation force F_w to the deformation of the primary structure x_s in Figure 2.1(c) by optimizing the tuning parameters of the series EMTMD. Thus, the performance index is defined as

$$PI = \frac{k_s^2 E[x_s^2]}{2\pi\omega_s S_F} = \frac{k_s^2\langle x_s^2\rangle}{2\pi\omega_s S_F} \tag{2.8}$$

where S_F is the uniform power spectrum density of the white-noise input force, E[] stands for the means square value, and <·> stands for the temporal average, respectively. The RMS value of the deformation of the primary mass x_s can be obtained as

$$\langle x_s^2\rangle = \omega_s S_\mathrm{F} \int_{-\infty}^{\infty} \left|\frac{X_s(j\alpha)}{F_w(j\alpha)}\right|^2 d\alpha \tag{2.9}$$

where $\alpha = \omega/\omega_s$ is the excitation frequency ratio. $\left|\frac{X_s(j\alpha)}{F_w(j\alpha)}\right|$ in Equation (2.9) is the norm of the transfer function from the excitation force F_w to the deformation of the primary structure x_s, where $j = \sqrt{-1}$ is the unit imaginary number. Substituting Equation (2.9) into Equation (2.8), the performance index in (2.8) can be expressed as:

$$PI = \frac{1}{2\pi}\int_{-\infty}^{\infty} \left|\frac{X_s(j\alpha)}{F_w(j\alpha)/k_\mathrm{s}}\right|^2 d\alpha \tag{2.10}$$

The normalized transfer function from F_w/k_s to x_s can be written in the dimensionless form by using the aforementioned dimensionless parameters, which is

$$\frac{X_s(j\alpha)}{F_w(j\alpha)/k_\mathrm{s}} = \frac{(j\alpha)^4+2\zeta_e f_e(j\alpha)^3+((1+\mu_k)f_1^2+f_e^2)(j\alpha)^2+2\zeta_e f_e f_1^2(j\alpha)+f_1^2 f_e^2}{\bar{A}_6(j\alpha)^6+\bar{A}_5(j\alpha)^5+\bar{A}_4(j\alpha)^4+\bar{A}_3(j\alpha)^3+\bar{A}_2(j\alpha)^2+\bar{A}_1(j\alpha)+\bar{A}_0} \tag{2.11}$$

where

$$\begin{cases} \bar{A}_6 = 1 \\ \bar{A}_5 = 2\zeta_e f_e \\ \bar{A}_4 = (1+\mu)(1+\mu_k)f_1^2 + f_e^2 \\ \bar{A}_3 = 2(1+\mu)\zeta_e f_e f_1^2 + 2\zeta_e f_e \\ \bar{A}_2 = (1+\mu_k)f_1^2 + (1+\mu)f_1^2 f_e^2 + f_e^2 \\ \bar{A}_1 = 2\zeta_e f_e f_1^2 \\ \bar{A}_0 = f_1^2 f_e^2 \end{cases} \tag{2.12}$$

The integral in Equation (2.10) can be solved using the residue theorem [36], the general formula of which can be found in the Appendix A. Hence, the performance index in (2.10) can be obtained as a function of the four design parameters f_1, μ_k, f_e, ζ_e and the given parameter μ.

$$PI = \frac{1}{4\mu f_1^2 \mu_k \zeta_e f_e}\{4\zeta_e^2 f_e^2[f_1^4(1+\mu)^2 - f_1^2(2+\mu)+1] + f_1^4(1+\mu)[f_e^2(1+\mu)-(1+\mu_k)]^2 - f_1^2[2f_e^4(1+\mu) - f_e^2(2+\mu)(2+\mu_k) + 2(1+\mu_k)] + (f_e^2-1)^2\} \tag{2.13}$$

In order to minimize the performance index PI regarding the vibration mitigation performance, the derivatives of PI with respect to all the design parameters should be equal to zero. Thus, we have

$$\frac{\partial PI}{\partial f_1} = 0, \quad \frac{\partial PI}{\partial \mu_k} = 0, \quad \frac{\partial PI}{\partial f_e} = 0, \quad \frac{\partial PI}{\partial \zeta_e} = 0 \tag{2.14}$$

Therefore, the following simultaneous gradients' equations can be obtained from Equation (2.14).

$$4\zeta_e^2 f_e^2[f_1^4(1+\mu)^2 - 1] + f_1^4(1+\mu)[f_e^2(1+\mu)-(1+\mu_k)]^2 - (f_e^2-1)^2 = 0 \tag{2.15a}$$

$$4\zeta_e^2 f_e^2[f_1^4(1+\mu)^2 - f_1^2(2+\mu)+1] + f_1^4(1+\mu)[f_e^4(1+\mu)^2 - 2f_e^2(1+\mu)+1-\mu_k^2] - 2f_1^2[f_e^4(1+\mu) - f_e^2(2+\mu)] + (f_e^2-1)^2 = 0 \tag{2.15b}$$

$$4\zeta_e^2 f_e^2[f_1^4(1+\mu)^2 - f_1^2(2+\mu)+1] + f_1^4(1+\mu)(f_e^2(1+\mu)-(1+\mu_k))(3f_e^2(1+\mu)+(1+\mu_k)) - f_1^2[6f_e^4(1+\mu) - f_e^2(2+\mu)(2+\mu_k) - 2(1+\mu_k)] + (f_e^2-1)(3f_e^2+1) = 0 \quad (2.15c)$$

$$4\zeta_e^2 f_e^2[f_1^4(1+\mu)^2 - f_1^2(2+\mu)+1] - f_1^4(1+\mu)[f_e^2(1+\mu)-(1+\mu_k)]^2 + f_1^2[2f_e^4(1+\mu) - f_e^2(2+\mu)(2+\mu_k) + 2(1+\mu_k)] - (f_e^2-1)^2 = 0 \quad (2.15d)$$

Solving this set of equations is nontrivial as it involves multiple nonlinear, high-order variables, but in the following we will simply summarize the solving process and then directly present the final results. This will highlight the results and avoid prolixity. By combining Equation (2.15d) with the other three equations in Equation (2.15), we can eliminate ζ_e to obtain a new equation set in design variables f_1, μ_k, f_e. Then using similar manipulations, we can eliminate f_1 and f_e from the new equation set and obtain Equation (2.16) in only variable μ_k.

$$(16+19\mu)\mu_k^2 - 16\mu(2+3\mu)\mu_k + 16\mu^3 = 0 \quad (2.16)$$

Therefore, the H_2 optimal μ_k can be obtained by Equation (2.16) as

$$\mu_k^{opt} = \frac{4\mu(4+6\mu+\sqrt{16+32\mu+17\mu^2})}{16+19\mu} \quad (2.17a)$$

Substituting the optimal μ_k into Equation (2.15), the optimal solutions of other design parameters can be similarly obtained, which are

$$f_1^{opt} = \frac{\sqrt{-\mu+\sqrt{16+32\mu+17\mu^2}}}{2(1+\mu)} \quad (2.17b)$$

$$f_e^{opt} = \sqrt{\frac{32+58\mu+25\mu^2+\mu\sqrt{16+32\mu+17\mu^2}}{2(16+35\mu+19\mu^2)}} \quad (2.17c)$$

$$\zeta_e^{opt} = \sqrt{\mu\frac{(96+272\mu+247\mu^2+70\mu^3)+(24+44\mu+18\mu^2)\sqrt{16+32\mu+17\mu^2}}{(16+19\mu)(16+23\mu+8\mu^2)}} \quad (2.17d)$$

At the optimal H_2 tuning condition, the performance index PI^{opt} is

$$PI^{opt} = \frac{f_e^{opt}\zeta_e^{opt}(-4-2\mu+\sqrt{16+32\mu+17\mu^2})}{\mu\mu_k^{opt}} \tag{2.18}$$

Since the mass ratio μ is a very small number, usually less than 0.1 for building-TMD systems, the square root term $\sqrt{16+32\mu+17\mu^2}$ in Equation (2.17) can be approximated as $4(1+\mu)$ by partially neglecting the terms involving second powers in μ. Therefore, a concise, approximate solution set can be obtained as

$$\begin{cases} {f_1}^{opt^*} = \frac{\sqrt{4+3\mu}}{2(1+\mu)} \\ {\mu_k}^{opt^*} = \frac{32\mu+40\mu^2}{16+19\mu} \\ {f_e}^{opt^*} = \sqrt{\frac{32+62\mu+29\mu^2}{2(16+35\mu+19\mu^2)}} \\ {\zeta_e}^{opt^*} = \sqrt{\frac{\mu(192+544\mu+495\mu^2+142\mu^3)}{256+672\mu+565\mu^2+152\mu^3}} \end{cases} \tag{2.19}$$

with the approximate optimal performance index PI^{opt^*}

$$PI^{opt^*} = \frac{2{f_e}^{opt^*}{\zeta_e}^{opt^*}}{{\mu_k}^{opt^*}} = \frac{\sqrt{(32+62u+29u^2)(192+544u+495u^2+142u^3)}}{4(4+5\mu)\sqrt{2u(1+u)(16+23u+8u^2)}} \tag{2.20}$$

After obtaining optimal dimensionless tuning parameters, the corresponding optimal absorber stiffness k_1^{opt}, the inductance L^{opt}, the capacitance C^{opt} and the total resistance R^{opt} are

$$\begin{cases} k_1^{opt} = m_1\omega_s^2{f_1^{opt}}^2 \\ L^{opt} = \frac{k_v k_f}{m_1\omega_s^2\mu_k^{opt}{f_1^{opt}}^2} \\ C^{opt} = \frac{m_1\mu_k^{opt}{f_1^{opt}}^2}{k_v k_f {f_e^{opt}}^2} \\ R^{opt} = \frac{k_v k_f f_e^{opt}}{m_1\omega_s\mu_k^{opt}{f_1^{opt}}^2} \end{cases} \tag{2.21}$$

It should be noted that R^{opt} is the optimal total resistance in which the tunable load is the external load R_e^{opt}, given by

$$R_e^{opt} = R^{opt} - R_i \tag{2.22}$$

It should be also noted that the H_2 tuning law for the classic TMD system in Figure 2.1(a) is [35]

$$\begin{cases} f^{opt} = \frac{1}{1+\mu}\sqrt{\frac{2+\mu}{2}} \\ \zeta^{opt} = \sqrt{\frac{\mu(4+3\mu)}{8(1+\mu)(2+\mu)}} \end{cases} \tag{2.23}$$

where f^{opt} and ζ^{opt} are the optimal tuning parameter and damping parameter defined in [35].

2.3.2 Energy harvesting for the force excitation system.

For optimizing the energy harvesting of the series EMTMD, we wish to maximize the average electrical power on the external load R_e. The instant power on the external load is

$$P(t) = R_e\dot{q}^2 \tag{2.24}$$

Therefore, when the system is subjected to the force excitation with a uniform power spectrum S_F, the performance index is defined as

$$PI = \frac{k_s^2 E[P(t)]}{2\pi\omega_s S_F} = \frac{k_s^2 R_e\langle\dot{q}^2\rangle}{2\pi\omega_s S_F} \tag{2.25}$$

where the RMS value of the current $\dot{q}$ can be obtained as

$$\langle\dot{q}^2\rangle = \omega_s S_{\mathrm{F}} \int_{-\infty}^{\infty} \left|\frac{\dot{Q}(j\alpha)}{F_w(j\alpha)}\right|^2 d\alpha \tag{2.26}$$

Substituting Equation (2.26) into Equation (2.25), the performance index in (2.25) can be expressed as:

$$PI = \frac{R_e}{2\pi}\int_{-\infty}^{\infty}\left|\frac{\dot{Q}(j\alpha)}{F_w(j\alpha)/k_s}\right|^2 d\alpha \tag{2.27}$$

where $\frac{\dot{Q}(j\alpha)}{F_w(j\alpha)/k_s}$ is the normalized transfer function from F_w/k_s to $\dot{q}$, which is

$$\frac{\dot{Q}(j\alpha)}{F_w(j\alpha)/k_s} = \frac{\frac{k_v}{L}(j\alpha)^4}{\bar{A}_6(j\alpha)^6+\bar{A}_5(j\alpha)^5+\bar{A}_4(j\alpha)^4+\bar{A}_3(j\alpha)^3+\bar{A}_2(j\alpha)^2+\bar{A}_1(j\alpha)+\bar{A}_0} \tag{2.28}$$

Similarly, by using the residue theorem [36], the performance index in (2.27) can be finally obtained as

$$PI = \frac{k_v}{2k_f m_s}\frac{R_e}{R_e+R_i} \tag{2.29}$$

where $\frac{k_v}{2k_f m_s}$ and R_i are the fixed parameters in the system. As we can see from Equation (2.29), the performance index depends on only one of the four design parameters: the external load R_e. This result agrees with the conclusions in [37], where the tuning of additional parameters is not necessarily better for energy harvesting under white noise types of excitation. Therefore, to maximize the power on the external load R_e, R_e needs to be maximized given the physical constraints of the system. Equation (2.29) also suggests that the energy harvesting performance is proportional to the mass of the primary structure under unit white-noise force disturbance. It is worth noting that the optimal tuning law for the vibration control given in Equation (2.17) and the optimal solution for the energy harvesting obtained from Equation (2.29) are different. Therefore, there is a trade-off between the vibration mitigation and energy harvesting performance when employing dual-functional EMTMDs.

2.4 H_2 Optimization for the Ground Excitation System

2.4.1 Vibration mitigation for the ground excitation system.

In this section, we wish to optimize the design parameters of the series EMTMD shown in Figure 2.1(c), when the system is subjected to the ground acceleration $\ddot{x}_g$. Similar to the definition in Section 3.1., the performance index regarding the H_2 norm from the ground acceleration $\ddot{x}_g$ to the deformation of the primary structure x_s is defined as

$$PI = \frac{1}{2\pi}\int_{-\infty}^{\infty}\left|\frac{X_s(j\alpha)}{\ddot{X}_g(j\alpha)/\omega_s^2}\right|^2 d\alpha \tag{2.30}$$

where $\frac{X_s(j\alpha)}{\ddot{X}_g(j\alpha)/\omega_s^2}$ is the normalized transfer function from $\ddot{x}_g/\omega_s^2$ to x_s. According to the system dynamics in Equation (2.7), its dimensionless form is given by

$$\frac{X_s(j\alpha)}{\ddot{X}_g(j\alpha)/\omega_s^2} = -\frac{(j\alpha)^4+2\zeta_e f_e(j\alpha)^3+\left((1+\mu)(1+\mu_k)f_1^2+f_e^2\right)(j\alpha)^2+2(1+\mu)\zeta_e f_e f_1^2(j\alpha)+(1+\mu)f_1^2 f_e^2}{\bar{A}_6(j\alpha)^6+\bar{A}_5(j\alpha)^5+\bar{A}_4(j\alpha)^4+\bar{A}_3(j\alpha)^3+\bar{A}_2(j\alpha)^2+\bar{A}_1(j\alpha)+\bar{A}_0} \tag{2.31}$$

By using the residue theorem [36], PI in Equation (2.30) can be similarly obtained as

$$PI = \frac{1}{4\mu f_1^2\mu_k\zeta_e f_e}\{4\zeta_e^2 f_e^2[f_1^4(1+\mu)^4 - f_1^2(1+\mu)(2+\mu-\mu^2)+1] + f_1^4(1+\mu)^3[f_e^4(1+\mu)^2 - 2f_e^2(1+\mu)(1+\mu_k)+(1+\mu_k)^2] - f_1^2(1+\mu)[2f_e^4(1+\mu)^2(1-\mu) - f_e^2(2+\mu-\mu^2)(2+\mu_k)+2(1+\mu_k)] + f_e^4(1+\mu^3) - 2f_e^2 + 1\} \tag{2.32}$$

Similarly, the gradients of the performance index PI in Equation (2.32) with respect to the four dimensionless design parameters should be equal to zero, see Equation (2.14). Therefore, we can obtain four simultaneous equations for the ground excitation system, as written below:

$$4\zeta_e^2 f_e^2[f_1^4(1+\mu)^4 - 1] + f_1^4(1+\mu)^3[f_e^4(1+\mu)^2 - 2f_e^2(1+\mu)(1+\mu_k)+(1+\mu_k)^2] - f_e^4(1+\mu^3) + 2f_e^2 - 1 = 0 \tag{2.33a}$$

$$4\zeta_e^2 f_e^2[f_1^4(1+\mu)^4 - f_1^2(1+\mu)^2(2-\mu)+1] + f_1^4(1+\mu)^3[f_e^4(1+\mu)^4 - 2f_e^2(1+\mu)+1-\mu_k^2] - 2f_1^2[f_e^4(1+\mu)^3(1-\mu) - f_e^2(1+\mu)^2(2-\mu)+(1+\mu)] + f_e^4(1+\mu^3) - 2f_e^2 + 1 = 0 \quad (2.33b)$$

$$4\zeta_e^2 f_e^2[f_1^4(1+\mu)^4 - f_1^2(1+\mu)^2(2-\mu)+1] + f_1^4(1+\mu)^3[3f_e^4(1+\mu)^2 - 2f_e^2(1+\mu)(1+\mu_k)+(1+\mu_k)^2] - f_1^2(1+\mu)[6f_e^4(1+\mu)^2(1-\mu) - f_e^2(1+\mu)(2-\mu)(2+\mu_k) - 2(1+\mu_k)] + 3f_e^4(1+\mu^3) - 2f_e^2 - 1 = 0 \quad (2.33c)$$

$$4\zeta_e^2 f_e^2[f_1^4(1+\mu)^4 - f_1^2(1+\mu)(2+\mu-\mu^2)+1] - f_1^4(1+\mu)^3[f_e^4(1+\mu)^2 - 2f_e^2(1+\mu)(1+\mu_k)+(1+\mu_k)^2] + f_1^2(1+\mu)[2f_e^4(1+\mu)^2(1-\mu) - f_e^2(2+\mu-\mu^2)(2+\mu_k)+2(1+\mu_k)] - f_e^4(1+\mu^3) + 2f_e^2 - 1 = 0 \quad (2.33d)$$

After similar manipulations summarized in Section 3.1., the H_2 optimal tuning law for the vibration mitigation under ground accelerations can be obtained as

$$\begin{cases} f_1^{opt} = \frac{\sqrt{4-3\mu}}{2(1+\mu)} \\ \mu_k^{opt} = \frac{128\mu}{64-36\mu-9\mu^2} \\ f_e^{opt} = \sqrt{\frac{16-9\mu}{16+19\mu+3\mu^2}} \\ \zeta_e^{opt} = \sqrt{\frac{192\mu}{256-96\mu-27\mu^2}} \end{cases} \quad (2.34)$$

At the H_2 optimal tuning condition, the performance index PI^{opt} is

$$PI^{opt} = \frac{(256-9\mu^2)\sqrt{(1+\mu)^3(48-27\mu)}}{32(16+3\mu)\sqrt{\mu(16-9\mu)}} \quad (2.35)$$

Then the corresponding optimal mechanical and electrical elements can be similarly obtained using Equations (2.21) and (2.22).

2.4.2 Energy harvesting for the ground excitation system.

If the system is subjected to ground accelerations, the energy harvesting performance index can be defined as

$$PI = \frac{R_e}{2\pi}\int_{-\infty}^{\infty}\left|\frac{\dot{Q}(j\alpha)}{\ddot{X}_g(j\alpha)/\omega_s^2}\right|^2 d\alpha \tag{2.36}$$

where $\frac{\dot{Q}(j\alpha)}{\ddot{X}_g(j\alpha)/\omega_s^2}$ is the normalized transfer function from $\ddot{x}_g/\omega_s^2$ to $\dot{q}$, the dimensionless form of which is

$$\frac{\dot{Q}(j\alpha)}{\ddot{X}_g(j\alpha)/\omega_s^2} = \frac{\frac{k_v}{L}(2\zeta_e(j\alpha)^3+(j\alpha)^2)}{\bar{A}_6(j\alpha)^6+\bar{A}_5(j\alpha)^5+\bar{A}_4(j\alpha)^4+\bar{A}_3(j\alpha)^3+\bar{A}_2(j\alpha)^2+\bar{A}_1(j\alpha)+\bar{A}_0} \tag{2.37}$$

Similarly, using the residue theorem [36], the performance index in (2.35) can be finally obtained as

$$PI = \frac{(m_s+m_1)k_v}{2k_f}\frac{R_e}{R_e+R_i} \tag{2.38}$$

The same conclusion, the energy harvesting depends on the only tuning variable: the external load R_e, that drawn from the force excitation system can also be drawn from Equation (2.38) for optimizing the energy harvesting in the ground excitation system. It should be noted that the harvestable energy in the ground excitation system under unit ground acceleration is proportional to the mass of the primary structure m_s and the mechanical shock absorber m_1. On the other hand, the harvestable energy in the system under unit wind force excitation is inversely proportional to the mass of the primary structure. This occurs because the heavier the mechanical structure, the smaller the induced motion due to unit force excitation is, which reduces the vibrational energy of the system. However, when the system is subjected to unit ground excitation, a heavier mechanical structure has a larger induced inertia force, therefore increasing the vibrational energy of the system.

Table 2.1 summarizes the H_2 tuning laws of the series EMTMD system when it is subjected to the force excitation and the ground acceleration excitation.

Table 2.1 H_2 tuning laws for series EMTMD systems.

		Vibration mitigation		Energy harvesting	
		H_2 tuning laws	Performance index	H_2 tuning laws	Performance index
Under Force Excitation F_w	Exact solution	$\begin{cases} f_1^{opt} = \frac{\sqrt{-\mu+r}}{2(1+\mu)} \\ \mu_k^{opt} = \frac{4\mu(4+6\mu+r)}{16+19\mu} \\ f_e^{opt} = \sqrt{\frac{32+58\mu+25\mu^2+\mu r}{2(16+35\mu+19\mu^2)}} \\ \zeta_e^{opt} = \sqrt{\mu\frac{(96+272\mu+247\mu^2+70\mu^3)+(24+44\mu+18\mu^2)r}{(16+19\mu)(16+23\mu+8\mu^2)}} \end{cases}$ $r = \sqrt{16+32\mu+17\mu^2}$	$\frac{1}{2\pi}\int_{-\infty}^{\infty}\left\|\frac{X_s(j\alpha)}{F_w(j\alpha)/k_s}\right\|^2 d\alpha = \frac{f_e^{opt}\zeta_e^{opt}(-4-2\mu+r)}{\mu\mu_k^{opt}}$	$R_e \gg R_i$	$\frac{R_e}{2\pi}\int_{-\infty}^{\infty}\left\|\frac{\dot{Q}(j\alpha)}{F_w(j\alpha)/k_s}\right\|^2 d\alpha = \frac{k_v}{2k_f m_s}\frac{R_e}{R_e+R_i}$
	Approx. solution	$\begin{cases} f_1{}^{opt^*} = \frac{\sqrt{4+3\mu}}{2(1+\mu)} \\ \mu_k{}^{opt^*} = \frac{32\mu+40\mu^2}{16+19\mu} \\ f_e{}^{opt^*} = \sqrt{\frac{32+62\mu+29\mu^2}{2(16+35\mu+19\mu^2)}} \\ \zeta_e{}^{opt^*} = \sqrt{\frac{\mu(192+544\mu+495\mu^2+142\mu^3)}{256+672\mu+565\mu^2+152\mu^3}} \end{cases}$	$\frac{1}{2\pi}\int_{-\infty}^{\infty}\left\|\frac{X_s(j\alpha)}{F_w(j\alpha)/k_s}\right\|^2 d\alpha \approx \frac{2f_e{}^{opt^*}\zeta_e{}^{opt^*}}{\mu_k{}^{opt^*}}$		
Under Ground Acceleration Excitation $\ddot{x}_g$		$\begin{cases} f_1^{opt} = \frac{\sqrt{4-3\mu}}{2(1+\mu)} \\ \mu_k^{opt} = \frac{128\mu}{64-36\mu-9\mu^2} \\ f_e^{opt} = \sqrt{\frac{16-9\mu}{16+19\mu+3\mu^2}} \\ \zeta_e^{opt} = \sqrt{\frac{192\mu}{256-96\mu-27\mu^2}} \end{cases}$	$\frac{1}{2\pi}\int_{-\infty}^{\infty}\left\|\frac{X_s(j\alpha)}{\ddot{X}_g(j\alpha)/\omega_s^2}\right\|^2 d\alpha = \frac{(256-9\mu^2)\sqrt{(1+\mu)^3(48-27\mu)}}{32(16+3\mu)\sqrt{\mu(16-9\mu)}}$		$\frac{R_e}{2\pi}\int_{-\infty}^{\infty}\left\|\frac{\dot{Q}(j\alpha)}{\ddot{X}_g(j\alpha)/\omega_s^2}\right\|^2 d\alpha = \frac{(m_s+m_1)k_v}{2k_f}\frac{R_e}{R_e+R_i}$

2.5 Numerical Analysis

2.5.1 Graphical representations

Figure 2.2 graphically shows the H_2 tuning laws for the vibration mitigation when the primary structure is disturbed by the force and the ground acceleration, respectively. It is clear to see that the error between the exact solution and the approximate solution for the force excitation system is extremely small. Therefore, the approximate solution is a good alternative to avoid computational complexities in practice. It is also obvious to see that the H_2 tuning laws for these two different excitations are close when the mass ratio μ is small, and become more and more distinct as μ increases.

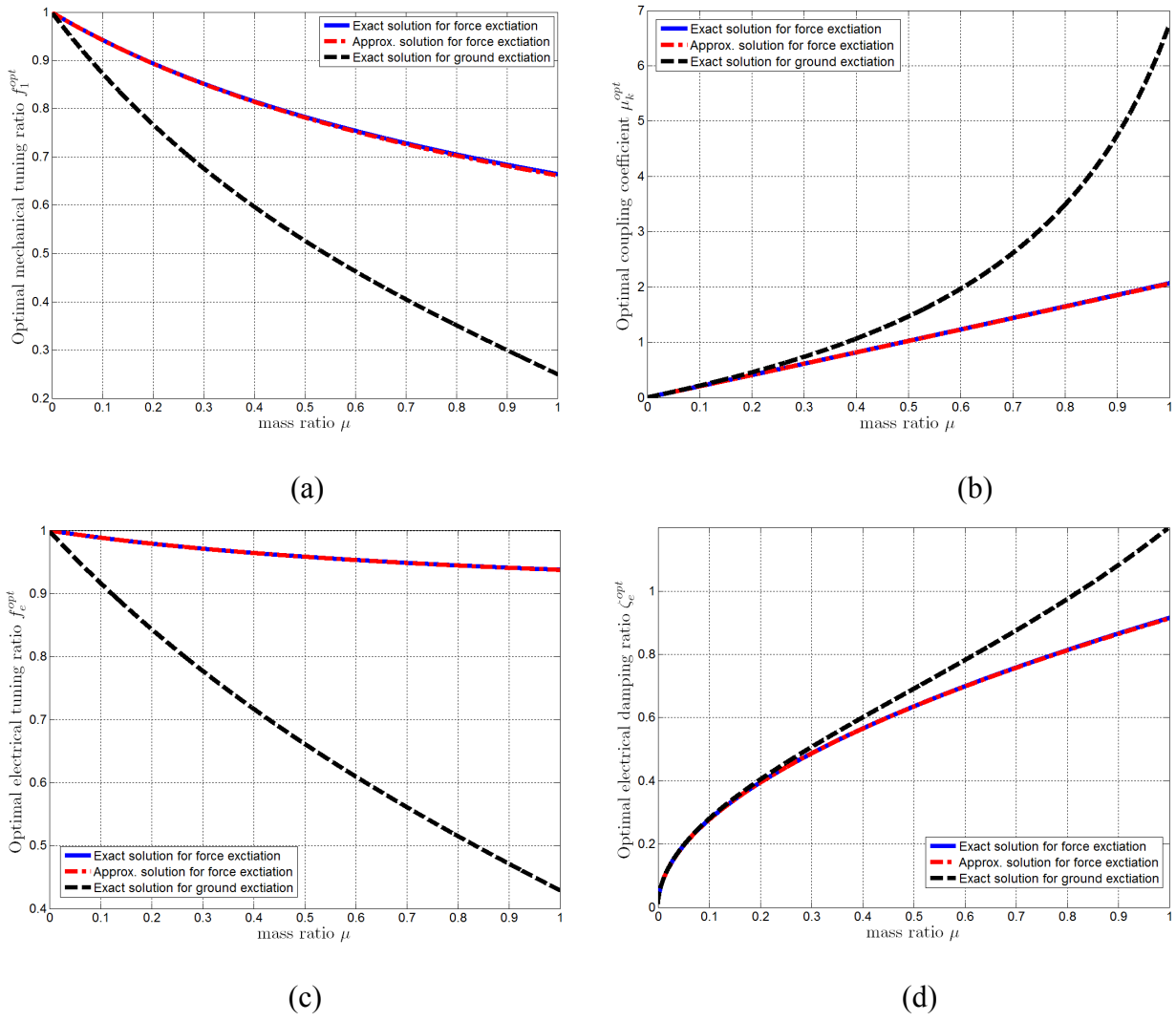

Figure 2.2. Graphical representations of the H_2 tuning laws. (a) Optimal mechanical tuning ratio f_1; (b) Optimal electromagnetic mechanical coupling coefficient μ_k; (c) Optimal electrical tuning ratio f_e; (d) Optimal electrical damping ratio ζ_e.

2.5.2 Optimal performance index for vibration mitigation

Figure 2.3 shows the optimal performance index PI^{opt} for the vibration mitigation under force and ground excitations respectively, as obtained in Equations (2.18), (2.20) and (2.35). From Figure 2.3, we can see that the change in the optimal performance index with respect to the mass ratio μ acts like an exponential decay. It initially decreases very rapidly, then the decreasing rate becomes

smaller, as μ increases from zero. In practice, this exponential-like trend can help make better trade-offs between the vibration mitigation performance and TMD costs for series EMTMDs.

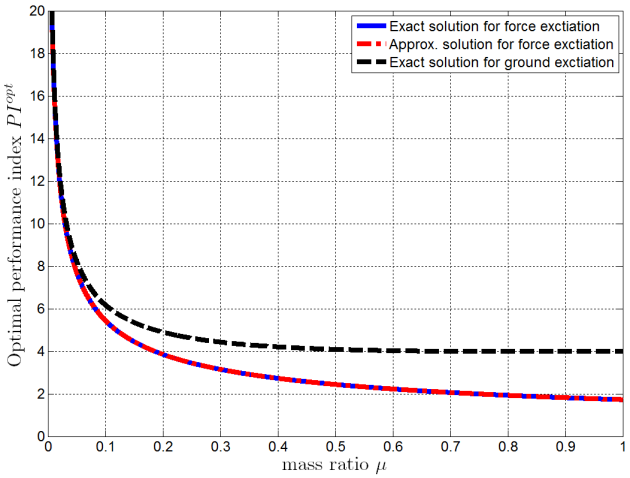

Figure 2.3. Optimal performance index PI^{opt} for the vibration mitigation.

2.5.3 Frequency responses for vibration mitigation

The optimal frequency response of the normalized primary structure displacement under force excitation $\frac{X_s(j\alpha)}{F_w(j\alpha)/k_s}$ or ground excitation $\frac{X_s(j\alpha)}{\ddot{X}_g(j\alpha)/\omega_s^2}$ are shown in Figure 2.4 in comparison with that of the classic TMD and the system without TMD, where the mass ratio $\mu = 1\%$ as a common case. It is noted that the classic TMD is also optimized for vibration mitigation using H_2 criteria, the corresponding tuning laws can be found in Equation (2.23). From Figure 2.4, it is clear that the series EMTMD is superior to mitigate the vibration of the primary structure nearly across the whole frequency spectrum for both the force and the ground excitation system, as compared to that of classic TMDs and systems without a TMD. At their own resonant frequencies, the peak value of the normalized displacement in the series EMTMD system is reduced by around 25% compared to that of the classic TMD system.

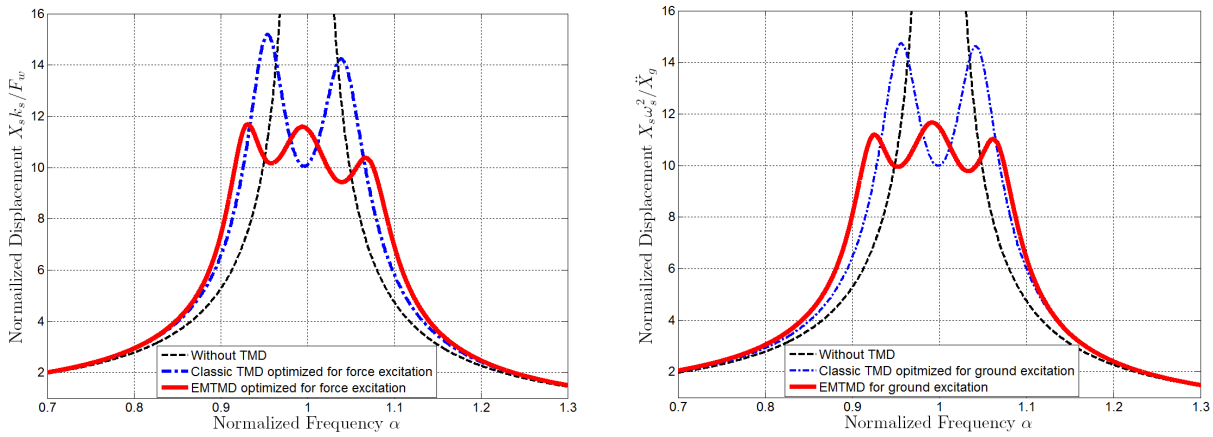

(a) (b)

Figure 2.4. The optimal normalized frequency response for vibration mitigation in comparison with the classic TMD and the system without a TMD, where mass ratio $\mu = 0.01$. (a) force excitation system; (b) ground excitation system.

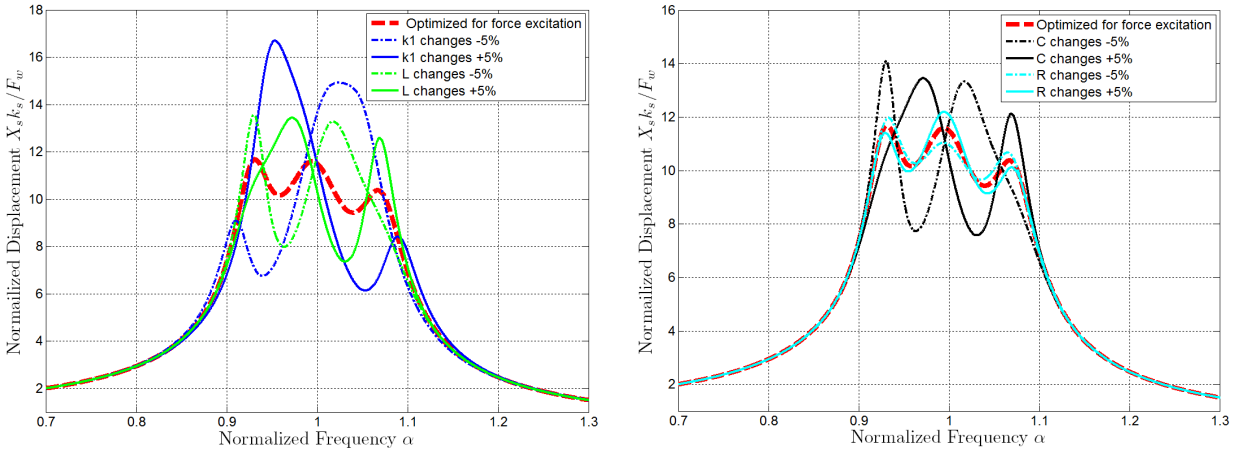

(a) (b)

Figure 2.5. The vibration performance change to the changes of the design parameters in the force excitation system. (a) the changes of the stiffness of mechanical shock absorber k_1 and the inductance of electrical resonator L; (b) the changes of the capacitance C and total resistance R.

2.5.4 Sensitivities of the tuning parameters

In practice it is difficult to tune perfectly, or perhaps some parameters may change over time. Figure 2.5 shows how the vibration mitigation performance will change with the uncertainties of the tuning parameters for the force excitation system. It can be concluded that the mechanical

tuning ratio f_1, namely the stiffness of the mechanical shock absorber, is the most sensitive design parameter to the vibration performance and that the electrical damping ratio ζ_e, namely the total resistance of the electrical resonator, is the least sensitive to the vibration performance. It should be noted that Figure 2.5 are based on the tuning laws obtained for the force excitation system, as in Equation (2.18). A similar conclusion can be also drawn for the design optimized for the ground excitation system.

2.5.5 Frequency responses of harvestable power

Series EMTMDs are capable of mitigating vibration and simultaneously harvesting the vibrational energy of the system. In this subsection, we show the energy harvesting capability of the series EMTMD when it is optimized for vibration mitigation. The frequency response from force excitation F_w to the square root of the normalized power of the series EMTMD is shown in Figure 2.6 in comparison with that of the passive damping power in classic TMD systems. The linear transducer used in the series EMTMD is assumed to be an ideal one in which $R_i = 0$ and $k_v = k_f$. The mass ratio μ is also set as 1%. From Figure 2.6, it is clear to see that the series EMTMD outperforms the classic TMD in power harvested due to broader bandwidth effect.

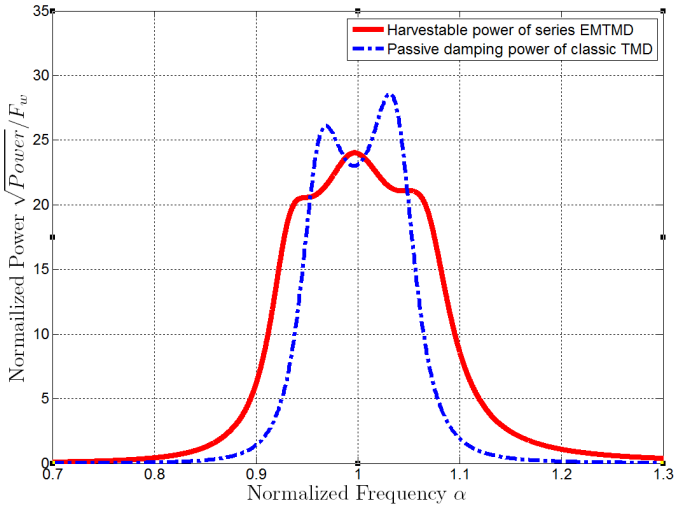

Figure 2.6. The normalized linear power spectrum density ($\sqrt{\mathrm{W/Hz}}$) of harvestable energy in ideal series EMTMDs optimized for vibration mitigation in comparison with that of classic TMDs. In ideal series EMTMDs, $R_i = 0$ and $k_v = k_f$.

2.6 Experimental Verification

2.6.1 Experimental setup

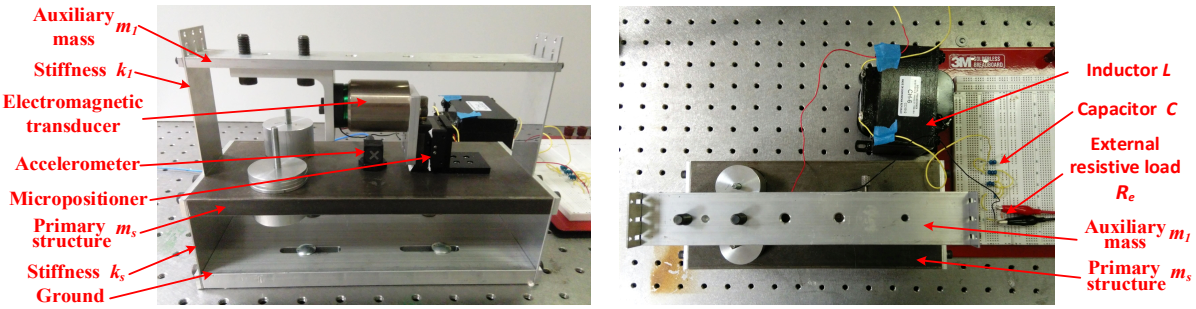

(a) (b)

Figure 2.7. The experimental setup of the series EMTMD with adjustable elements. (a) Front view (b) Top view

Figure 2.7 shows the experimental setup of the series EMTMD system with adjustable design elements. By using this setup, the motions of the primary structure and the mechanical TMD can be simplified as one-degree linear motions in the horizontal direction when the motion strokes are small. A voice coil motor is installed between the primary structure and the mechanical TMD, which acts as a linear electromagnetic transducer. A micro-positioner is used to align the coil and magnet of the motor to avoid frictions. A horizontal impulse force perpendicular to the primary structure was applied to the primary structure by using an impact hammer to emulate a broadband force excitation. An accelerometer is used to measure the frequency response of the acceleration of the primary structure under the force excitation. Later, the frequency response of the normalized displacement of the primary structure can be obtained by

$$\left|\frac{X_s(j\omega)}{F_w(j\omega)/k_s}\right| = \left|\frac{\ddot{X}_s(j\omega)}{F_w(j\omega)}\right| \frac{k_s}{\omega^2}$$

The voltage across on the external resistive load and the impact force are recorded to show the simultaneous energy harvesting capabilities of series EMTMDs. The parameters of the setup are listed in Table 2.2.

Table 2.2 The parameters of the experimental setup.

Description	Symbol	Value
Primary structure mass	m_s	3 [kg]
Mechanical TMD mass	m_1	0.3 [kg]
Stiffness of the primary structure	k_s	189.5[kN/m]
Stiffness of the mechanical TMD	k_1	16.84 [kN/m]
Total inductance of electrical resonator	L	41.8 [mH]
Total capacitance of electrical resonator	C	387 [μF]
Internal resistance of linear motor	R_i	4.35[Ω]
External resistance	R_e	1.3[Ω]
Force excitation	F_w	Impulse force

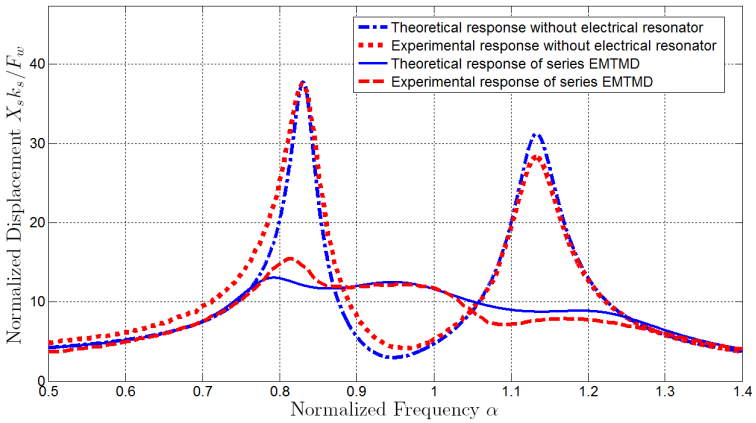

Figure 2.8. Theoretical and experimental frequency response of the series EMTMD system and the system without electrical resonator.

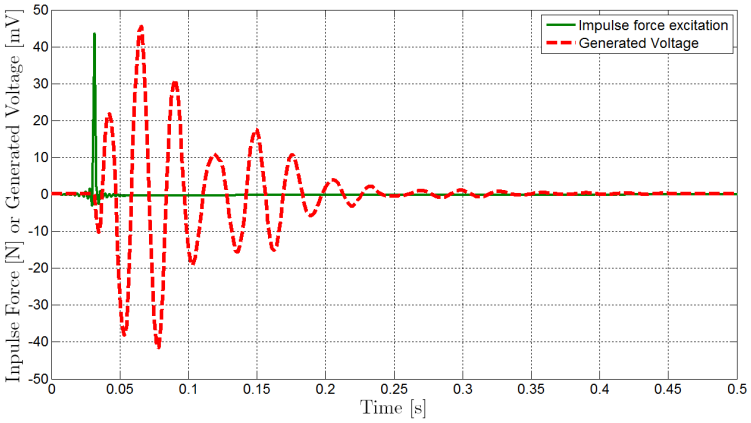

Figure 2.9. Experimental output voltage across on external resistive load R_e under an impulse force excitation.

2.6.2 Experimental results

Figure 2.8 shows the theoretical and experimental frequency responses of the normalized displacements of the primary structure when excited by an impulse force. Both responses of the series EMTMD system and the system without electrical resonator are presented to display the influence of the electrical resonator in vibration mitigation performance. The experimental results match the theoretical responses closely. From Figure 2.8, it is clear that the series EMTMD system outperforms the system without the electrical resonator in vibration mitigation, by reducing the resonant peak by around 58.7%. It should be noted that the system without electrical resonator is the system with the open RLC circuit, which is not the optimal classic TMD system. The voltage simultaneously generated and the corresponding impulse force are plotted in Figure 2.9, in which the peak voltage is around 45 mV and the peak value of the impulse force is around 43 N. To sum up, Figure 2.8-2.9 clearly demonstrated the dual functions of series EMTMDs, namely simultaneous enhanced vibration mitigation and energy harvesting functions.

2.7 Chapter Summary

This Chapter investigates the energy-harvesting series electromagnetic tuned-mass damper (EMTMD) system, which consists of a single degree-of-freedom (DOF) primary mechanical system, an auxiliary mechanical shock absorber, a regenerative electromagnetic damper with an electrical RLC circuit. This chapter also derives ready-to-use analytical H_2 tuning laws for the series EMTMD system when the primary structure is subjected to force or ground excitations, respectively. Both vibration mitigation and energy harvesting performance were optimized using H_2 criteria. These analytical tuning laws can easily guide the design of series EMTMDs under various excitations. Based on the tuning laws of the series EMTMD, it is found that an optimal design for vibration mitigation is mainly related to four tuning parameters, which are the mechanical tuning ratio f_1, the electromagnetic mechanical coupling coefficient μ_k, the electrical tuning ratio f_e, and the electrical damping ratio ζ_e. However, the design that aims to maximize the average harvestable energy is only dependent on one of the four design parameters, the resistance of the electrical resonator. Other than the tuning parameters, the harvestable energy in the system under a unit ground acceleration excitation is proportional to the mass of the primary structure m_s

and the mechanical shock absorber m_1, while the harvestable energy in the system under a unit force excitation is inversely proportional to the mass of the primary structure.

The numerical analysis shows that the series EMTMD can achieve enhanced performance in terms of both vibration and energy harvesting due to tuning both the resonances of the mechanical shock absorber and the electrical resonator, as compared to classic TMDs in which only the mechanical shock absorber is tuned. Finally, the experiment shows the simultaneous enhanced vibration mitigation and energy harvesting functions of series EMTMDs. Particularly, the series EMTMD with the electrical resonator improves the vibration mitigation by reducing the resonant peak by 58.7%, as compared to that without the electrical resonator. It also shows the large amount voltage simultaneously generated on the external resistive load under a broad bandwidth force excitation.

Through the numerical and experimental verification, it is proved that the regenerative electromagnetic damper or shock absorber is able to effectively mitigate the vibration of vibration systems. It can act as a traditional viscous damper when connected to a constant external resistive load. Moreover, the vibration mitigation performance can be further improved when the regenerative electromagnetic damper is connected to high-order electrical impedances. Meanwhile, the regenerative electromagnetic damper or shock absorber is able to harvest the vibration energy otherwise dissipated by the traditional viscous damper.

3 A Novel Semi-Active Damping Control for the Vehicle Suspension Using a Regenerative Electromagnetic Shock absorber

3.1 Chapter Introduction

The regenerative electromagnetic shock absorber can work as a semi-active controllable damper when its external electrical load is being adjusted. In this chapter, a new suspension damping control algorithm is proposed to control the electromagnetic shock absorber in improving the performance of vehicle suspensions. A linear regenerative electromagnetic shock absorber is used in the suspension control experiments, which verifies the function of the regenerative electromagnetic shock absorber in controlling vehicle suspension systems. In practice, semi-active suspensions provide better trade-offs between performances and costs than passive or active damping. Many different semi-active control algorithms have been developed, including Skyhook (SH) [5], Acceleration-Driven-Damper (ADD) [6], Power-Driven-Damper (PDD) [7], mixed Skyhook and Acceleration-Driven-Damper (SH-ADD) [8], and others. Among them, it has been shown that the SH-ADD is quasi-optimal in reducing the sprung mass vibration. This chapter analyzes the abilities of vehicular suspension components, the shock absorber and the spring, from the perspective of energy transfer between the sprung mass and the unsprung mass, and propose a new sprung mass control algorithm named mixed Skyhook and Power-Driven-Damper (SH-PDD). The proposed algorithm defines a switching law that is capable of mixing Skyhook (SH) and Power-Driven-Damper (PDD), and simultaneously marries their advantages to achieve a better suspension performance. As a result, the proposed SH-PDD is effective in reducing the sprung mass vibration across the whole frequency spectrum, similar to SH-ADD and much better than SH, PDD and ADD, while eliminating the control chattering and high-jerk behaviors as occurred in SH-ADD. The superior characteristics of the SH-PDD are verified in numerical analysis as well as experiments.

3.2 System Modeling and Control Problem Statement

3.2.1 System modeling

A 2-DOF vehicle suspension system with an electromagnetic semi-active damper, depicted in Figure 3.1, is used to design and evaluate the control algorithms in this chapter. Its dynamic motion is governed by the following equations:

$$\begin{cases} m_s\ddot{z}_s = -c(t)(\dot{z}_s - \dot{z}_u) - k_s(z_s - z_u) \\ m_u\ddot{z}_u = c(t)(\dot{z}_s - \dot{z}_u) + k_s(z_s - z_u) - k_u(z_u - z_r) \\ \dot{c}(t) = -\beta c(t) + \beta c^d(t), \quad c_{min} \le c^d(t) \le c_{max} \end{cases} \tag{3.1}$$

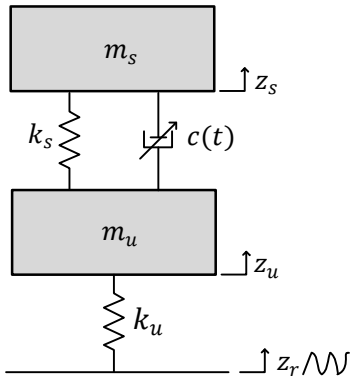

Figure 3.1 2-DOF quarter car model with an electromagnetic semi-active damper

where m_s and m_u are the sprung mass and the unsprung mass respectively, z_s and z_u are the vertical displacement of the sprung mass and the unsprung mass respectively, z_r is the uneven road displacement which is the exogenous disturbance to the system, k_s is the stiffness of the suspension spring, k_u is the equivalent stiffness of the tire. $c(t)$ denotes the actual damping coefficient. $c^d(t) \in [c_{min}, c_{max}]$ is the desired damping input. β denotes the dampers' bandwidth. In such a system, an original invariant viscous damper is replaced by an electromagnetic electromagnetic semi-active damper $c(t)$ linked between the sprung mass and the unsprung mass, which aims to achieve better suspension performances including ride comfort, road holding, etc. The above electromagnetic semi-active damper has been widely studied in the automotive industry. Its damping coefficient $c(t)$ can be tuned between $[c_{min}, c_{max}]$ and the corresponding damping force $c(t)(\dot{z}_s - \dot{z}_u)$ is used to dampen the vertical motion of the suspension system. The damper's

dynamics are usually specified by a first order filter with the parameter β representing the dampers' bandwidth. The larger β is, the faster the damper can follow the input $c^d(t)$.

3.2.2 Control objectives

Ride comfort is usually the major concern for passengers. Humans are most sensitive to vertical vibrations at frequencies in the range of [4Hz, 7Hz] [38]. Therefore, the first control objective in this chapter is to reduce the sprung mass acceleration $\ddot{z}_s$ under the road disturbance z_r. The corresponding performance index [39] is defined as

$$PI_{acceleration}(N) = \sqrt{\frac{\frac{1}{N}\sum_{i=1}^{N} \ddot{z}_s(i)^2}{\frac{1}{N}\sum_{i=1}^{N} z_r(i)^2}} \qquad i = 1,2,\cdots,N \tag{3.2}$$

which measures the normalized vertical acceleration of the sprung mass over N samples. The second control objective in this chapter is to lower the sprung mass jerk $\dddot{z}_s$ under the road disturbance z_r, thus further improving ride comfort. The corresponding performance index is defined as

$$PI_{jerk}(N) = \sqrt{\frac{\frac{1}{N}\sum_{i=1}^{N} \dddot{z}_s(i)^2}{\frac{1}{N}\sum_{i=1}^{N} z_r(i)^2}} \qquad i = 1,2,\cdots,N \tag{3.3}$$

Another important performance index of the vehicle suspension is the road holding evaluated by the tire deflections $z_u - z_r$ under the road disturbance z_r, which is defined as [38]

$$PI_{road\ holding}(N) = \sqrt{\frac{\frac{1}{N}\sum_{i=1}^{N} (z_u(i) - z_r(i))^2}{\frac{1}{N}\sum_{i=1}^{N} z_r(i)^2}} \quad i = 1,2,\cdots,N \tag{3.4}$$

It is worth noting that a practical sprung mass control algorithm, such as Sky-hook, SH-ADD, etc., should not deteriorate road holding performance too much, while improving ride comfort.

3.3 Power Flow Analysis of Suspension Systems and Energy Perspectives of Some Existing Semi-active Controls

In this section, we analyze the abilities of vehicle suspensions from the perspective of energy transfer between the sprung mass and the unsprung mass. Then several well-known semi-active control algorithms, such as SH, ADD, PDD, SH-ADD, are reinterpreted from power flow point of views, which will guide the design of the control algorithm we propose. Finally, the nonlinear frequency responses [6] of the existing methods are presented to be the benchmarks for later evaluations.

3.3.1 Power flow analysis of suspension systems

When vehicles are driving on roads, the unevenness of roads is the only external source to exchange the energy with vehicle suspensions. At some instant, the total mechanical energy stored in the suspension system is

$$E(t) = \frac{1}{2}m_s\dot{z_s}^2 + \frac{1}{2}m_u\dot{z_u}^2 + \frac{1}{2}k_s(z_s - z_u)^2 + \frac{1}{2}k_u(z_u - z_r)^2 \tag{3.5}$$

Taking the derivative of the total energy with respect to time, the power flow of the suspension system can be obtained as

$$P(t) = k_u\dot{z_r}(z_r - z_u) - c(t)(\dot{z_s} - \dot{z_u})^2 \tag{3.6}$$

On the right-hand side of Eq. (3.6), the first term is the power flowing into the suspension system from the road profile and the second term is the power dissipated by the electromagnetic semi-active damper.

According to Newtonian mechanics, power is equal to force times velocity. Therefore, at some instant, the power of the sprung mass absorbed by the electromagnetic semi-active damper is

$$P_{sd} = c(t)(\dot{z_s} - \dot{z_u})\,\dot{z_s} \tag{3.7}$$

The power of the sprung mass absorbed by the suspension spring is

$$P_{ss} = k_s(z_s - z_u)\,\dot{z}_s \tag{3.8}$$

The power which the electromagnetic semi-active damper releases to the unsprung mass is

$$P_{ud} = c(t)(\dot{z}_s - \dot{z}_u)\,\dot{z}_u \tag{3.9}$$

The power which the suspension spring releases to the unsprung mass is

$$P_{us} = k_s(z_s - z_u)\,\dot{z}_u \tag{3.10}$$

Therefore, the net power flowing into the suspension is

$$P_{net} = P_{sd} + P_{ss} - P_{ud} - P_{us} = c(t)(\dot{z}_s - \dot{z}_u)(\dot{z}_s - \dot{z}_u) + k_s(z_s - z_u)(\dot{z}_s - \dot{z}_u) \tag{3.11}$$

It is worth noting that the power flow of each component represents its energy transfer ability. For instance, P_{sd}(or $-P_{sd}$) represents the electromagnetic semi-active damper's ability of absorbing (or releasing) the power from (or to) the sprung mass; P_{ud}(or $-P_{ud}$) represents the electromagnetic semi-active damper's ability of releasing (or absorbing) power to (or from) the unsprung mass. Moreover, the net power flowing into the suspension P_{net} evaluates the energy decoupling ability of the suspension between the sprung mass and the unsprung mass.

3.3.2 Energy perspectives of Skyhook (SH)

Skyhook (SH) was initially proposed to reduce the oscillation of the sprung mass. Its main idea is to virtually create an ideal suspension system in which the chassis is "hooked" to a virtual inertial frame called "sky" by a passive damper c_{sky}, then using the real suspension with an electromagnetic semi-active damper to emulate the dynamics of this ideal suspension system.

From energy point of view, the power of the sprung mass absorbed by the suspension can be expressed as

$$P_{sd} + P_{ss} = c(t)\dot{z}_{su}\dot{z}_s + k_s z_{su}\dot{z}_s \tag{3.12}$$

where $z_{su} = (z_s - z_u)$ and $\dot{z}_{su} = (\dot{z}_s - \dot{z}_u)$. If we design a control law to reduce the oscillation of the sprung mass by using the suspension to dissipate the kinetic energy of the sprung mass as much as possible at every moment, then this control law , since P_{ss} is not controllable, can be designed as

$$c(t) = \begin{cases} c_{max}, & if\ \dot{z}_{su}\dot{z}_s \geq 0 \\ c_{min}, & if\ \dot{z}_{su}\dot{z}_s < 0 \end{cases} \tag{3.13}$$

When P_{sd} is positive, the damper is absorbing power from the sprung mass. This absorbed power can be maximized by setting $c(t) = c_{max}$. Otherwise when the damper is releasing power to the sprung mass, the released power can be minimized by setting $c(t) = c_{min}$. Noticing that (3.13) are exactly the same as the two-state SH control law in [6], the physical insight of the SH algorithm is just dissipating the power from the sprung mass as much as possible.

$$Skyhook \Leftrightarrow min_{c(t)} J\big(c(t)\big) \triangleq -(P_{sd} + P_{ss}) \tag{3.14}$$

3.3.3 Energy perspectives of Power-Driven-Damper (PDD) and Acceleration-Driven-Damper (ADD)

The Power-Driven-Damper (PDD) is newly proposed in [8] using port Hamiltonian techniques. Its control law is given by

$$c_{PDD}(t) = \begin{cases} c_{max} & if\ k_s z_{su}\dot{z}_{su} + c_{max}\dot{z}_{su}^2 < 0 \\ c_{min} & if\ k_s z_{su}\dot{z}_{su} + c_{min}\dot{z}_{su}^2 \geq 0 \\ \frac{c_{max}+c_{min}}{2} & if\ \dot{z}_{su} = 0\ \&\ z_{su} \neq 0 \\ \frac{-k_s z_{su}}{\dot{z}_{su}} & otherwise \end{cases} \tag{3.15}$$

Starting from an energy point of view, we found the vehicle suspension has the ability to decouple the energy between the sprung mass and the unsprung mass. Moreover, this ability can be evaluated by the value of P_{net} (3.11): the closer to zero P_{net} is, the better energy isolation the suspension can achieve. By minimizing the absolute value of P_{net} (3.11), we can obtain this energy-decoupling control law as:

$$c(t) = \begin{cases} c_{min}, & if\ k_s z_{su}\dot{z}_{su} + c_{min}\dot{z}_{su}^2 \geq 0 \\ c_{max} & if\ k_s z_{su}\dot{z}_{su} + c_{max}\dot{z}_{su}^2 < 0 \\ \frac{-k_s z_{su}}{\dot{z}_{su}} & otherwise \end{cases} \tag{3.16}$$

Comparing the energy-decoupling control law in (3.16) with the control law of PDD in (3.15), we found that they have the same structure except one condition in PDD: $c_{PDD}(t) = \frac{c_{max}+c_{min}}{2}, if\ \dot{z}_{su} = 0\ \&\ z_{su} \neq 0$. However the existence of this condition in PDD is only to make the damping coefficient change smoothly. Therefore, PDD is just trying to balance the power flowing into the suspension.

$$PDD \Leftrightarrow min_{c(t)} J\big(c(t)\big) \triangleq |P_{net}| \tag{3.17}$$

Acceleration-Driven-Damper (ADD), proposed by Savaresi *et al.* [6], aims to minimize the acceleration of the sprung mass at each sampling instant based on several light assumptions. The ADD control law is [6]

$$c_{ADD}(t) = \begin{cases} c_{max}, & if\ \ddot{z}_s(\dot{z}_s - \dot{z}_u) \geq 0 \\ c_{min}, & else \end{cases} \tag{3.18}$$

After plugging the system dynamics in (3.1), ADD can be reformed as:

$$c_{ADD}(t) = \begin{cases} c_{max}, & if\ k_s z_{su}\dot{z}_{su} + c(t)\dot{z}_{su}^2 < 0 \\ c_{min}, & else \end{cases} \tag{3.19}$$

Comparing (3.19) and (3.16), it is obvious that ADD tries to balance the power flowing into the suspension when only a two-state electromagnetic semi-active damper is available.

$$\text{ADD} \Leftrightarrow min_{c(t)} J\big(c(t)\big) \triangleq |P_{net}|,\ c(t) \in \{c_{min}, c_{max}\} \tag{3.20}$$

Although PDD and ADD were developed from completely different theories, they have similar isolating performances due to the same energy perspectives mentioned above, which have been proven by their similar nonlinear frequency responses presented in [8].

However, as pointed out in [8], the effectiveness of ADD is highly sensitive to the damper's bandwidth β. A damper with large bandwidth may cause control chattering behaviors. This is because the ADD, $c_{ADD}(t)$, directly depends on the sprung mass acceleration $\ddot{z}_s$, namely if β is large enough, the controlled variable is influenced instantaneously by the measured variables. Due to this control chattering behavior, ADD may cause larger jerks than most other control algorithms, which deteriorates ride comfort. PDD is very similar to ADD regarding the vibration reduction of the sprung mass, except that PDD does not directly depend on the acceleration $\ddot{z}_s$ and hence significantly lowers the jerk of the sprung mass.

3.3.4 Energy perspectives of mixed Skyhook and ADD (SH-ADD)

The SH-ADD control algorithm [7] is given by

$$c_{SH-ADD}(t) = \begin{cases} c_{SH}(t), & if\ \ddot{z}_s - \alpha^2 \dot{z}_s \geq 0 \\ c_{ADD}(t), & else \end{cases} \tag{3.21}$$

where α is a design parameter dependent on the suspension system and $\ddot{z}_s - \alpha^2 \dot{z}_s \geq 0 (or\ < 0)$ is the "frequency selector" selecting Skyhook or ADD rules at the end of every sampling period. Essentially, the SH-ADD defines a switching law to direct the power flow driven by the SH and the ADD in suspension systems. As shown in [7], the SH-ADD approaches the optimal filtering limit of semi-active control. However, similar to ADD, SH-ADD may show an oscillating behavior on semi-active damping $c_{SH-ADD}(t)$ if the bandwidth β is wide enough. This oscillating behavior is caused not only by the ADD control algorithm but also the switching law $\ddot{z}_s - \alpha^2 \dot{z}_s \geq 0$ (or <

0) due to the fact that the switching law also directly depends on the controlled variable $\ddot{z}_s$. More characteristics of SH-ADD will be presented later.

The nonlinear frequency responses, from the road disturbance z_r to the sprung mass acceleration $\ddot{z}_s$, of the aforementioned control algorithms are plotted in Figure 3.2. The procedures to generate the nonlinear frequency responses have been summarized in [6]. Similarly to the system considered in [6], we also take damper's bandwidth β and minimum damping c_{min} into account in this chapter to emulate real situations more closely. The parameters of a real suspension are cited from [6] and [40], as listed in Table 3.1.

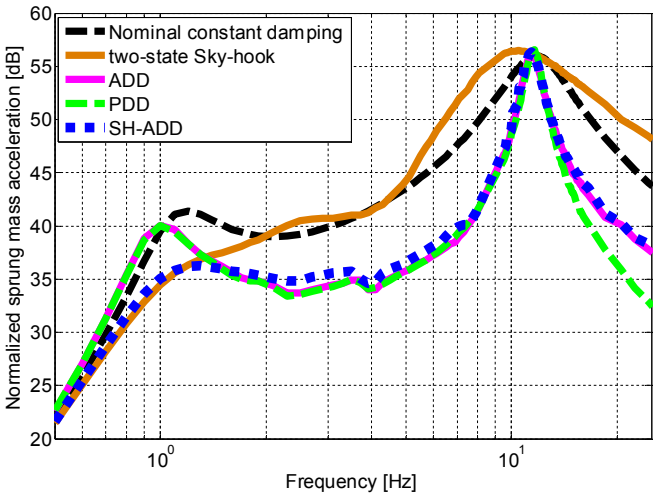

Figure 3.2 The nonlinear frequency response from the road disturbance z_r to the sprung mass acceleration $\ddot{z}_s$ of the existing control algorithms

Table 3.1 Simulation parameters: real vehicle suspension

Parameters	Value	description
T_s	2[ms]	Sampling interval
m_s	400[kg]	Sprung mass
m_u	50[kg]	Unsprung mass
k_s	20 [kN/m]	Suspension stiffness
k_u	250[kN/m]	Tire stiffness
β	50.2π	Damper's bandwidth
c_{min}	300[N/(m/s)]	Min. damping coeff.
c_{max}	4000[N/(m/s)]	Max. damping coeff.
c_n	1500[N/(m/s)]	Nominal constant
A	0.05[m]	The amplitude of sinusoid
S_0	$64[m^2/$	Degree of road roughness
V_{sb}	7.2 [km/h]	Rolling over speed bump
V	80.5 [km/h]	Vehicle moving velocity

3.3.5 The influence of asymmetrical damping

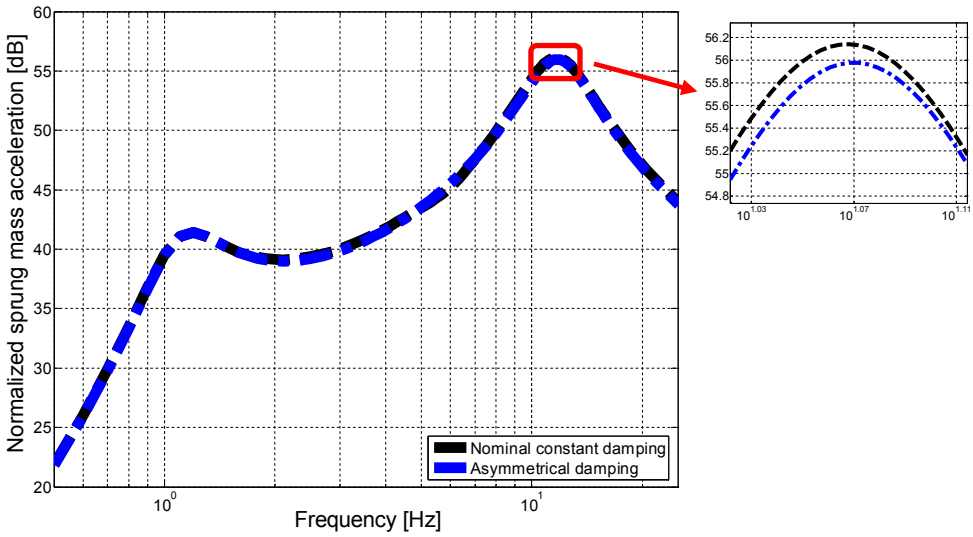

Figure 3.3 The influence of asymmetrical damping

The influence of asymmetrical damping is also studied in this subsection. The asymmetrical damping is set to

$$c(t) = \begin{cases} 2250\text{N/(m/s)}, & if\ \dot{z}_{su} \geq 0 \\ 750\text{N/(m/s)}, & if\ \dot{z}_{su} < 0 \end{cases}$$

which means the damping of extended shock absorber is 3 times of the damping of the compressed shock absorber. The frequency response of the chassis acceleration with asymmetrical damping is plotted in Figure 3.3 in comparison with the symmetrical case as presented before. The results show that the asymmetrical damping can achieve a slightly smaller acceleration around the second resonant peak, as compared to symmetrical damping. However, the overall performance is similar to the symmetrical damping. Therefore, the symmetrical damping is employed as a benchmark in the following analysis. More details about asymmetrical damping is investigated in [41].

3.4 A New Low-jerk Control Algorithm: Mixed Skyhook and Power-Driven-Damper Control (SH-PDD)

As mentioned, SH-ADD is effective at reducing the sprung mass vibration across the whole frequency spectrum at the expense of causing high jerks and control chattering on the sprung mass. To further improve the control performance, one may wonder if there is a new semi-active control algorithm that is effective in reducing the sprung mass vibration across the whole frequency spectrum, similar to SH-ADD, while it simultaneously eliminates control chattering and high-jerk behaviors as occurred in SH-ADD. In response to this, we propose mixed Skyhook and Power-Driven-Damper (SH-PDD) control algorithm. It should be noted that simply replacing ADD with PDD in SH-ADD control algorithm does not remove the control chattering and high-jerk behaviors since the "frequency selector" of SH-ADD also directly depends on the sprung mass acceleration $\ddot{z}_s$.

In Section 3, it is explained that SH essentially utilizes the suspension to dissipate energy from the sprung mass as much as possible so that the chassis oscillation is mitigated. On the other hand, PDD or ADD utilize the suspension to decouple the energy between the sprung mass and the unsprung mass. It is easy to be aware that SH and PDD (or ADD) conflict in some time periods and this confliction mainly results from the energy transfer abilities of the suspension: P_{sd} and P_{ud}.

For instance, if $P_{sd} + P_{ud} \geq 0$, the suspension is able to transfer all the energy absorbed from the sprung mass to the unsprung mass. During this time period, SH can be applied to dissipate the energy away from the sprung mass. Otherwise if $P_{sd} + P_{ud} < 0$, SH and PDD (or ADD) behave oppositely since the more energy is absorbed by the suspension, the more energy remains in the

suspension. Based on the above thoughts, the SH-PDD control algorithm essentially mixes SH and PDD by the switching law $P_{sd} + P_{ud} \geq 0$. The SH-PDD control law is given by:

$$c_{SH-PDD}(t) = \begin{cases} c_{SH}(t), & if\ \dot{z}_s^2 - \dot{z}_u^2 \geq 0 \\ c_{PDD}(t), & else \end{cases} \tag{3.22}$$

The SH-PDD control algorithm in (3.22) states that when $\dot{z}_s^2 - \dot{z}_u^2 \geq 0$, the SH control law is applied so that the suspension can dissipate the energy away from the sprung mass as much as possible. On the other hand, when $\dot{z}_s^2 - \dot{z}_u^2 < 0$, the PDD control law is applied to try to balance the energy flowing into the suspension. This means that the suspension is only allowed to dissipate the energy of the sprung mass moderately during this period. After substituting the explicit rules of SH and PDD, the simplified SH-PDD control law is explicitly given by

$$c_{SH-PDD}(t) = \begin{cases} c_{max}, & if\ \dot{z}_s^2 - \dot{z}_u^2 \geq 0\ or\ k_s z_{su}\dot{z}_{su} + c_{max}\dot{z}_{su}^2 < 0 \\ c_{min}, & if\ \dot{z}_s^2 - \dot{z}_u^2 < 0\ and\ k_s z_{su}\dot{z}_{su} + c_{min}\dot{z}_{su}^2 \geq 0 \\ \frac{-k_s z_{su}}{\dot{z}_{su}}, & otherwise \end{cases} \tag{3.23}$$

The nonlinear frequency response, from the road disturbance z_r to the sprung mass acceleration $\ddot{z}_s$, of the SH-PDD is plotted in Figure 3.4. It shows that the SH-PDD closely inherits the vibration isolation benefits of both Skyhook and PDD, which verifies the mixing effectiveness of the switching law. Comparing Figure 3.2 and Figure 3.4, it can be seen that the SH-PDD is almost the same as SH in the low frequency range and the same as PDD in the high frequency range, while the transmissibility of the SH-ADD is still slightly larger than the ADD between the first and second resonances. Therefore, we can conclude that the proposed switching law is more effective than the "frequency selector" in the SH-ADD at mixing and inheriting the benefits of the existing control algorithms. Also, the SH-PDD does not require the design parameter α existing in the SH-ADD, which reduces the design uncertainties. However, as compared to the two-state control algorithm SH-ADD, the SH-PDD is a continuous one due to the continuous control algorithm PDD, which requires a continuous electromagnetic semi-active damper.

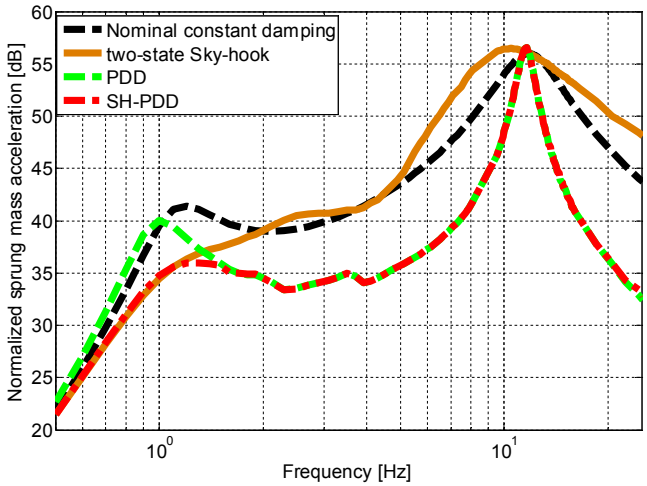

Figure 3.4 The nonlinear frequency response, from the road disturbance z_r to the sprung mass acceleration $\ddot{z}_s$, of the SH-PDD control algorithm

An insightful interpretation from suspension dynamics point of view:

The proposed switching law in the SH-PDD selects the SH or the PDD rule according to the instant value $(\dot{z}_s^2 - \dot{z}_u^2)$ at the end of every sampling period. For every short sampling period, the damping coefficient $c(t) = c$ can be taken as a constant value [6]. Therefore the semi-active system can be approximated as a linear system during every sampling period in which the transfer function from $\dot{z}_u$ to $\dot{z}_s$ is

$$\mathcal{L}\left\{\frac{\dot{z}_s}{\dot{z}_u}\right\}(s) = \frac{cs+k_s}{m_s s^2+cs+k_s} \tag{3.24}$$

where s is the Laplace variable and c is the constant damping in every sampling period. Figure 3.5 shows the magnitude of the frequency response of $|\dot{z}_s/\dot{z}_u|$. From Figure 3.5, it is clear that $|\dot{z}_s|$ is dominant around the sprung mass resonance while $|\dot{z}_u|$ is dominant in the high frequency range, regardless of the value of the current damping coefficient in the current sampling period. Therefore, in the low frequency range, we have the following relation in practice

$$|\dot{z}_s| \geq |\dot{z}_u| \tag{3.25a}$$

Similarly, in the high frequency range, we have the following relation in practice

$$|\dot{z}_s| < |\dot{z}_u| \tag{3.25b}$$

The relation in (3.25) is the same as the proposed switching law in (3.22). Therefore, the proposed switching law is not only based on heuristic reasoning, but can be given a rational explanation to explain why it is able to select the SH in the low frequency range and select the PDD in the high frequency range. By letting $\left|\frac{\dot{z}_s}{\dot{z}_u}\right| = 1$, the crossover frequency is given by

$$f_{crossover} = \sqrt{\frac{2k_s}{m_s}} \tag{3.26}$$

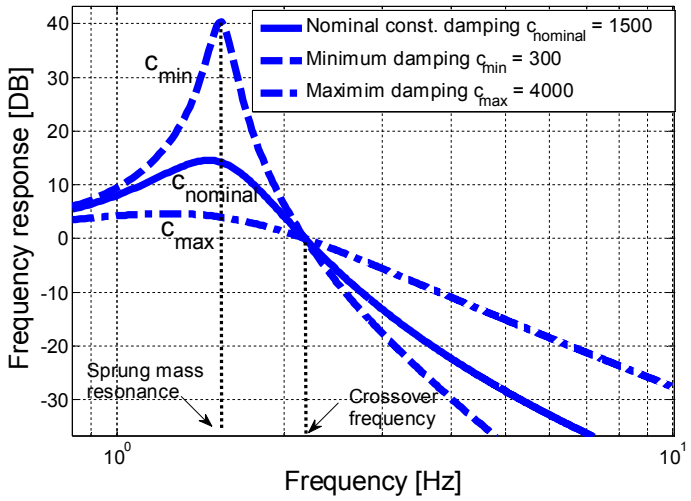

Figure 3.5 The frequency response of the magnitude $\frac{|\dot{z}_s|}{|\dot{z}_u|}$

3.5 Numerical Analysis

3.5.1 Nonlinear frequency responses.

The frequency domain comparison of the SH-ADD and the SH-PDD, in terms of ride comfort and road holding, is shown in Figure 3.6. Figure 3.6(a) shows that the SH-PDD, similar to the SH-ADD, is effective at attenuating the sprung mass acceleration across the whole frequency spectrum. Moreover, it is even slightly better than the SH-ADD beyond the second resonance.

Since the SH-ADD is almost the optimal semi-active control algorithm in terms of ride comfort [7], it can be concluded that the SH-PDD is also approaching the optimal limit in terms of ride comfort. The ride comfort and the road holding are known to be conflicting. Thus, it is necessary to check that the road holding does not deteriorate too much for the proposed SH-PDD. As shown in Figure 3.6(b), the SH-PDD also achieves similar road holding performance across the whole frequency spectrum, as compared to the SH-ADD. However, they both increase the peak of the second resonance, as compared to the conventional suspension with a nominal constant damping.

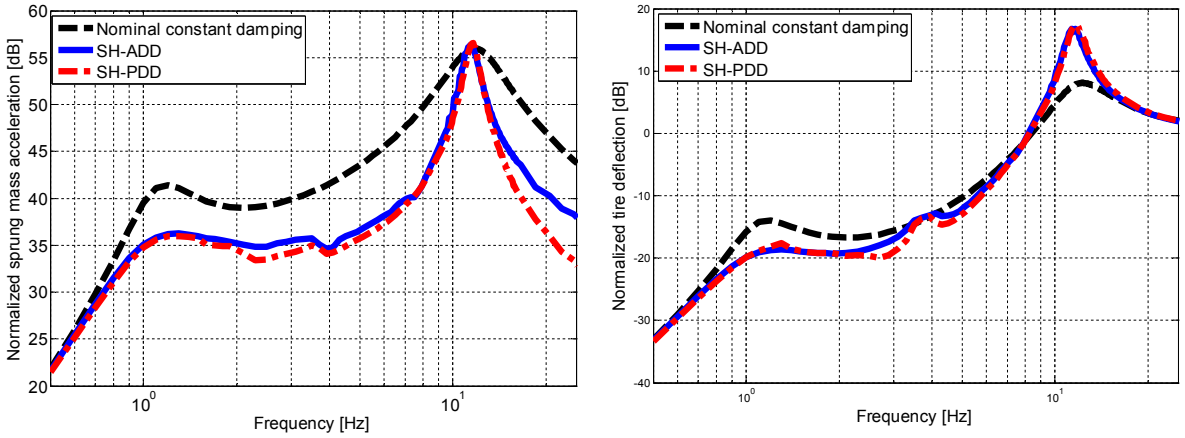

(a) (b)

Figure 3.6 The nonlinear frequency responses of the SH-ADD and the SH-PDD control algorithm from the road disturbance z_r (a) to the sprung mass acceleration $\ddot{z}_s$; (b) to the tire deflection $z_u - z_r$;

3.5.2 Initial condition excitations.

In this part, we apply two large initial disturbances to the semi-active suspension, which are

(a) $\dot{z}_s = -1[m/s], z_s = 0.15[m]$;

(b) $\dot{z}_u = -1[m/s], z_u = 0.02[m]$;

These two initial disturbances emulate the shocks to the sprung mass and the unsprung mass, respectively. The corresponding responses are shown in Figure 3.7. As shown in Figure 3.7(a), when the sprung mass is disturbed, the suspension is oscillating in the low frequency range. During

this time period, SH-PDD inherits the isolating performance of SH, of which the response is better than that of passive suspension and PDD. On the other hand, the suspension is oscillating in the high frequency range when the unsprung mass is disturbed. At this moment, SH-PDD acts like PDD, of which the response is better than that of the passive suspension and SH. To sum up, the shock tests show that SH-PDD always automatically performs as the better one of SH and PDD across whole frequency spectrum. These results agree with the nonlinear frequency response of the SH-PDD shown in Figure 3.4, in comparison with that of the SH and the PDD.

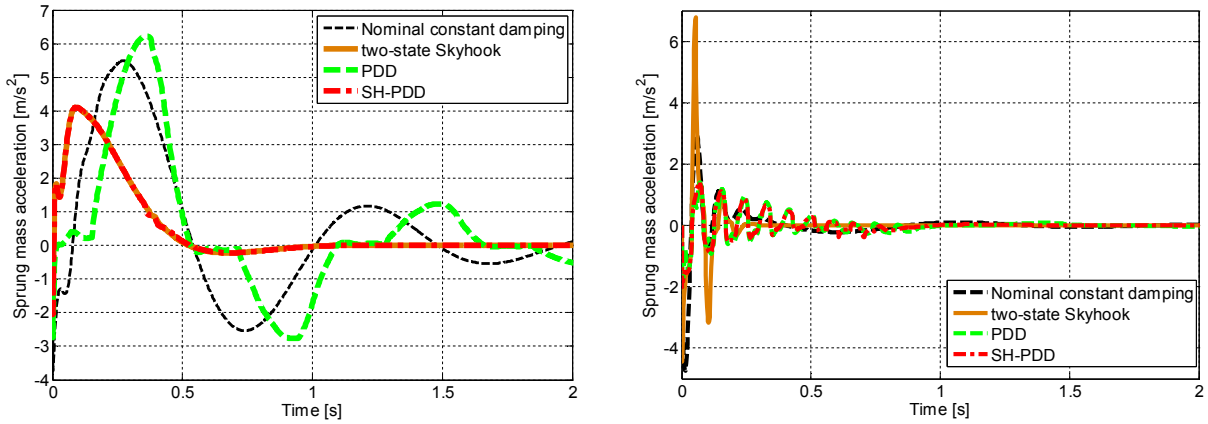

Figure 3.7 Initial condition excitation (a) I.C. $\dot{z}_s = -1[m/s]$, $z_s = 0.15[m]$; (b) I.C. $\dot{z}_u = -1[m/s]$, $z_u = 0.02[m]$;

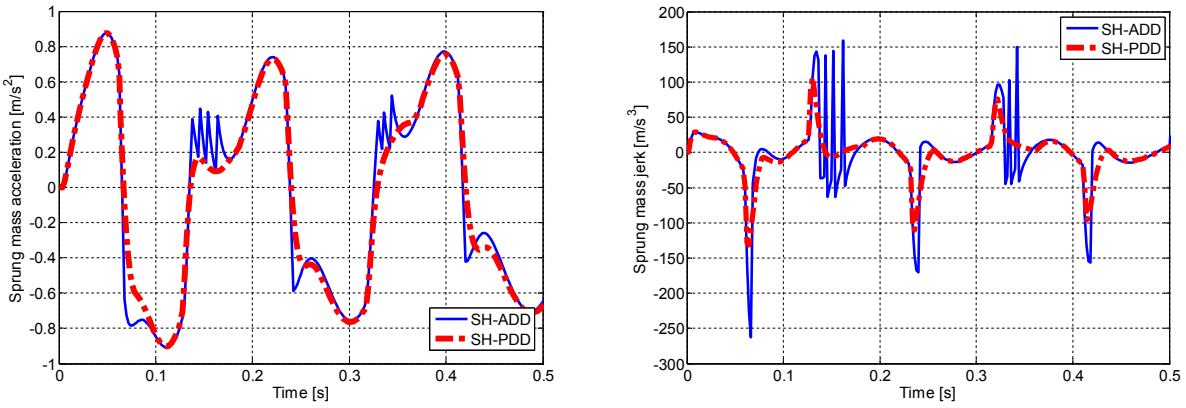

Figure 3.8 The response of single frequency excitation at 5.5 Hz (a) Sprung mass acceleration; (b) Sprung mass jerk

3.5.3 Single frequency excitations.

The response of the SH-PDD under a single frequency excitation is presented, in comparison with that of the SH-ADD, in Figure 3.8. As mentioned previously, humans are sensitive to the vertical vibration at frequencies ranging from 4Hz to 7Hz, so we choose a 5.5 Hz single frequency excitation as the most sensitive case. As shown in Figure 3.8, the SH-PDD is slightly better than the SH-ADD in attenuating the sprung mass acceleration while significantly reducing the sprung mass jerk and the control chattering behaviors on sprung mass. This simulation result agrees with the analysis in the previous sections. It is noted that high jerks and control chattering behaviors exist in the SH-ADD, which agrees with the results in [6] and [7].

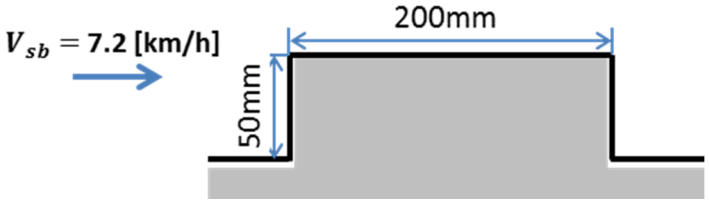

Figure 3.9 Speed bump dimensions

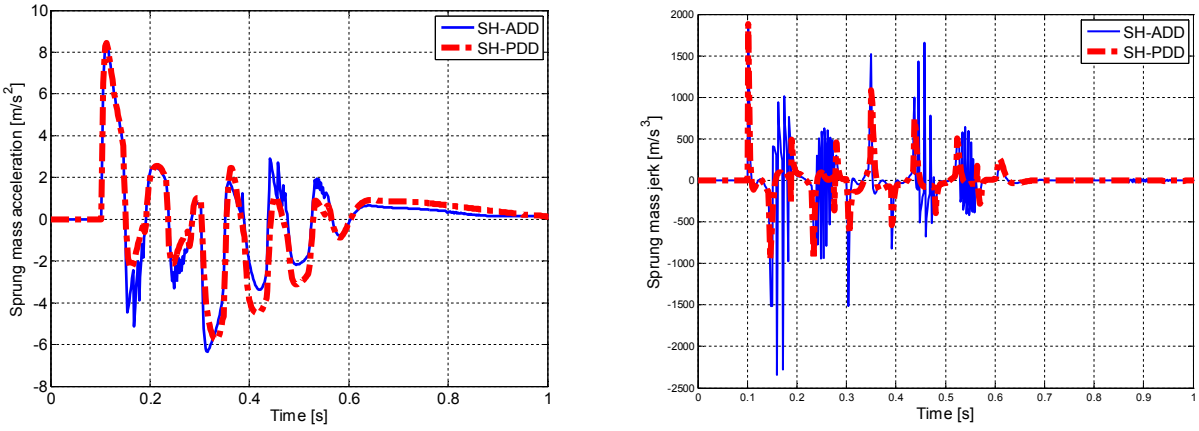

(a) (b)

Figure 3.10 Speed bump response (a) Sprung mass acceleration; (b) Sprung mass jerk

3.5.4 Speed bump tests.

The real road disturbances experienced by vehicle suspension systems include road obstacles and regular unevenness. A vehicle passing over a speed bump 0.05m high and 0.2m wide at 7.2 km/h (4.5 mph) was taken as a bump test study. The dimensions of the speed bump are depicted in

Figure 3.9. The speed bump responses of the SH-PDD and the SH-ADD are shown in Figure 3.10. Figure 3.10 shows that the SH-PDD can significantly reduce the sprung mass jerk while remaining effective at attenuating the sprung mass acceleration for a speed bump response, as compared to that of the SH-ADD. This conclusion agrees with the conclusion from Figure 3.8.

3.5.5 Random road unevenness tests.

In addition to the speed bump test, the tests of the semi-active suspension under random road disturbances were also carried out to show the advantages of the SH-PDD. The road displacements were generated by following the International Standard Organization (ISO) which divides the road into several classes according to the degree of road roughness, as shown in Table 3.2 [42-44]. Since most of highways or drives in the U.S. are classified Class C and better, we took the mean value of degree of road roughness of Road Class C as a case study. The disturbance generating procedures are summarized below:

Table 3.2 Degree of road roughness

Road class	S_0 range, $(\times 10^{-6})$	S_0 mean, $(\times 10^{-6})$
A (very good)	<8	4
B (Good)	8-32	16
C (Average)	**32-128**	**64**
D (Poor)	128-512	256

S_0 in $[m^2/(cycle/m)]$ at reference spatial frequency $v_0 = 1/(2\pi)$ $[cycle/m]$ suggested by ISO. Road-roughness coefficient $G_r = S_0/({v_0}^{-2})$

(a) Generating a white noise with 0 mean value and unit intensity Power Spectrum Density (PSD).
(b) Then the road displacement z_r is generated by letting the white noise pass by a filter [45]

$$G(s) = \frac{\sqrt{2\pi V G_r}}{s+\omega_0} \tag{3.27}$$

where $\omega_0 = 2\pi V v_0$, v_0 is the cutoff spatial frequency which is between 0.001 and 0.02 cycles/m. As long as ω_0 is far smaller than the resonant frequency of vehicle, it is acceptable [44]. Here ω_0 is chosen to be 0.01.

(c) The generated z_r then excites the quarter car model (3.1) controlled by different control laws for a 60-second period.

(d) The root mean square (RMS) value of the sprung mass acceleration $\ddot{z}_s$, the sprung mass jerk $\dddot{z}_s$ and the tire deflection $z_u - z_r$ are recorded for the evaluation of different control methods.

(f) The improvement of different control laws is defined by

$$\text{Improvement} = \frac{RMS_{passive}(\ddot{z}_s) - RMS_i(\ddot{z}_s)}{RMS_{Passive}(\ddot{z}_s)} \tag{3.28}$$

where $RMS_{passive}(\ddot{z}_s)$ is RMS value of $\ddot{z}_s$ of nominal passive suspension and $RMS_i(\ddot{z}_s)$ stands for the RMS value of $\ddot{z}_s$ of different control laws (SH, PDD, ADD, SH-ADD, SH-PDD).

The performances, including the root-mean-square values of the sprung mass acceleration $\ddot{z}_s$, the sprung mass jerk $\dddot{z}_s$ and the tire deflection $z_u - z_r$, of the semi-active suspensions under random road disturbances are summarized in Table 3.3. From Table 3.3, it can be seen that both the SH-ADD and the SH-PDD effectively reduce the sprung mass accelerations, significantly improving ride comfort as compared to the nominal constant damper and other electromagnetic semi-active dampers. However, the jerk of the SH-PDD is much lower than that of the SH-ADD, which can further improve the ride comfort and also protect the suspension. It should also be noted that the SH-PDD, similar to the SH-ADD, is a sprung mass control algorithm which improves the ride comfort at the expense of road holding performance, with larger tire deflections as compared to the passive suspension.

Table 3.3 The performances of the semi-active suspensions under random road disturbance

Control algorithms	Sprung mass acc. $RMS(\ddot{z}_s)$ [m/s^2] (Improvement)	Sprung mass jerk $RMS(\dddot{z}_s)$ [m/s^3]	Tire deflection $RMS(z_u - z_r)$ [mm]
Nominal const.	1.07 (0%)	67.04	3.7
SH	1.14(-6.5%)	117.49	3.9
ADD	0.84(21.5%)	109.31	5.6
PDD	0.83(22.4%)	61.72	5.7
SH-ADD	0.773(27.75%)	121.03	5.2
SH-PDD	**0.770 (28.04%)**	**70.81**	**5.3**

3.6 Experiment

3.6.1 Experimental setup.

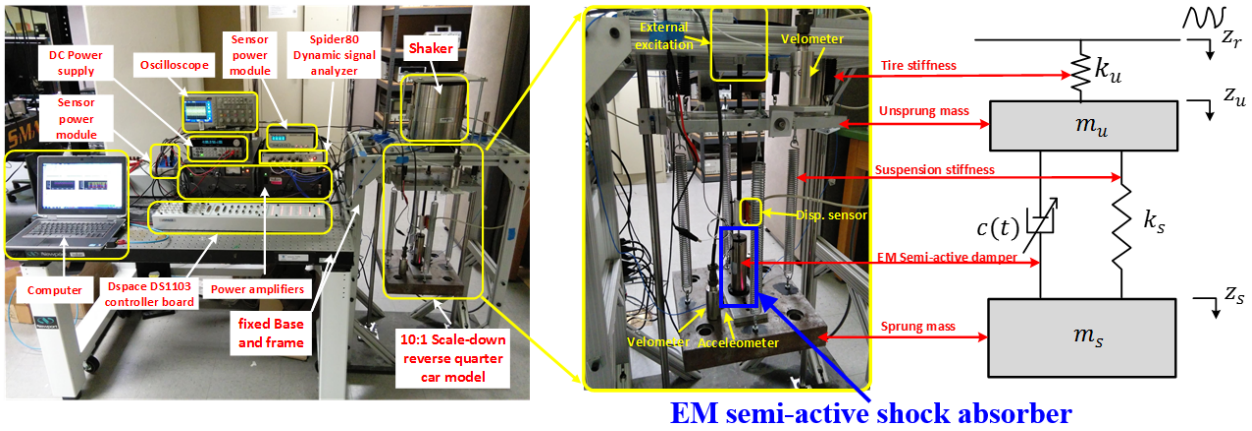

(a) (b)

Figure 3.11 (a) Overall experimental setup. (b) 10:1 scaled-down reverse quarter car model

Figure 3.11 (a) shows the overall experimental setup which includes a 10-to-1 scaled-down reverse quarter car test rig, a shaker, a dSPACE DS1103 controller board, a Spider-80 dynamic signal analyzer from Crystal Instrument, a computer and other instruments. Figure 3.11 (b) shows the 10-to-1 scaled-down reverse quarter car suspension and its dynamic model. The reverse quarter car suspension is still in the equilibrium due to its gravity being counteracted by the lift force of the springs hung on the fixed frame. The motions of the sprung mass and the unsprung mass are constrained only in the vertical direction by using linear guides and bearings. A voice coil motor is installed between the sprung mass and unsprung mass to emulate the electromagnetic semi-active damper. By adjusting the input voltage of this voice coil motor, its output force can be continuously set as desired damping force $c(t)(\dot{z}_s - \dot{z}_u)$ which is always linearly proportional to the relative velocity of the sprung mass and unsprung mass. A shaker is mounted on the fixed frame to provide the external excitations to the suspension system. Three accelerometers, two low-frequency velometers, one force sensor and one displacement sensor are mounted on the suspension system to measure the signals for the needs of semi-active control and system monitoring. The parameters of the 10-to-1 scaled-down quarter car suspension are listed in Table 3.4.

Table 3.4 Experiment parameters: 10:1 scaled-down quarter-car suspension

Parameters	Value	description
T_s	3.125[ms]	Dspace Sampling interval
m_s	37 [kg]	Sprung mass
m_u	6.37 [kg]	Unsprung mass
k_s	2.52 [kN/m]	Suspension stiffness
k_u	28.5 [kN/m]	Tire stiffness
c_{min}	30 [N/(m/s)]	Min. damping coeff.
c_{max}	400 [N/(m/s)]	Max. damping coeff.
c_n	150 [N/(m/s)]	Nominal constant damping
A	0.1 [inch]	The amplitude of sinusoid excitations

3.6.2 Justification of the scale-down quarter car test rig

In this section, we will show that the semi-active suspension system can be linearly scaled down. As mentioned above and in [6], the semi-active suspension system can be approximated as a linear suspension with a constant damping during a very short time period, in which the transfer function from road disturbance to the sprung mass acceleration is

$$\mathcal{L}\left\{\frac{\ddot{z}_s}{z_r}\right\}(s) = \frac{\frac{ck_u}{m_s m_u}s + \frac{k_s k_u}{m_s m_u}}{s^4 + (\frac{c}{m_s} + \frac{c}{m_u})s^3 + (\frac{k_s}{m_u} + \frac{k_u}{m_u} + \frac{k_s}{m_s})s^2 + \frac{ck_u}{m_s m_u}s + \frac{k_s k_u}{m_s m_u}} \tag{3.29}$$

If we scale down the suspension system by a scaled-down factor ρ, then the transfer function, from road disturbance to the sprung mass acceleration, of this scaled-down suspension system is

$$\begin{aligned}\mathcal{L}\left\{\frac{\ddot{z}_s}{z_r}\right\}(s) &= \frac{\frac{(\rho c)(\rho k_u)}{(\rho m_s)(\rho m_u)}s + \frac{(\rho k_s)(\rho k_u)}{(\rho m_s)(\rho m_u)}}{s^4 + \left(\frac{\rho c}{\rho m_s} + \frac{\rho c}{\rho m_u}\right)s^3 + \left(\frac{\rho k_s}{\rho m_u} + \frac{\rho k_u}{\rho m_u} + \frac{\rho k_s}{\rho m_s}\right)s^2 + \frac{(\rho c)(\rho k_u)}{(\rho m_s)(\rho m_u)}s + \frac{(\rho k_s)(\rho k_u)}{(\rho m_s)(\rho m_u)}} \\ &= \frac{\frac{ck_u}{m_s m_u}s + \frac{k_s k_u}{m_s m_u}}{s^4 + (\frac{c}{m_s} + \frac{c}{m_u})s^3 + (\frac{k_s}{m_u} + \frac{k_u}{m_u} + \frac{k_s}{m_s})s^2 + \frac{ck_u}{m_s m_u}s + \frac{k_s k_u}{m_s m_u}}\end{aligned} \tag{3.30}$$

By comparing (3.29) and (3.30), it is clear that the transfer function of the original suspension system and its linearly scaled-down system are identical. Therefore, the suspension system can be linearly scaled down and we choose $\rho = 1/10$ in our scaled-down test rig.

3.6.3 Experimental results

Figure 3.12 shows the experimental nonlinear frequency responses of the normalized sprung mass acceleration $\ddot{z}_s$ of SH-PDD, SH and PDD. It shows that the SH-PDD closely inherits the vibration isolation benefits of both SH and PDD, which agrees with the numerical analysis presented in Figure 3.4.

Figure 3.12 Experimental nonlinear frequency response of the normalized sprung mass acceleration $\ddot{z}_s$ of the proposed SH-PDD and the existing SH and PDD.

Figure 3.13 shows the experimental nonlinear frequency responses of the proposed SH-PDD and the existing SH-ADD. From Figure 3.13, it is clear that SH-PDD is similar to SH-ADD in effectively reducing the sprung mass acceleration across the whole frequency spectrum, which agrees with the numerical analysis presented in Figure 3.6(a).

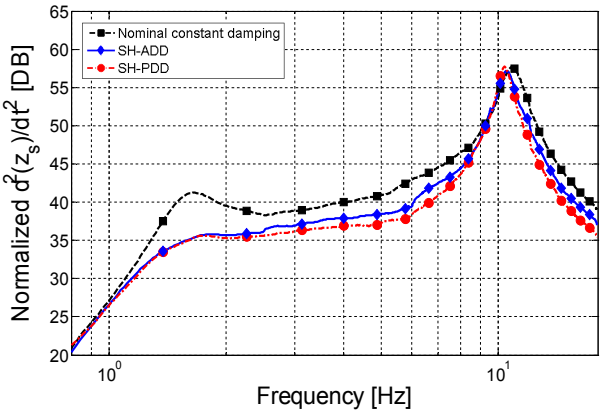

Figure 3.13 Experimental nonlinear frequency response of the proposed SH-PDD and the existing SH-ADD.

Figure 3.14 shows the experimental time-domain responses of the proposed SH-PDD under a single frequency excitation at 5.5 HZ, in comparison with that of the SH-ADD. As shown in Figure 3.14 (a), the SH-PDD is slightly better than the SH-ADD in attenuating the sprung mass acceleration. As shown in Figure 3.14 (b), SH-PDD significantly reduces the sprung mass jerk compared to SH-ADD. This result also agrees with the numerical analysis presented in Figure 3.7. Through comparison to the SH-ADD from the experimental results shown in Figure 3.12 - Figure 3.13, it is concluded that the SH-PDD is a new low-jerk semi-active control algorithm approaching the optimal limit of the semi-active control in terms of ride comfort.

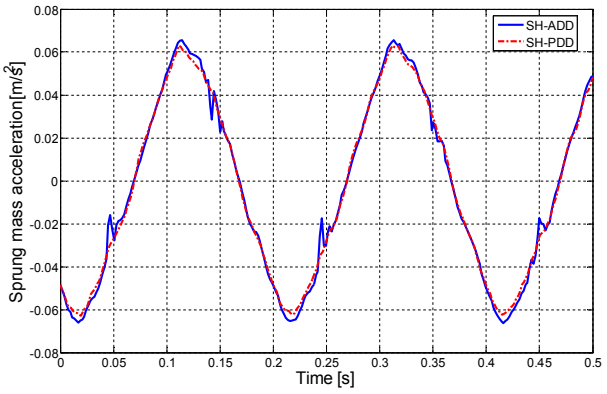

(a)

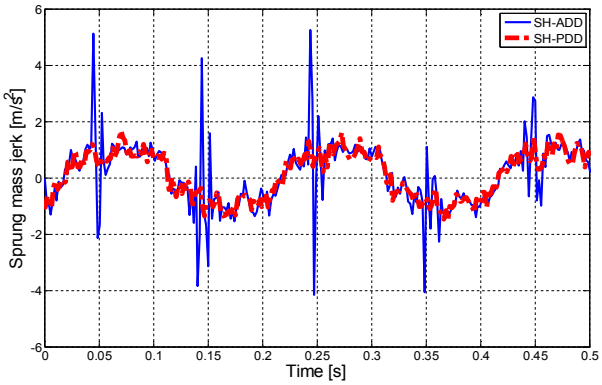

(b)

Figure 3.14 Experimental response of the single frequency excitation at 5.5 Hz (a) Sprung mass acceleration; (b) Sprung mass jerk.

3.7 Extension of the Proposed Switching Law

The proposed switching law is able to mix not only the Skyhook and PDD, but also other semi-active control algorithms. Some useful extensions of the proposed switching law are also given below.

By noticing the filtering benefits of the suspension with soft damping and hard damping in the low frequency range and high frequency range, respectively [6], we may mix hard damping c_{max} and soft damping c_{min} by using the proposed switching law to reduce the sprung mass oscillations. Thus, a new two-state sprung mass control algorithm, the mixed hard damping and soft damping$(c_{max} - c_{min})$, is proposed. Its concise control algorithm is given by

$$c_{c_{max}-c_{min}}(t) = \begin{cases} c_{max} & if\ \dot{z}_s^2 - \dot{z}_u^2 \geq 0 \\ c_{min} & else \end{cases} \tag{3.31}$$

The nonlinear frequency response of the $c_{max} - c_{min}$, from the road disturbance z_r to the sprung mass acceleration $\ddot{z}_s$, is shown in Figure 3.15. It is clear that the $c_{max} - c_{min}$ inherits the filtering benefits of hard damping and soft damping. Although the $c_{max} - c_{min}$ is less effective than the SH-PDD, it is able to reduce the sprung mass vibration across the whole frequency spectrum with very limited control efforts: only requiring a two-state electromagnetic semi-active damper and two velocity sensors.

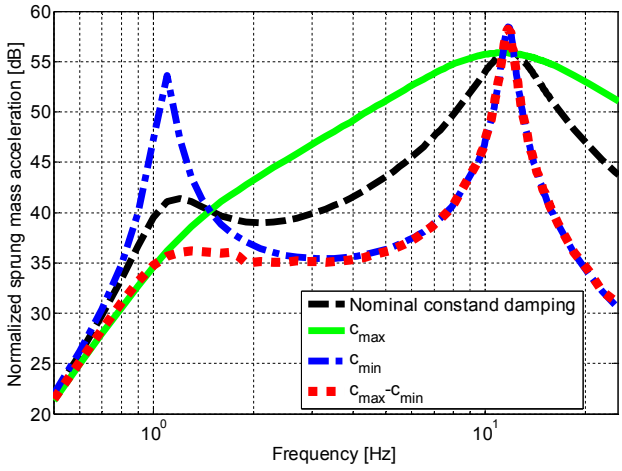

Figure 3.15 The nonlinear frequency response of the $c_{max} - c_{min}$ from the road disturbance z_r to the sprung mass acceleration $\ddot{z}_s$

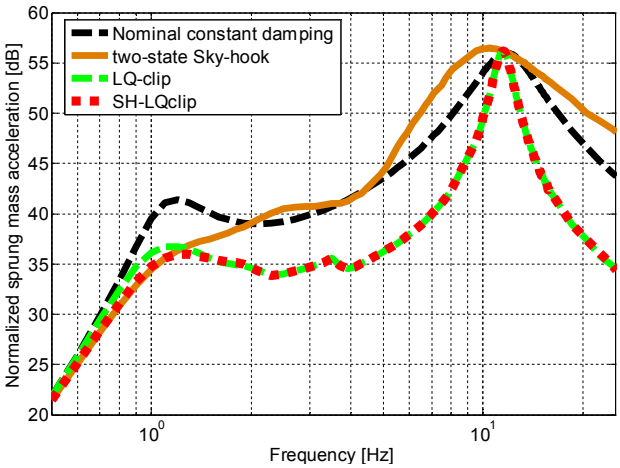

Figure 3.16 The nonlinear frequency response of the $SH - LQclip$ from the road disturbance z_r to the sprung mass acceleration $\ddot{z}_s$.

As proposed in [11], the classic clipped-optimal LQR control algorithm has superior isolation performance in the high frequency range among the existing control methods. Therefore, mixing SH and clipped-optimal control algorithms via the proposed switching law is also proposed to improve ride comfort when a continuous damper is available. So a new continuous sprung mass semi-active control algorithm, the mixed Sky-hook and clipped LQR (SH-LQclip), is given by

$$c_{\mathrm{SH-LQclip}}(t) = \begin{cases} c_{SH}(t) & if\ \dot{z}_s^2 - \dot{z}_u^2 \geq 0 \\ c_{LQclip}(t) & else \end{cases} \tag{3.32}$$

where $c_{LQclip}(t)$ is the clipped-optimal LQR control algorithm proposed in [11]. The nonlinear frequency response of the $SH - LQclip$, from the road disturbance z_r to the sprung mass acceleration $\ddot{z}_s$, is shown in Figure 3.16. It can be seen that the $SH - LQclip$ effectively inherits the filtering benefits of the Skyhook and the clipped-optimal LQR. Compared to the clipped-optimal LQR, $SH - LQclip$ slightly reduces the filtering performance around the first resonance, which is contributed by the characteristics of the Skyhook.

3.8 Chapter summary

In this chapter, we analyze the energy transfer abilities of vehicular suspension components between the sprung mass and the unsprung mass, and propose a new sprung mass control algorithm: the mixed Skyhook and Power-Driven-Damper (SH-PDD). The proposed algorithm defines a switching law that is capable of mixing Skyhook (SH) and Power-Driven-Damper (PDD), and simultaneously marries their advantages to achieve a better suspension performance.

The superior characteristics of the SH-PDD have been verified in the numerical analysis as well as experiments. As shown in the nonlinear frequency responses and the shock tests, the SH-PDD automatically marries the advantages of SH and PDD, effectively attenuating the sprung mass vibration across the whole frequency spectrum. As demonstrated in the single frequency excitation responses and the speed bump tests, the SH-PDD significantly lowers the jerk of the sprung mass while maintaining acceleration attenuation of the sprung mass, as compared to the SH-ADD. As shown by the random road disturbance tests, the proposed SH-PDD is effective at reducing the sprung mass vibration across the whole frequency spectrum, similar to SH-ADD and much better than SH, PDD and ADD, while eliminating the control chattering and high-jerk behaviors from suspension motion as occurred in SH-ADD. Since the SH-ADD is almost the optimal semi-active control algorithm in terms of ride comfort, it is concluded that the proposed SH-PDD is a new low-jerk semi-active suspension approaching the optimal limit in terms of ride comfort.

Therefore, the regenerative electromagnetic shock absorber can work as a semi-active controllable damper when its external resistive load is being adjusted. A linear regenerative electromagnetic shock absorber is used in the suspension control experiments, which verifies the function of the regenerative electromagnetic shock absorber in semi-actively controlling the vehicle suspension systems.

4 A Novel Regenerative Electromagnetic Shock Absorber with a Ball-screw-based Mechanical Motion Rectifier (MMR)

4.1 Chapter Introduction

Regenerative shock absorbers can effectively mitigate the vibration of vehicles while simultaneously harvesting the vibration energy otherwise dissipated by the traditional viscous damper. In this chapter, we develop a new type of MMR-based regenerative shock absorber using a ball screw and bevel gears with one-way sprag clutches embedded. The proposed shock absorber is composed of three modules which are the ball-screw, the enclosed MMR gearbox and the generator. Due to two one-way clutches, at any instant time only one bevel gear is engaged on the screw shaft and the other one idly rotates, the proposed shock absorber is able to convert the reciprocating vibration induced by the suspension vibration into the unidirectional rotation of the generator. Therefore, the proposed transmission system is named as Mechanical Motion Rectifier (MMR) which is in a similar sense as the electric voltage rectifier regulates an AC voltage. However, the MMR's advantages is well beyond the electric voltage rectifier. It can significantly increase the energy-harvesting efficiency by stabilizing the generator's rotational speed and improve the system reliability by reducing impact forces among transmission gears. In this chapter, we also analyzed the dynamics of the proposed ball-screw-based MMR shock absorber. It is derived that the shock absorber acts as a linear fixed inerter in parallel with a linear variable damper tuned by the external electrical loads of the generator. Moreover, we also derive the instants of one-way clutches engaging and disengaging from the screw shaft, which allow us to predict the rotational speed of the generator and the corresponding generated voltage and power. The analysis presented in this chapter can be extended to other types of energy-harvesting shock absorbers involving clutches-embedded gear transmissions, not only limited to the proposed ball-screw-based MMR shock absorber. In addition to the theoretical analysis, we also conduct lab and road tests to experimentally analyze and characterize the characteristics of the proposed shock absorber.

4.2 Design and Working Principles

As shown in Figure 4.1, the proposed shock absorber consists of three modules: the ball screw, the enclosed MMR gearbox and the generator. The ball screw and nut are employed in back-driven mode, that is, low-speed reciprocating motion of the nut induced by irregular suspension vibrations drives the screw to bi-directionally rotate at high speed. The nut can move along the linear guide in the ball-screw case. Such a structure ensures the stability and precision of the relative movement between the nut and screw and creates a fixed boundary condition to prevent the screw from buckling damages. The two eyelet connectors of the proposed shock absorber connect to the vehicle body and the wheel axle, respectively. To help the proposed shock absorber survive from shock induced by road obstacles, the eyelet connectors are filled with rubber buffers which act as additional springs and dampers.

Compared to rack-pinion mechanisms, the ball-screw mechanism can significantly reduce the backlash before the MMR mechanism, resulting in higher energy-harvesting efficiency. Also by using the ball-screw mechanism, an enclosed lubricated MMR gear transmission system can be designed, which increases the transmission durability and efficiency. However, the contact of the ball nut and screw causes additional friction. To reduce this friction, a highly lubricated large-lead screw is preferred to be used in the proposed shock absorber.

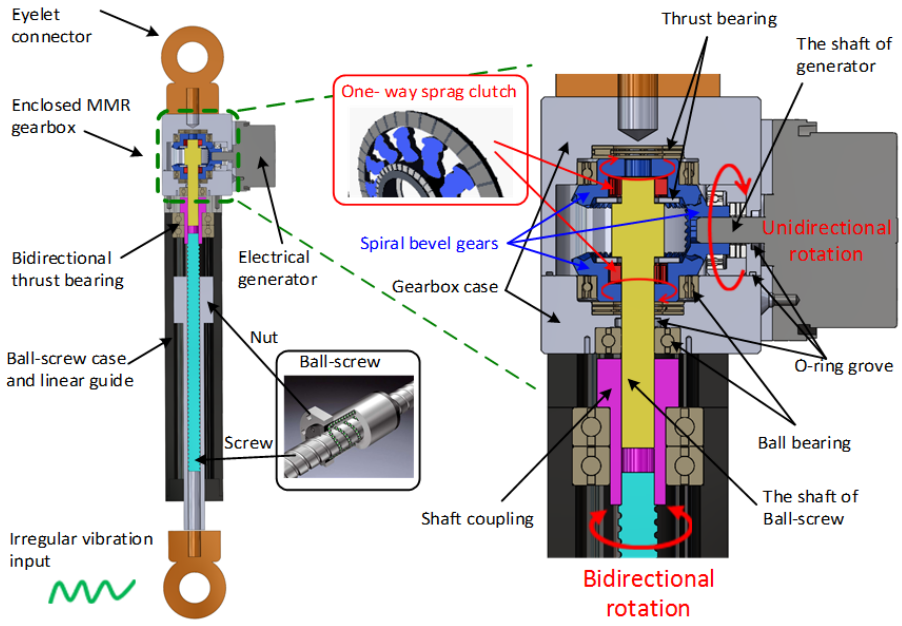

Figure 4.1 the design of ball-screw based shock absorber

The enclosed Mechanical Motion Rectifier (MMR) gearbox consists of one screw shaft, two one-way sprag clutches, two large and one small spiral bevel gears, bearings and lubricant sealing rings. The two one-way clutches are installed between the screw shaft and the large gears, which can only transmit torque in one direction and idly rotate in the other direction, in a similar function as those used in bicycle gears. Due to these one-way clutches, at any instant in time only one large bevel gear is engaged to the screw shaft, becoming the driving gear. For instance, in Figure 4.2(a), if the screw shaft rotates in the counter-clockwise direction (view from top to bottom), the lower clutch will engage on the screw shaft and the lower gear will become the driving gear to drive the generator to rotate in the clockwise direction (view from left to right). During this period, the upper clutch is disengaged from the screw shaft and the upper gear idly rotates. Similarly, in Figure 4.2(b), the clockwise rotation of the screw shaft will also drive the generator to rotate in the clockwise direction, in which the upper gear will become the driving gear and the lower gear will be the idle gear. In this way, the generator always rotates in one direction no matter whether the proposed shock absorber extends or compresses.

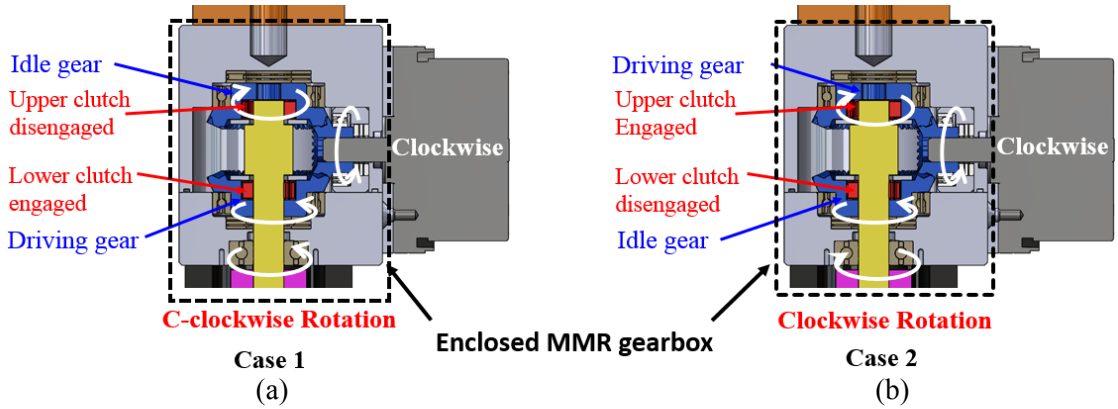

Figure 4.2 The reciprocating suspension vibration will drive the electrical generator to rotate in one direction using the proposed ball-screw-based mechanical motion rectifier (MMR).

Due to converting reciprocating vibration into unidirectional rotation of the generator, the proposed transmission system is named Mechanical Motion Rectifier (MMR) which is similar in a sense to electric voltage rectifiers used to regulate an AC voltage into DC voltage. However, MMR's advantages go well beyond electric voltage rectifiers. The unidirectional rotation enables the generator to operate steadily in its high-efficiency working condition from the oscillatory

vibration of suspensions induced by road roughness. Such a feature increases the energy conversion efficiency and reduces the impact force commonly caused by oscillatory motions.

The prototype is shown in Figure 4.3 and the corresponding parameters are listed in Table 4.1. The parameters selection is briefly summarized as follows. First, in order to maintain a high electrical efficiency, we choose the nominal external resistance approximately 9 times larger than the internal resistance of the generator. With this total resistance, we can properly choose the gear transmission ratios (r_b, r_g), the screw lead and diameter (l and d_m) so that the nominal equivalent damping of the proposed shock absorber is suitable to the vehicles we are targeting. In this paper, we are targeting heavy-duty trucks or buses whose typical damping is around 8 - 10 kNs/m. The relation between the equivalent damping and the corresponding design parameters are derived in Equation (4.13) in Section 4.3. More specifically, first we want to choose the ball screw whose lead angle $\lambda = \arctan(\frac{l}{\pi d_m})$ is as large as possible so that the ball-screw induced friction is reduced and the mechanical efficiency is increased. Then the gear transmission ratio will be selected accordingly.

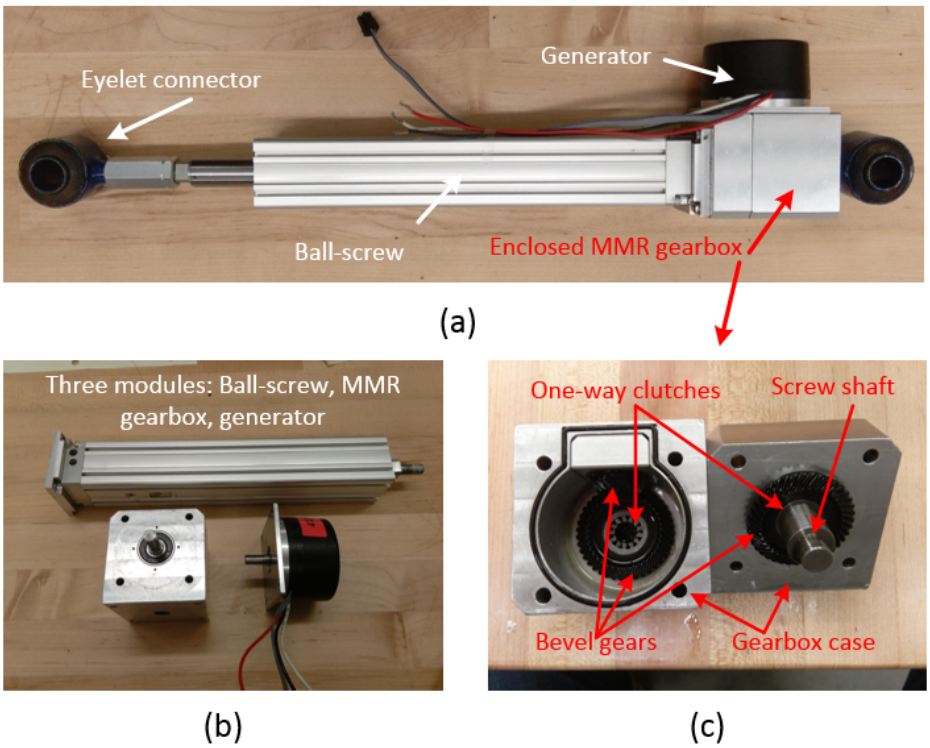

Figure 4.3 the Prototype of ball-screw-based MMR shock absorber (a) the overall shock absorber (b) three independent modules (c) inside structure of MMR gearbox

Table 4.1. The parameters of the prototype

Parameters	Value	description
d_m	8[mm]	Screw diameter
l	6[mm]	Ball-screw lead
f	0.15	Ball-screw friction factor
J_m	1.21 [kgcm^2]	Generator inertia
J_{lg}	0.1[kgcm^2]	Large gear inertia
J_{sg}	0.0065[kgcm^2]	Small gear inertia
J_{bg}	0.02[kgcm^2]	Screw inertia
r_b	2	MMR bevel gear transmission ratio
r_g	1	Generator gearhead ratio
k_e	0.114 [V/rads]	Generator voltage constant
k_t	0.114 [Nm/A]	Generator torque constant
R_i	1.1 [ohm]	Internal resistance per phase
L	0.864[mH]	Internal inductance per phase
Length	600 [mm]	Shock absorber length
Strokes	150 [mm]	Shock absorber stroke
Weight	3.25 [Kg]	Shock absorber weight

4.3 Modeling and Dynamics

4.3.1 The dynamics of the generator

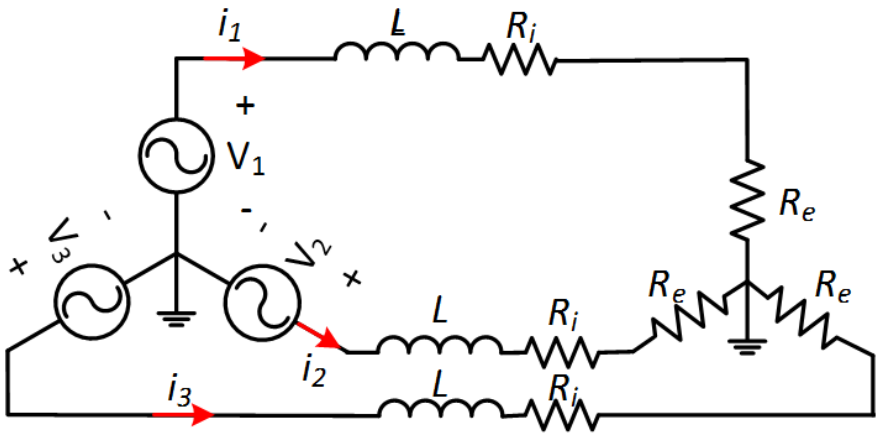

Figure 4.4 The dynamic model of a three-phase generator

A three-phase generator has been adopted in the proposed energy-harvesting shock absorber. The dynamic model of the generator is shown in Figure 4.4, where V_1, V_2 and V_3 are the induced electromagnetic force (EMF) generated by the respective phase of the generator. i_1, i_2 and i_3 are the corresponding phase current of the generator. L and R_i are the inductance and resistance of the voice coil per phase. R_e is the external resistive electrical load per phase. The dynamics of the generator and its electrical damping have been analyzed in [24-25]. The resisting torque caused by electrical damping of the three-phase generator is [25]

$$\tau_{emf} = \frac{3k_t k_e}{2R}\frac{d\theta}{dt} \tag{4.1}$$

where $R = R_i + R_e$, k_e and k_t are the voltage constant and torque constant of the generator, and θ is the angular displacement of the generator. To make the model more accurate in this paper, we also take into account the friction of the generator including both Coulomb friction and viscous damping, which may be written as

$$\tau_{fric} = c_v\frac{d\theta}{dt} + \tau_0 sgn(\frac{d\theta}{dt}) \tag{4.2}$$

where τ_{fric} is the friction torque of the generator, c_v is the viscous damping coefficient, and τ_0 is the Coulomb friction torque, indicating that the friction torque opposes the direction of motion (sgn($\frac{d\theta}{dt}$) just returns the sign of $\frac{d\theta}{dt}$). According to Newton's law, the rotor's acceleration, $\frac{d^2\theta}{dt^2}$, is proportional to the total torque applied on the rotor of the generator

$$\tau_m - \tau_{emf} - \tau_{fric} = J_m\frac{d^2\theta}{dt^2} \tag{4.3}$$

where τ_m is input mechanical torque, J_m is rotor's rotational inertia. Substituting Equations (4.1) and (4.2) into Equation (4.3), the overall dynamics of the generator can be derived as

$$\tau_m = J_m\frac{d^2\theta}{dt^2} + c_m\frac{d\theta}{dt} + \tau_0 sgn(\frac{d\theta}{dt}) \tag{4.4}$$

where c_m is the equivalent torsional damping of the generator contributed by both electrical damping and viscous damping

$$c_m = \frac{3k_t k_e}{2R} + c_v \tag{4.5}$$

The Coulomb friction torque τ_0 is usually very small and negligible in most of generators. Therefore, the generator can be simplified as a torsional inerter J_m in parallel with a torsional damper $c_m = \frac{3k_t k_e}{2R} + c_v$.

4.3.2 The dynamics of ball-screw-based MMR shock absorbers

Figure 4.5 shows the dynamic model of the ball-screw-based MMR shock absorber. Unlike linear and rotary energy-harvesting shock absorbers [14-25], the MMR-based energy-harvesting shock absorber has non-linear behaviors induced by the switching between engagement and disengagement of one-way clutches. When the rotational speed of the screw shaft is smaller than that of the large bevel gears, the one-way clutches inside the large gears will disengage from the screw shaft, resulting zero torque transmission. When the system is engaged, the screw shaft τ_{bs} drives the system including the MMR gear transmission system and the generator. During this period, the following transmission relations hold.

$$\frac{d\theta}{dt} = \frac{d\theta_{in}}{dt} \tag{4.6}$$

$$\tau_{sg} - r_g \tau_m = \frac{J_{sg}}{r_g} \frac{d^2\theta}{dt^2} \tag{4.7}$$

$$\tau_{lg} - r_b \tau_{sg} = \frac{2J_{lg}}{r_b r_g} \frac{d^2\theta}{dt^2} \tag{4.8}$$

$$\tau_{bs} - \tau_{lg} = \frac{J_{bs}}{r_b r_g} \frac{d^2\theta}{dt^2} \tag{4.9}$$

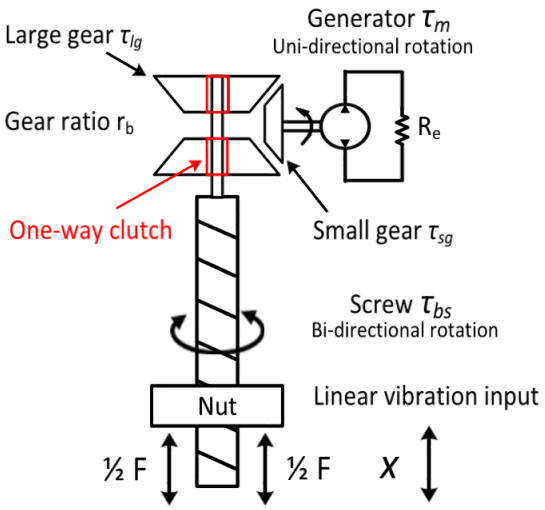

Figure 4.5 The dynamic model of ball-screw-based MMR shock absorber

where $\frac{d\theta_{in}}{dt} = \frac{r_b r_g}{l}\left|\frac{dx}{dt}\right|$ is defined as input rotational speed. x is the linear relative displacement of the shock absorber and l is the screw lead. r_b and r_g are the transmission ratio of the bevel gears and planetary gears. τ_{sg}, τ_{lg} and τ_{bs} are the torque of the small gear, the large gear and the screw shaft, respectively. J_{sg}, J_{lg} and J_{bs} are the rotational inertia of the small gear, the large gear and the screw shaft, respectively. The thrust force applied on the ball nut is proportional to the torque of the screw shaft [48]

$$F_e = \frac{2\tau_{bs}}{d_m}\left(\frac{\pi d_m + fl}{l - \pi f d_m}\right) \tag{4.10}$$

where d_m is the pitch diameter of the screw and f is the friction coefficient. Combining Equations (4.4) - (4.9), the thrust force of the engaged shock absorber can be expressed as

$$F_e = \left[\left(\frac{\pi d_m + fl}{l - \pi f d_m}\right)\frac{2\left(r_b^2 r_g^2 J_m + r_b^2 J_{sg} + 2J_{lg} + J_{bs}\right)}{d_m l}\right]\frac{d^2x}{dt^2} + \left[\left(\frac{\pi d_m + fl}{l - \pi f d_m}\right)\frac{2r_b^2 r_g^2}{d_m l}\left(\frac{3k_t k_e}{2R} + c_v\right)\right]\frac{dx}{dt} \tag{4.11}$$

Equivalently, the engaged shock absorber acts as a linear fixed inerter in parallel with a linear variable damper tuned by the electrical load of the generator, as shown in Figure 4.6. The equivalent inertance and damping are

$$m_e = \left(\frac{\pi d_m + fl}{l - \pi f d_m}\right) \frac{2\left(r_b^2 r_g^2 J_m + r_b^2 J_{sg} + 2J_{lg} + J_{bs}\right)}{d_m l} \approx \left(\frac{\pi d_m + fl}{l - \pi f d_m}\right) \frac{2 r_b^2 r_g^2 J_m}{d_m l} \tag{4.12}$$

$$c_e = \left(\frac{\pi d_m + fl}{l - \pi f d_m}\right) \frac{2 r_b^2 r_g^2}{d_m l} \left(\frac{3 k_t k_e}{2R} + c_v\right) \tag{4.13}$$

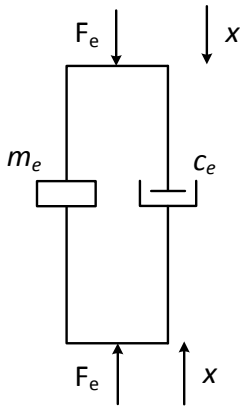

Figure 4.6 The equivalent dynamic model of ball-screw-based MMR shock absorber when it is in the engaged stage

In Equation (4.12), the contribution of the rotational inertias of the gears and screw, $r_b^2 J_{sg} + 2J_{lg} + J_{bs}$, is much smaller than that of the generator $r_b^2 r_g^2 J_m$, which is especially true when the transmission ratios r_b and r_g are large. For instance, in the proposed design, $r_b^2 r_g^2 J_m = 4.82\text{kgcm}^2$ is approximately 20 times larger than $r_b^2 J_{sg} + 2J_{lg} + J_{bs} = 0.246\text{kgcm}^2$. Therefore, the equivalent inertance m_e of the shock absorber is mainly dominated by the rotational inertia of the generator and $r_b^2 J_{sg} + 2J_{lg} + J_{bs}$ is negligible.

On the other hand, when the input rotational speed is smaller than the rotational speed of the generator, disengagement of the MMR occurs.

$$\frac{d\theta_{in}}{dt} < \frac{d\theta}{dt} \tag{4.14}$$

During this period, the generator drives the gear transmission system at a higher speed than that of the screw shaft due to the kinetic energy stored in the inertia of the mechanical elements, such as gears or the rotor of the generator. However, this rotational speed will gradually decrease due to

the electrical load of the generator, which converts kinetic energy into electricity. When the input rotational speed $\dot{\theta}_{in}$ is again equal to the rotational speed of the generator $\dot{\theta}$, the one-way clutches get re-engaged and start transmitting torque to the generator. During the disengaged period, the screw shaft doesn't transmit any torque to the generator and thus the force of the shock absorber is zero

$$F_d = 0 \tag{4.15}$$

To sum up, the force of the proposed MMR-based shock absorber is given by

$$\begin{cases} F_e = m_e \frac{d^2x}{dt^2} + c_e \frac{dx}{dt} & \dot{\theta} = \dot{\theta}_{in}, \quad engaged\ period \\ F_d = 0 & \dot{\theta} > \dot{\theta}_{in},\ disengaged\ period \end{cases} \tag{4.16}$$

where m_e and c_e can be solved from Equation (4.12) and (4.13). It is worth noting that all the mechanical energy in the primary suspension system will be kept conservatively during disengaged period since the primary system becomes an undamped system. Ideally, the proposed design won't cause additional mechanical energy loss during disengaged period.

4.3.3 The rotational speed of the generator and the generated power

Since any arbitrary vibration sources can be decomposed into a series of sinusoidal functions, the proposed shock absorber is analyzed when subjected to sinusoidal vibration inputs.

$$\begin{cases} x = Asin(\omega t) \\ \frac{dx}{dt} = A\omega cos(\omega t) \\ \frac{d^2x}{dt^2} = -A\omega^2 sin(\omega t) \end{cases} \tag{4.17}$$

where A is the amplitude and ω is the angular frequency of the sinusoidal vibration input.

As explained above, when the MMR is disengaged, the torque of the screw shaft τ_{bs} falls down to zero. Neglecting the rotational inertia of gears, we can obtain the governing equation of the generator when the MMR is disengaged

$$J_m \frac{d^2\theta}{dt^2} + c_m \frac{d\theta}{dt} = 0 \tag{4.18}$$

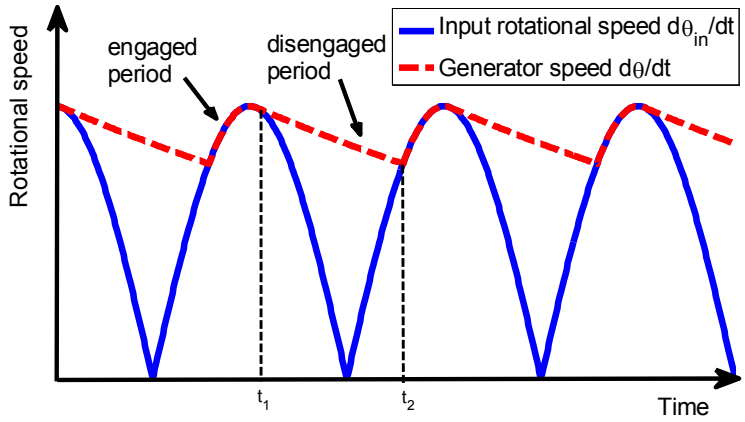

Figure 4.7 The switching of the engagement and disengagement inside the mechanical motion rectifier. $\theta_{in} = \frac{r_b r_g}{l}|x|$ and θ is the angular displacement of the generator.

Figure 4.7 shows the switching dynamics of the engagement and disengagement inside the MMR. At t_1,

$$\frac{d\theta}{dt} = \frac{d\theta_{in}}{dt} \tag{4.19}$$

and the one-way clutch starts disengaging from the screw shaft. At this time, the input angular acceleration can be obtained using Equation (4.17)

$$\frac{d^2\theta_{in}}{dt^2} = \frac{r_b r_g}{l}\frac{d^2x}{dt^2} = -\frac{r_b r_g}{l} A\omega^2 sin(\omega t_1) \tag{4.20}$$

and the angular acceleration of the generator is

$$\frac{d^2\theta}{dt^2} = -\frac{c_m}{J_m}\frac{d\theta}{dt} = -\frac{c_m}{J_m}\frac{d\theta_{in}}{dt} = -\frac{c_m}{J_m}\frac{r_b r_g}{l} A\omega cos(\omega t_1) \tag{4.21}$$

When disengagement occurs at t_1,

$$\frac{d^2\theta_{in}}{dt^2} \leq \frac{d^2\theta}{dt^2} \tag{4.22}$$

Substituting Equations (4.20) and (4.21) into Equation (4.22), we can solve for t_1

$$\tan(\omega t_1) = \frac{c_m}{\omega J_m} \tag{4.23}$$

Thus, the instant t_1 when the MMR starts to disengage is

$$t_1 = \frac{1}{\omega}\arctan\left(\frac{c_m}{\omega J_m}\right) + \frac{K\pi}{\omega}, \quad K = 0,1,2,3\cdots \tag{4.24}$$

During its disengaged period, the rotation of the generator is governed by Equation (4.18). Therefore the rotational speed of the generator during the disengaged period can be obtained as

$$\frac{d\theta}{dt} = \frac{d\theta}{dt}(t_1) * e^{\frac{-c_m}{J_m}(t-t_1)}, \quad t_1 \leq t \leq t_2 \tag{4.25}$$

where $\frac{d\theta}{dt}(t_1) = \frac{r_b r_g}{l} A\omega|cos(\omega t_1)|$. When the system becomes re-engaged at t_2, the rotational speed of the generator is equal to $\frac{d\theta_{in}}{dt}$. Therefore, at t_2,

$$\frac{d\theta_{in}}{dt}(t_1) * e^{\frac{-c_m}{J_m}(t_2-t_1)} = -\frac{d\theta_{in}}{dt}(t_2), \quad t_1 \leq t_2 \leq t_1 + \frac{\pi}{\omega} \tag{4.26}$$

Equation (4.26) can be reformed as

$$cos(\omega t_1)\, e^{\frac{c_m}{J_m}t_1} + cos(\omega t_2)\, e^{\frac{c_m}{J_m}t_2} = 0, \; t_1 \leq t_2 \leq t_1 + \frac{\pi}{\omega} \tag{4.27}$$

Then, the corresponding t_2 can be solved from Equation (4.27) for every t_1 with a different K. To sum up, the rotational speed of the generator is governed by the following equations

$$\begin{cases} \frac{d\theta}{dt} = \frac{d\theta_{in}}{dt} & t_2 \le t \le t_1 \\ J_m \frac{d^2\theta}{dt^2} + c_m \frac{d\theta}{dt} = 0 & t_1 < t < t_2 \end{cases} \quad K = 0,1,2,3\cdots \tag{4.28}$$

where t_1 and t_2 with different K are solved from Equations (4.24) and (4.27).

Once the rotational speed of the generator is obtained, the generated voltage is $k_e \frac{d\theta}{dt}$ and the electrical power envelop per phase can be solved by

$$P_e = \frac{{k_e}^2}{R}\left(\frac{d\theta}{dt}\right)^2 \tag{4.29}$$

It should be noted that the rotational speed of the generator derived above can be easily extended to other types of MMR-based mechanisms by simply defining a different input rotational speed θ_{in}. Figure 4.8(a) shows the simulation results of the rotational speed of the generator when the shock absorber is subjected to a 4 Hz sinusoidal excitation with $\pm$2mm amplitude and 10Ω external electrical loads. Figure 4.8 (b) shows the corresponding simulated power envelop per phase.

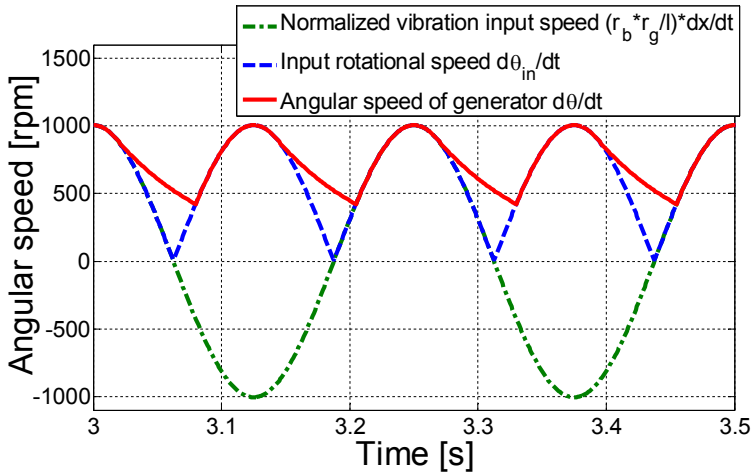

(a)

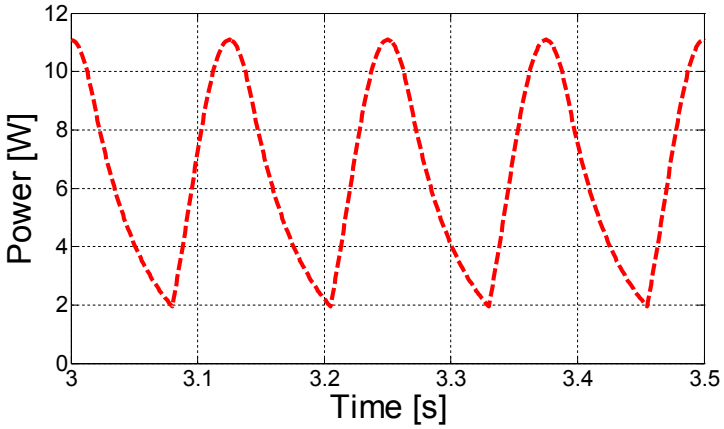

(b)

Figure 4.8 (a) Simulated rotational speed of the generator. (b)Simulated power envelop per phase. The shock absorber is subjected to harmonic vibration inputs of 4 Hz frequency with ±2mm amplitude and 10Ω external electrical loads.

4.4 Lab experiments and Analysis

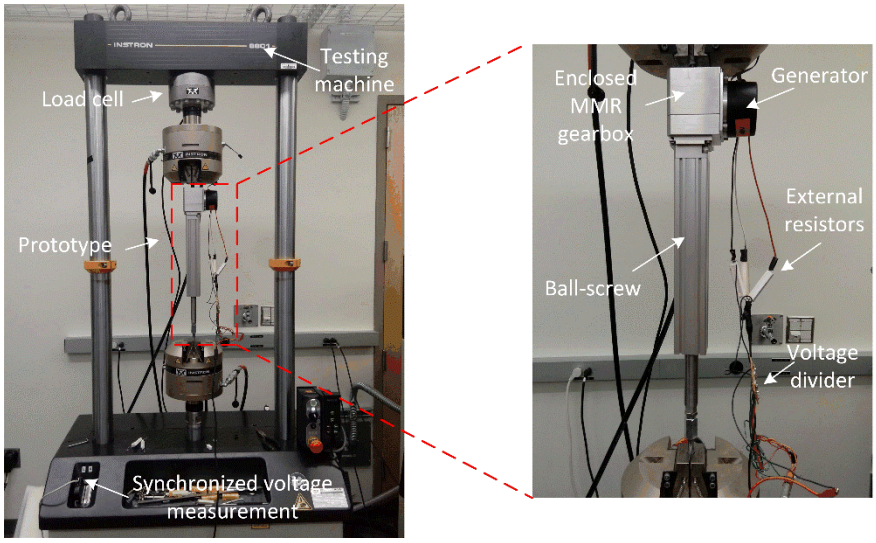

Figure 4.9 Experimental setup

4.4.1 Experimental setup

As shown in Figure 4.9, the shock absorber prototype was tested on an Instron testing machine which has a built-in load cell and a displacement sensor to record the force and displacement data.

In addition, an extensible analog-to-digital input channel of the testing machine was used to simultaneously measure the voltage across the external resistors. A series of sinusoidal inputs, with the frequency ranging from 1Hz to 10 Hz and the amplitude ranging from ±0.5mm to ±5mm, were used to excite the shock absorber prototype during the tests. The external electrical loads were connected to the three-phase generator in a "Y" configuration [49], as shown in Figure 3. A 1-to-41 voltage divider was used to measure the voltage across the external resistors. The dynamic and energy-harvesting characteristics of the shock absorber prototype are presented in the following subsections.

4.4.2 Force-displacement loops and damping characteristics

Since suspensions experience vibration over a broadband spectrum, mainly 1-10Hz [38], the performance of the proposed shock absorber was investigated for various excitation frequencies. Figure 4.10 (a) shows the force-displacement loops for different excitation frequencies ranging from 1Hz to 10Hz under harmonic vibration inputs of 2mm amplitude with 10 Ω external electrical loads. The results show that the higher the frequency of the excitation, the larger damping force the shock absorber achieves. This result agrees with the force of the engaged shock absorber derived in Equation (4.11). The results in Figure 4.10 (a) also indicate that the shock absorber starts engaging earlier when the excitation frequency is smaller, which corresponds to a shorter disengaged period $t_2 - t_1$ that agrees with the results in equation (4.24) and (4.27). This also explains why the peak force is shifted from the left to the right when the excitation frequency is increased from 1Hz to 10Hz. In Figure 4.10(a), the fluctuation of the damping force is also observed at 1Hz excitation frequency. This is because the generator rotates at low speeds when the vibration input is slow, which will cause the effect of torque fluctuation of the 3-phase generator due to uneven distribution of the magnets inside the generator. This force fluctuation phenomenon may lightly degrade suspension dynamic performance, especially when vehicle speed is low. In order to reduce this fluctuation, we can choose the DC-brush generator in which the magnets are more evenly distributed. Alternatively, we can also increase the gear transmission ratio so that the generator also rotates at a relatively high speed even under low-frequency excitations. A larger damping will be also achieved if the transmission ratio is increased.

Figure 4.10(b) shows force-displacement loops for different electrical loads under harmonic

vibration inputs of 5Hz frequency and $\pm$2mm amplitude. The results show that the forces fall down to zero before the displacements reach their maximum or minimum. This is because the kinetic energy stored in the generator inertia is returned to the system and the one-way clutch is disengaged at this area, which agrees with the analysis in Section 4.3. Moreover, the results indicate that the smaller the electrical load is, the shorter the disengaged period is. This is because the equivalent damping of the shock absorber becomes larger when the electrical load is smaller. The larger damping will cause the generator to slow down faster during the disengaged periods and thus the generator will be reengaged with the system in a shorter time period.

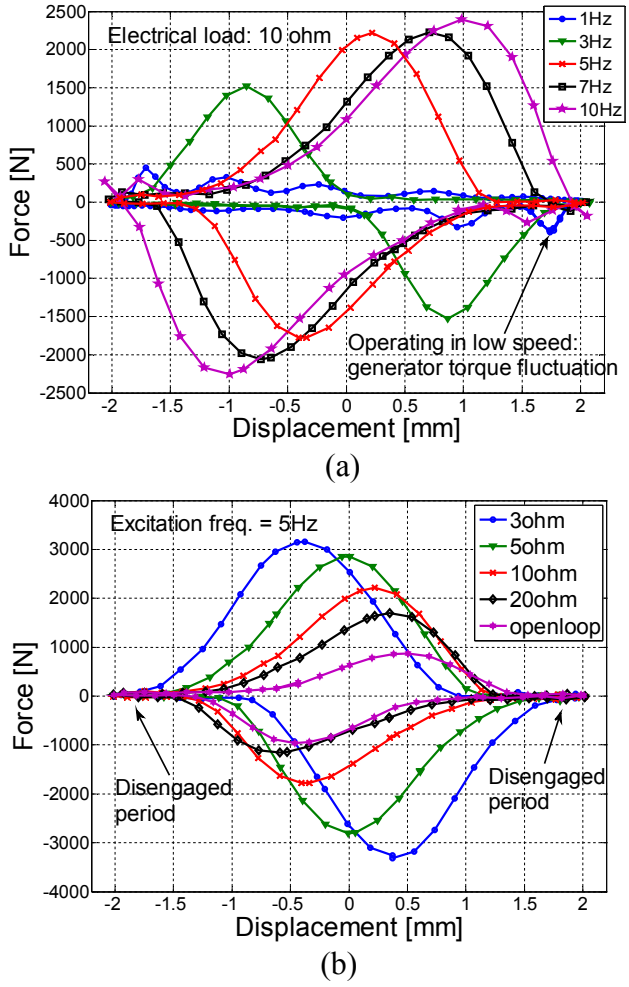

Figure 4.10. Force-displacement loops under harmonic vibration inputs of A = $\pm$2mm. (a) for different excitation frequencies with external electrical load $R_e = 10\Omega$. (b) for different external electrical loads with frequency 5Hz.

Figure 4.11 shows the damping loops for different amplitudes at vibration inputs of 5Hz frequency and 10Ω electrical load. The results in Figure 4.11 show that the damping force is proportional to the excitation amplitude when other conditions are remained. This indicates that the proposed shock absorber roughly keeps linear behaviours with respect to the excitation amplitude.

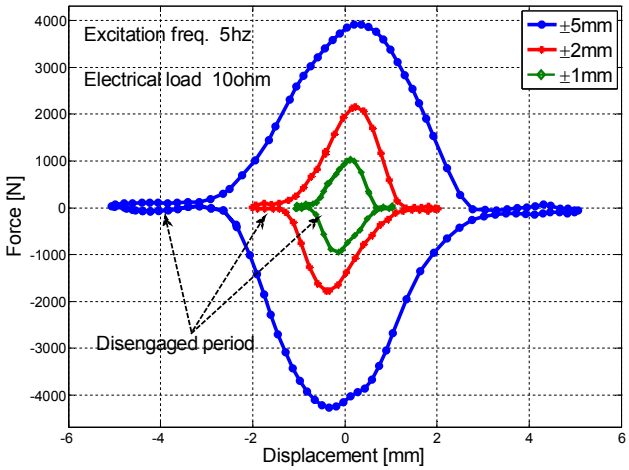

Figure 4.11 Force-displacement loops for different amplitudes at harmonic vibration inputs of 5Hz frequency and 10Ω electrical load.

In Figures 4.10-4.11, the area of the force-displacement loop represents the mechanical work input of the shock absorber ΔW during one work cycle. Therefore, the mechanical power input can be obtained by [24]

$$P_m = f * \Delta W \tag{4.30}$$

where f is the frequency of the vibration input. Moreover, the equivalent damping coefficient can be calculated as [24]

$$c_{eq} = \frac{\Delta W}{2\pi^2 f X^2} \tag{4.31}$$

where X is the amplitude of the harmonic vibration input. Based on Equation (4.31), the equivalent

damping of the shock absorber prototype is calculated for different electrical loads under vibration inputs of 2Hz frequency close to the first resonance of vehicle suspensions, as shown in Figure 4.12. The results show that the smaller the electrical load is, the larger damping force and damping coefficient the shock absorber can achieve. Figure 4.12 also shows that the minimum damping 4425 Ns/m is achieved when the shock absorber is in open-loop status. This means the damping of the shock absorber contributed by the viscous damping of the generator $c_v \left(\frac{\pi d_m + fl}{l - \pi f d_m}\right) \frac{2r_b^2 r_g^2}{d_m l} =$ 4425 Ns/m. Then we can properly predict the damping of the shock absorber, which is also plotted in Figure 4.12. The results also show that the damping of the shock absorber with a 10Ω electrical load is 8205Ns/m which is typically suitable to trucks or buses. This is why we study the performance of the proposed shock absorber with 10Ω electrical loads in detail. In addition, Figure 4.12 indicates that the damping range of the proposed shock absorber is 4.43kNs/m – 15.42kNs/m, which can be changed by adjusting the electrical loads. In comparison, the typical suspension damping for passenger cars is 1.5kNs/m [50], for heavy-duty trucks or buses are 8-10kNs/m [51-52].

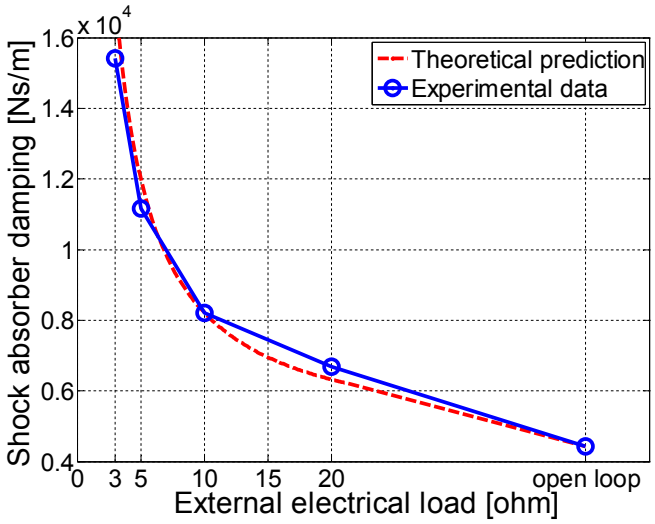

Figure 4.12 Equivalent damping for different electrical loads at vibration inputs of 2Hz frequency

4.4.3 Energy harvesting and efficiency

The generated voltage V per phase was recorded during the tests and the instantaneous electrical power per phase can be calculated as

$$P_s = \frac{V^2}{R} \tag{4.32}$$

where V is the instant phase voltage. The average of total power generated by the three-phase generator can be obtained as

$$P_{ave} = 3 \times \frac{\int_0^T P_s \, dt}{T} \tag{4.33}$$

which means calculating the average over T time period.

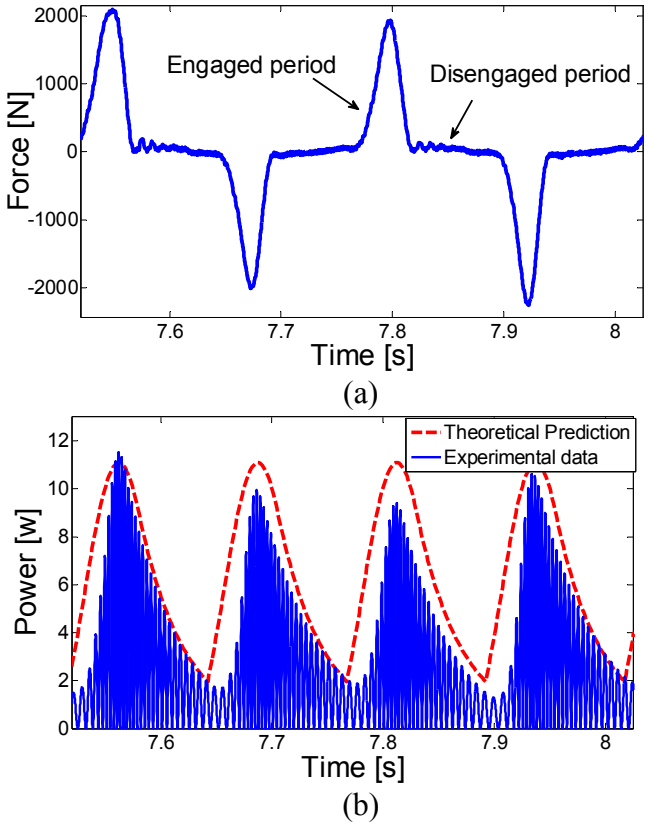

Figure 4.13 (a) Measured force (b) Measured and Simulated phase power under harmonic excitations with 4Hz frequency, $R_i + R_e$=11.1 Ω total electrical load and ±2mm amplitude. (Max. power = 11.52 W, Ave. power = 2.25W)

Figure 4.13 (a)-(b) show the simulated and measured electrical power per phase together with the shock absorber force under harmonic excitations with 4Hz frequency, 10+1.1=11.1 Ω total electrical load and ±2mm amplitude. Under such a condition, the maximum phase power is around 11.52 watts and the average phase power is 2.25 watts. Figure 10(b) also shows that the proposed MMR-based shock absorber can stabilize the rotational speed of the generator to never fall to zero as occurs in linear and rotary energy harvesters [14-25]. The asymmetric shape of the generated power is also observed, as the upward slope of the generated power is larger than the downward slope. This is because the generator is disengaged from the ball screw during the downward slope, which corresponds to a slow deceleration of the generator speed, as is also shown in Figure 4.8. Note that the power harvested also increases as the amplitude and the frequency of vibration inputs increase.

The total energy-harvesting efficiency of the system can be decomposed into the electrical efficiency η_e and the mechanical efficiency η_m. The electrical efficiency is the ratio of power on the external electrical load to the total electrical power, which is the R_e divided by the total resistance $R_e + R_i$. The mechanical energy-harvesting efficiency is defined as the ratio of total electrical power to mechanical input power. The mechanical and electrical efficiency of the proposed shock absorber for different external electrical loads $R_e = 3 - 20\Omega$ and different input amplitudes $A = \pm 1 - \pm 5mm$ under 2Hz harmonic excitations is shown in Figure 4.14(a). In this prototype, the internal resistance $R_i = 1.1\Omega$ and the electrical efficiency η_e is 73.2% - 94.7% for $R_e = 3 - 20\Omega$.

As shown in Figure 4.14(a), the mechanical efficiency ranges from 27% to 57.9% when $A = \pm 2mm$. The mechanical efficiency η_m increases when the electrical load decreases. The total energy harvesting efficiency is from 25.6% to 42.4% for $R_e = 3 - 20\Omega$ at 2Hz excitation frequency and 2mm amplitude.

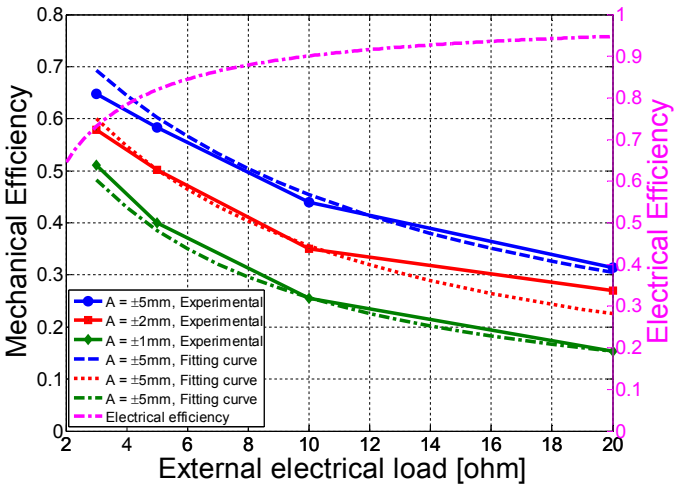

(a)

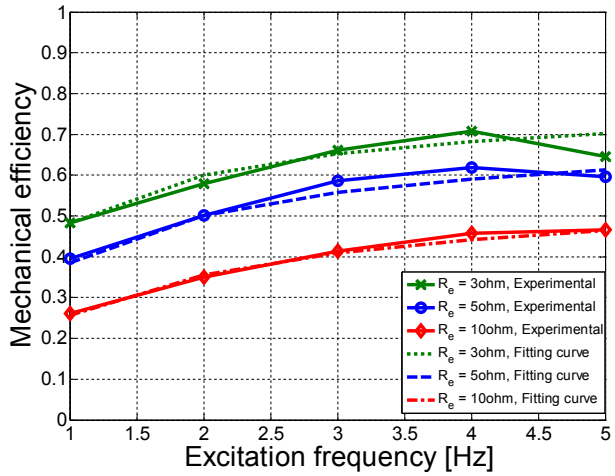

(b)

Figure 4.14 Mechanical efficiency (a) for different electrical loads and different amplitudes under vibration inputs of 2Hz frequency, (b) for different excitation frequencies and different electrical loads under vibration inputs of $\pm$2mm amplitude.

The mechanical efficiency of the system under different excitation frequencies with $R_e = 3 - 10\Omega$ is presented in Figure 4.14 (b). The results show that the mechanical efficiency increases as the excitation frequency increases. The highest mechanical efficiency 70.1% is achieved at 4Hz excitation frequency and $R_e = 3\Omega$. The total energy harvesting efficiency is from 35.9% to 51.9% for 1Hz to 5Hz excitation frequency with $R_e = 3\Omega$. The mechanical efficiency 70.1% is higher than previous rotary or MMR-based energy harvesters mentioned in the introduction. For the proposed design, there are trade-offs between damping performance and energy-harvesting performance. The maximum damping of the shock absorber is achieved when the generator is

short-circuited, but in this case, the harvested energy would be zero. However, it should be noted that the maximum damping may not be the desired damping in vehicle suspension systems.

4.4.4 Efficiency comparison of ball-screw-based MMR shock absorber and rack-pinion-based MMR shock absorber [26]

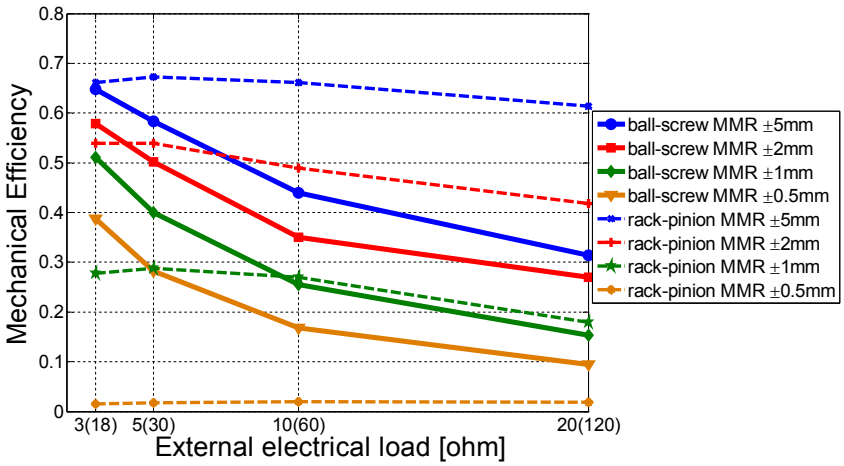

Figure 4.15 Mechanical efficiency of the ball-screw-based MMR energy harvester (solid line) and rack-pinion-based MMR energy harvester [26] (dash line) under harmonic vibration inputs of ±0.5mm to ±5mm amplitude and 2Hz frequency.

Figure 4.15 shows the comparison of the mechanical efficiency between the ball-screw-based MMR shock absorber and rack-pinion-based MMR shock absorber [26] under harmonic vibrations of different amplitudes and electrical loads. To make a fair comparison, the electrical efficiency of these two types of MMR-based shock absorbers are kept the same, that is, the external load of the rack-pinion MMR shock absorber is 6 times larger than that of the proposed ball-screw-based one. It is observed that the mechanical efficiency of the rack-pinion shock absorber dramatically decreases as the vibration amplitude decreases, and ceases to work in excitations below A = ±0.5mm due to the backlash between the rack teeth and pinion teeth. However, the ball-screw shock absorber can still generate power under small excitation conditions. This low-backlash feature can increase the energy harvesting efficiency of the proposed shock absorber, especially when vehicles are running on smooth highways. The results in Figure 4.15 also show that the proposed ball-screw-based MMR shock absorber has higher efficiency when the electrical load is

small, which is suitable to harvest energy from heavy-duty vehicles with large suspension damping.

However, the mechanical efficiency of the proposed design is lower than rack-pinion one at high electrical resistances. The reason is as follows. First, the total energy-dissipating force of the shock absorber is composed of electrical damping forces and mechanical friction forces. The work only done by the electrical damping force can be converted to the electrical energy. The mechanical friction force of the proposed design is larger than that of the rack-pinion design due to additional friction force induced by the ball screw and the high-speed rotational MMR gearbox. Under high electrical resistances, the electrical damping force is small and the total energy-dissipating force is dominated by the mechanical friction force. As a result, for the proposed design, the ratio of power lost due to mechanical friction to the input power is larger than that of the rack-pinion design, resulting in a lower mechanical efficiency. However, as electrical resistances decrease, the electrical damping force contributes to the total energy-dissipating force more and more, which will make the mechanical efficiency of both designs closer. In addition, the backlash of the proposed design is smaller than the rack-pinion design, Therefore, under small electrical resistances, the proposed ball-screw design can have higher mechanical efficiency than the rack-pinion one, especially when vibration inputs are small (≤1mm cases).

4.5 Road Tests

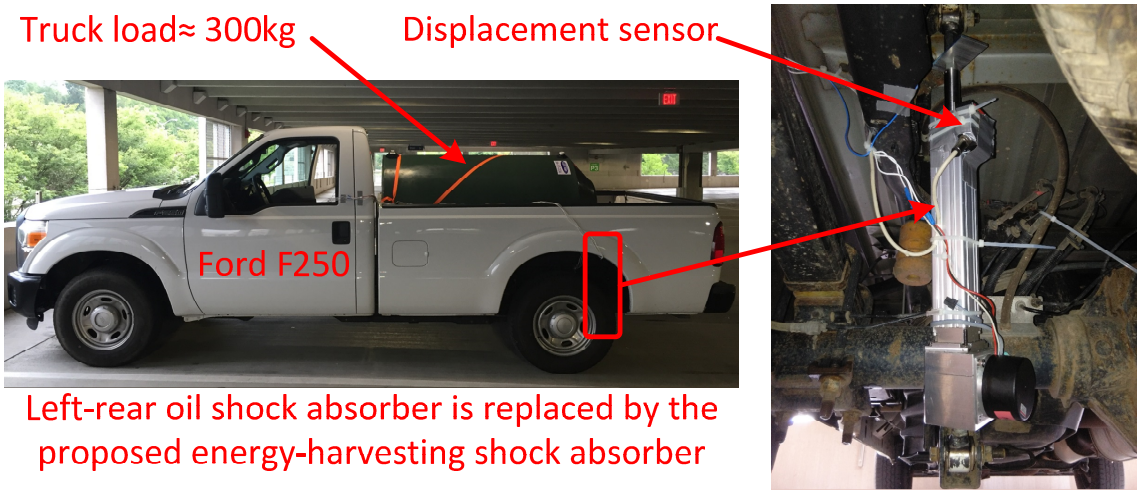

Figure 4.16 Setup of road tests. Testing vehicle (left) and mounting of the proposed shock absorber and sensors (right).

Road tests were also carried out to validate the feasibility of the proposed regenerative shock absorber in harvesting energy from vibration of vehicle suspensions. Figure 4.16 shows the test setup in which the proposed shock absorber is installed on a Ford F250 pick-up truck to replace its original left-rear oil damper. A 300kg weight was also loaded on the truck bed to emulate the actual operating situation more closely. A laser displacement sensor from Micro-Epsilon and a PCB accelerometer were used to record the relative displacements of the shock absorber and the chassis acceleration. The tests were conducted by driving the modified vehicle at 40mph on a paved road near Virginia Tech campus and passing over a speed bump at 5mph. The testing location is shown in Figure 14.17

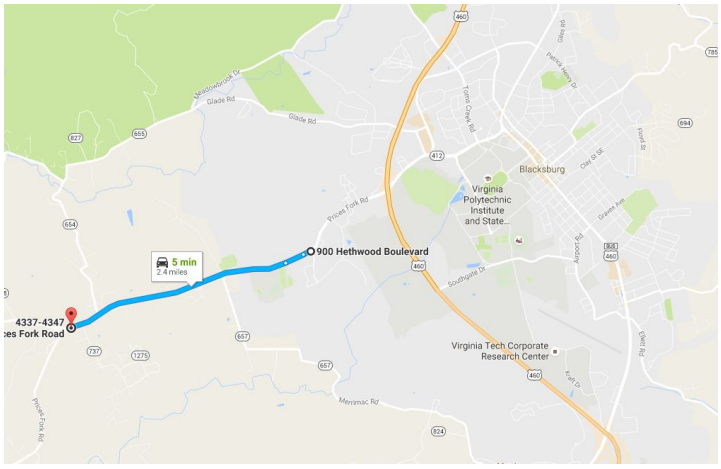

Figure 4.17 The location of road tests highlighted in blue.

The generated phase voltages, shock absorber displacements and chassis accelerations are recorded by a coco-80 dynamic signal analyzer from Crystal Instrument. Figure 4.18 (a) – (c) show the testing results of the generated voltage and corresponding displacements for different driving conditions. The results have been statistically summarized in Table 4.2.

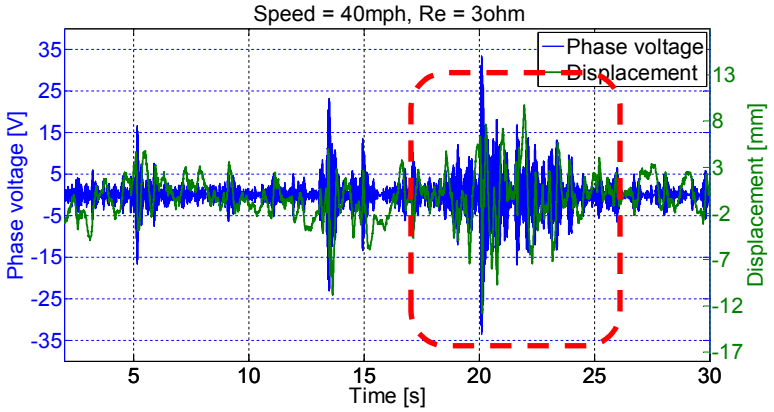

(a)

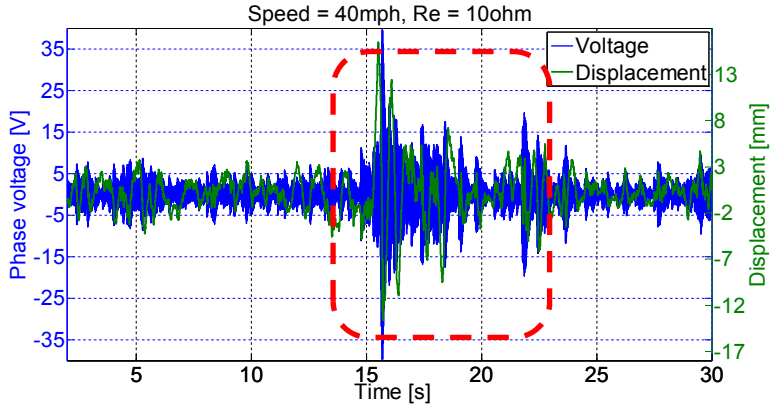

(b)

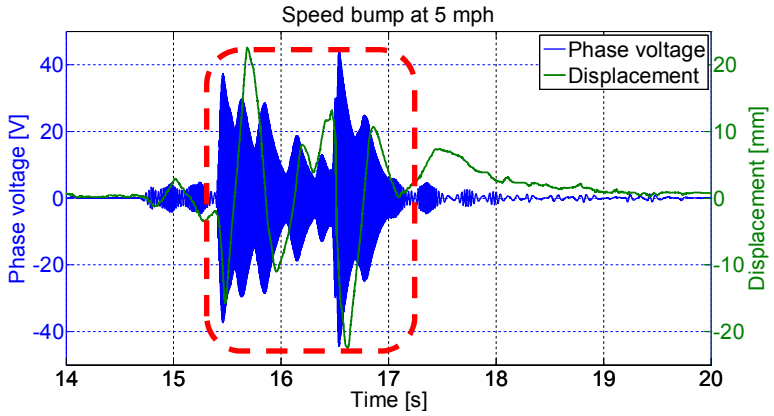

(c)

Figure 4.18 Generated phase voltage and corresponding displacements per shock absorber for different driving conditions (a) with 40mph and 3Ω electrical loads (b) with 40mph and 10Ω electrical loads (c) passing over a speed bump at 5mph and with 10Ω electrical loads.

Table 4.2 The results of road tests, per shock absorber

Driving condition	Road type	Peak phase voltage [V]	Peak phase power [W]	Ave. total power [W]	Ave. total power in red box [W]
$V = 40\text{mph}, R_e = 3\Omega$	Paved road	33.46	373	10.1	24.7
$V = 40\text{mph}, R_e = 10\Omega$	Paved road	39.57	158	5.14	13.3
$V = 5\text{mph}, R_e = 10\Omega$	Speed bump	44.42	197.3	N/A	52.65

The results in Table 4.2 show that the proposed regenerative shock absorber is feasible to continuously generate a decent amount of energy from suspension vibration when vehicles are driving on paved roads. Moreover, the proposed shock absorber is capable of surviving from large shocks caused by road obstacles and recovering the vibration energy. For our case, an average power of 52.65 W has been achieved in a 2-second period when the testing vehicle was passing over a speed bump at 5mph. Furthermore, the proposed shock absorber still works well after a 5-hours testing drive in two days, which shows it is also durable.

In addition to the energy harvesting performance, we also evaluate the chassis acceleration and jerk, commonly representing ride comfort of vehicles, for the MMR-based shock absorber in comparison with the original oil shock absorber and no shock absorber case. A low pass filter with a cutoff frequency 100Hz and stopband frequency 200Hz is used to filter out high-frequency measurement noise. The results are shown in Figure 4.19. It should be noted that the road segment may not be exactly same for these two testing results.

It is shown that the root-mean-square (RMS) values of filtered chassis acceleration of the proposed MMR-based shock absorber is 11.12% smaller than that of the original shock absorber and that the RMS values of corresponding filtered jerk is 5.83% smaller than that of the original shock absorber. The results show that the MMR-based shock absorber is able to improve the ride comfort of vehicle suspensions, as compared to conventional oil dampers. Because human is highly sensitive to the acceleration and jerk only ranging from 4Hz to 10Hz. The reason is summarized as follows. First, the proposed MMR-based shock absorber can provide an additional inertial force proportional to the suspension velocity which may lead to a better ride comfort. Second, the proposed MMR-based shock absorber has an disengaged status in which the shock absorber is separated from the primary suspension system, which may lead to a better suspension performance during second suspension resonance by reducing the impact force. To further improve

the ride comfort of the suspension with the MMR-based shock absorber, the coupled dynamics of the suspension and the proposed shock absorber will be studied and optimized in detail in the next Chapter. In addition, a semi-active control will be also proposed to control the proposed shock absorber and further improve the suspension dynamics.

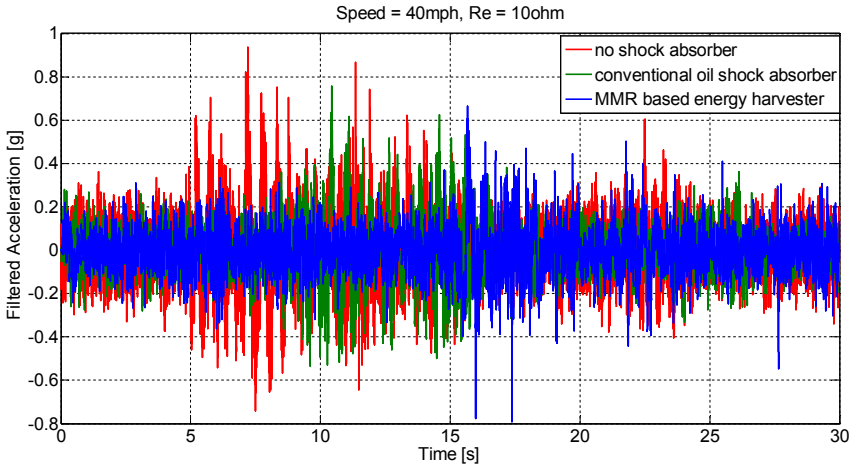

(a)

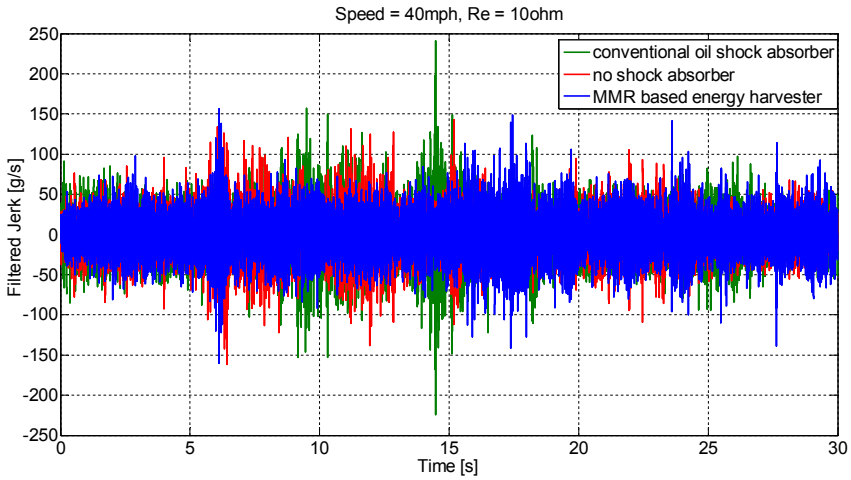

(b)

Figure 4.19 (a) Filtered chassis acceleration with the MMR-based energy harvester (RMS = 0.1079g), original oil shock absorber (RMS = 0.1214g) and no shock absorber (RMS = 0.1295g), (b) Filtered chassis jerk with the MMR-based energy harvester (RMS = 26.5g/s), original oil shock absorber (RMS = 28.05g/s) and no shock absorber (RMS = 25.54g/s). A low pass filter with cutoff frequency 100Hz and stopband frequency 200Hz is used to filter out high-frequency measurement noises.

4.6 Chapter Summary

In this paper, we propose a new-type of MMR-based energy-harvesting shock absorber using a ball-screw mechanism and bevel gears with embedded one-way clutches. Due to the one-way clutches, the proposed shock absorber is able to convert reciprocating suspension vibration into the unidirectional rotation of a generator. This function can significantly increase energy-harvesting efficiency by enabling the generator to rotate at a relatively steady speed during irregular vibrations and improve system reliability by reducing impact forces among transmission gears. In this paper, we also analyze the non-linear dynamics of the MMR mechanism induced by the engagement and disengagement of the one-way clutches. It is shown that the proposed shock absorber acts as a fixed inerter in parallel with a variable damper tuned by the external electrical loads of the generator when the system is engaged.

In addition to theoretical analysis, lab and road tests were also conducted to experimentally characterize the proposed shock absorber. In the lab tests, the performance of the proposed shock absorber is examined with various electrical loads, under harmonic excitations with various excitation frequencies and amplitudes. It was found that the equivalent damping increases from 4,425Ns/m to 15,420 Ns/m as the electrical load changes from open loop to 3Ω under harmonic excitations around the first resonant frequency of vehicle suspensions. The energy-harvesting efficiency of the proposed shock absorbers was also studied when subjected to various excitation conditions. The highest mechanical efficiency, 70.1%, is achieved under 4Hz harmonic vibration input with 3 Ω external electrical loads, corresponds to a 51.9% overall energy harvesting efficiency. Moreover, it was found that the backlash of the proposed shock absorber is much smaller than existing rack-pinion MMR energy-harvesting shock absorbers. The road tests show that the proposed regenerative shock absorber is feasible to continuously generate a decent amount of energy from suspension vibration when vehicles are driving on paved roads. Moreover, the proposed shock absorber is capable of surviving from large shocks caused by road obstacles and recovering the vibration energy.

5 Dynamics and Control of the Vehicle Suspension with a MMR-Based Regenerative Electromagnetic Shock Absorber

5.1 Motivation

In Chapter 4, we designed and experimentally characterized a novel MMR-based regenerative electromagnetic shock absorber using a ball-screw mechanism. Due to the rotational inertia of the electrical generator, commonly referred to as the inerter, an additional force proportional to the relative acceleration of the sprung mass and unsprung mass is provided by the proposed shock absorber. Some preliminary researches using inerter to improve the performance of traditional suspension in terms of ride comfort and vehicle stability have been conducted, see [46-47]. However, the inerter effect with the nonlinear dynamics caused by sprag clutches in the proposed are still needed to be explored. In addition, since the proposed shock absorber can work as a controller damper as well as an energy harvester, a novel control algorithm will also be proposed to control the proposed shock absorber considering its unique nonlinear dynamics induced by the two one-way clutches.

5.2 The Dynamics of the Vehicle Suspension with a MMR-based Regenerative Electromagnetic Shock Absorber

5.2.1 Modelling of the vehicle suspension with a MMR-based shock absorber

A 2-DOF vehicle suspension model is considered in this chapter to study the coupled dynamics of the suspension with the MMR-based shock absrober. As derived in Chapter 4, the force of the MMR-based shock absorber is

$$\begin{cases} F_e = m_e \frac{d^2x}{dt^2} + c_e \frac{dx}{dt} & \dot{\theta} = \dot{\theta}_{in}, \quad engaged\ period \\ F_d = 0 & \dot{\theta} > \dot{\theta}_{in}, \ disengaged\ period \end{cases} \tag{5.1}$$

From Equation (5.1), we can see that there are two states of the suspension system, the engaged state and the disengaged state. In the engaged state, the suspension system is a linear system, in

which the generator exerts an inerter force and damping force onto the suspension. In the disengaged state, the suspension system with MMR-based shock absorber becomes two independent linear systems. One system is an undamped suspension system. The other system are the gearbox and the generator, which are independent of the suspension and rotate with the kinetic energy stored in their inertia. The engaged state and disengaged stage of the vehicle suspension with a MMR-based regenerative electromagnetic shock absorber are shown in Figure 5.1.

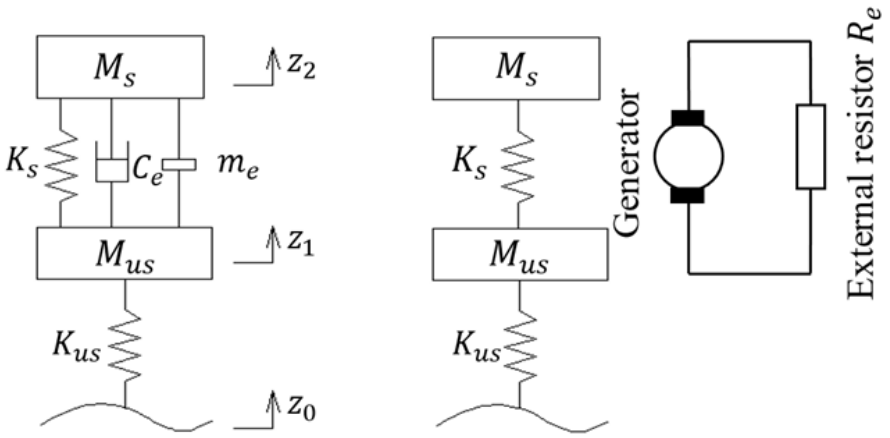

(a) (b)

Figure 5.1 2-DOF vehicle suspension with a ball-screw-based MMR regenerative electromagnetic shock absorber (a) Engaged state (b) Disengaged state

The dynamics of the suspension system with the MMR-based shock absorber are

Engaged dynamics:

$$\begin{cases} M_s\ddot{z}_2 = K_s(z_1 - z_2) + m_e(\ddot{z}_1 - \ddot{z}_2) + c_e(\dot{z}_1 - \dot{z}_2) \\ M_{us}\ddot{z}_1 = K_{us}(z_0 - z_1) - K_s(z_1 - z_2) - m_e(\ddot{z}_1 - \ddot{z}_2) - c_e(\dot{z}_1 - \dot{z}_2) \end{cases}, \quad \dot{\theta} = \dot{\theta}_{in} \tag{5.2a}$$

Disengaged dynamics:

$$\begin{cases} M_s\ddot{z}_2 = K_s(z_1 - z_2) \\ M_{us}\ddot{z}_1 = K_{us}(z_0 - z_1) - K_s(z_1 - z_2) \\ J_m\frac{d^2\theta}{dt^2} + c_m\frac{d\theta}{dt} = 0 \end{cases} \quad \dot{\theta} > \dot{\theta}_{in} \tag{5.2b}$$

where M_s is the sprung mass, M_{us} is the unsprung mass, K_s is the suspension stiffness, K_{us} is the tire stiffness, z_2, z_1, z_0 are the displacements of sprung mass, unsprung mass and road disturbance.

5.2.2 Performance index of ride comfort and road handling

The ride comfort is evaluated by the ratio of root mean square (RMS) value of the chassis acceleration to the RMS of the road disturbance,

$$a_{rms} = \sqrt{\frac{\frac{1}{N}\sum_{i=1}^{N} \ddot{z}_2(i)^2}{\frac{1}{N}\sum_{i=1}^{N} \dot{z}_0(i)^2}} \qquad i = 1,2,\cdots,N \tag{5.3}$$

Road handling is evaluated by the ratio of the dynamic tire load to the static tire load

$$\mu_{rms} = \frac{K_{us}\sqrt{\frac{1}{N}\sum_{i=1}^{N}(z_1(i)-z_0(i))^2}}{(M_s+M_{us})g} \qquad i = 1,2,\cdots,N \tag{5.5}$$

where g is the gravitational acceleration.

5.2.3 Numerical analysis of the suspension system with the MMR-based shock absorber

5.2.3.1 Road excitation and vehicle parameters

In accordance with ISO-8608, roads are classified as Class A-H [53-54]. The corresponding PSD of the road is

$$S(n) = G_0\left(\frac{n}{n_0}\right)^{-p} \tag{5.6}$$

Table 5.1 ISO8608 values of G_0 and σ_q

Road Class	A	B	C	D	E
$\boldsymbol{G_0/(10^{-6}m^3)}$ $\boldsymbol{(n_0 = 0.1m^{-1})}$	16	64	256	1024	4096
$\boldsymbol{\sigma_q/(10^{-3}m)}$	3.81	7.61	15.23	30.45	60.90

where n is spatial frequency $[m^{-1}]$, n_0 is the reference spatial frequency $[0.1\,m^{-1}]$. p is the frequency spectrum exponential, which represents the slope of the PSD curve in log-log plot and

is selected as 2 here. G_0 is the road roughness coefficient, which represents the PSD of the road at the reference wave number. Table 5.1 shows the typical values of G_0 and the RMS value of the road displacement σ_q about Class A-E road. Here we selected Class C road to conduct the simulation tests and study the influences of the system dynamics. Assuming that the vehicles are driven at a velocity of 60 mph.

Influences of the MMR-based shock absorber on suspension dynamics vary for different types of vehicles, since their damping, stiffness and curb weight are different. To illustrate these different influences, various types of vehicles are studied, including passenger cars, buses and trucks.

Suspension parameters vary largely among trucks. When an MMR-based shock absorber is installed on trucks with different suspension parameters [51-52, 55-62], the effects can be classified into two categories: for one category of trucks, MMR-based shock absorber can only improve the ride comfort, and for the other category of trucks, MMR-based shock absorber can improve both ride comfort and road handling if the equivalent inerter m_e is properly designed. Hence, we chose two typical groups of truck parameters to illustrate the different influences of MMR-based shock absorbers on trucks.

Table 5.2 shows the parameters of different vehicles [52, 59, 63, 64]. The damping ratio of a suspension is defined as $\zeta = \frac{c}{2\sqrt{K_S \cdot M_S}}$, and the stiffness ratio is $r_k = \frac{K_{us}}{K_S}$. Truck 2 is a light-damped vehicle.

Table 5.2 Vehicle parameters

	$M_s[kg]$	$M_{us}[kg]$	$K_s[kN/m]$	$K_{us}[kN/m]$	$C(kNs/m)$	ζ	r_k
Car	240	36	16	160	0.98	0.25	10
Bus	2250	250	150	800	10	0.27	5.3
Truck 1	4450	550	622.18	1705.45	26.582	0.25	2.7
Truck 2	4500	500	400	2000	10	0.12	5

5.2.3.2 Performance of inerter-based shock absorber and MMR-based shock absorber

As explained before, the engaged MMR-based shock absorber can be modeled as a traditional shock absorber in parallel with an equivalent inerter. The engaged MMR-based shock absorber is

also referred to as NonMMR shock absorber in this chapter. And MMR shock absorber can be seen as an engaged MMR-based shock absorber plus a disengaged working process. Hence, we set the damping coefficient to a constant which is the same as the conventional oil damper on the vehicles, to compare the dynamic performances of suspensions with different shock absorbers, including traditional viscous shock absorber, the NonMMR shock absorber and the MMR-based shock absorber.

Figures 5.2 – 5.3 show the ride comfort comparison and road handling comparison on various vehicles. In Figures 5.2 and 5.3, the value at the point where equivalent inertance is equal to zero represents the performance of the vehicle with traditional oil shock absorber. When the performance index of the regenerative suspension is smaller than that value at me=0, the regenerative suspension provides improved performance over the traditional shock absorber.

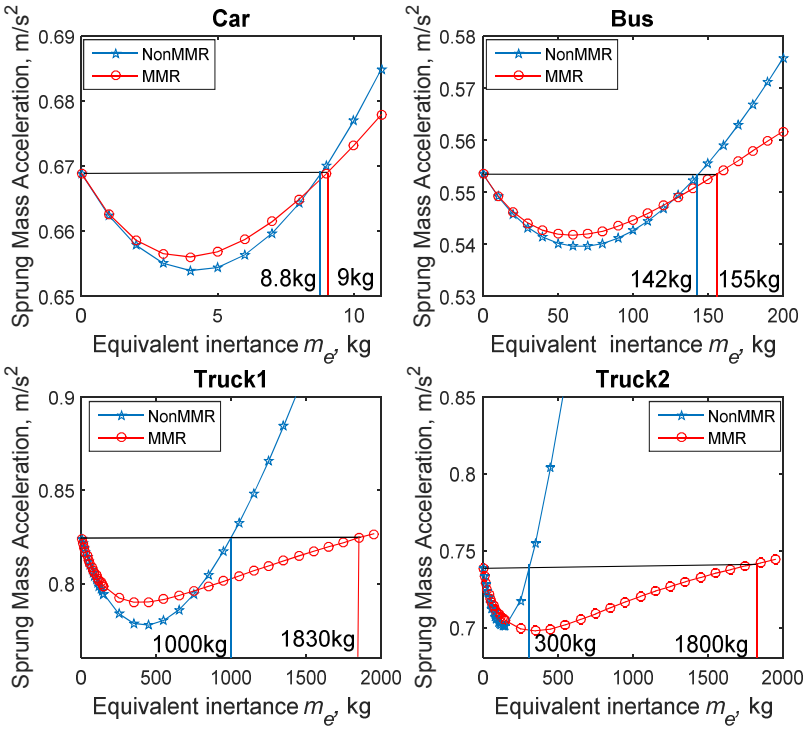

Figure 5.2 Ride comfort comparisons between suspensions with traditional shock absorber, NonMMR shock absorber and MMR-based shock absorber.

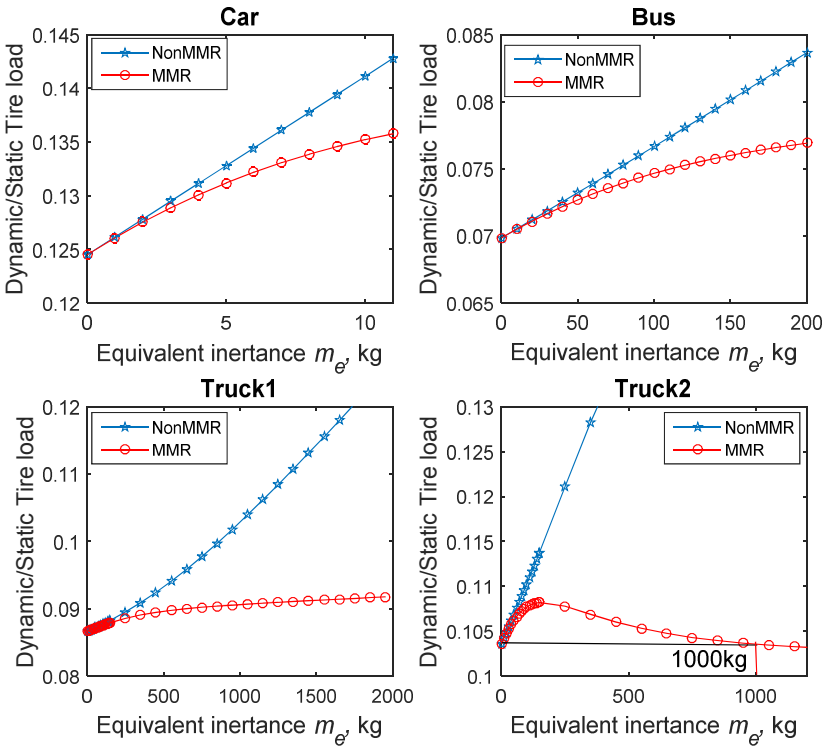

Figure 5.3 Road handling comparisons between suspensions with traditional shock absorber, NonMMR shock absorber and MMR-based shock absorber.

Figure 5.2 shows the ride comfort comparison. (1) For both NonMMR shock absorber and MMR shock absorber, there exists a certain inertance range, in which the ride comfort of the regenerative suspension is better than the corresponding traditional suspension. (2) For NonMMR shock absorber, this inertance range for ride comfort improvement increases from Car to Bus to Truck2 to Truck1, due to the increase in the vehicle gross mass and the decrease in the stiffness ratio of tire stiffness to suspension stiffness. (3) MMR shock absorber provides much larger inertance range for improvement than Non-MMR shock absorber. This phenomenon is more obvious for the cases of trucks. When the inertance in the EHSA is not a small value, commonly in a range of 10–40% of the sprung mass, MMR-based shock absorber can improve the ride comfort over the traditional shock absorber while NonMMR shock absorber cannot. Moreover, MMR shock absorber provides much better ride comfort than NonMMR ones when the inertance is larger than a certain value, like 150 kg for Truck 2.

From Figure 5.3, it can be seen that: (1) MMR shock absorber provides better road handling than NonMMR shock absorbers; (2) however, both regenerative shock absorbers deteriorate the

road handling of the normal-damped vehicles, such as Car, Bus and Truck 1; (3) MMR improves the road handling of the light-damped vehicle, like Truck 2, when the inertance is larger than a certain value, like 1000 kg for Truck 2.

As shown in Figures 5.2–5.3, MMR shock absorber is more suitable to vehicles than NonMMR shock absorbers. Additionally, with a properly designed inerter, MMR shock absorber is able to improve both the ride comfort and road handling simultaneously over the traditional shock absorber, when it is installed on light-damped, heavy-duty vehicles. For example, the proper inertance range for Truck 2 is 1000–1800 kg.

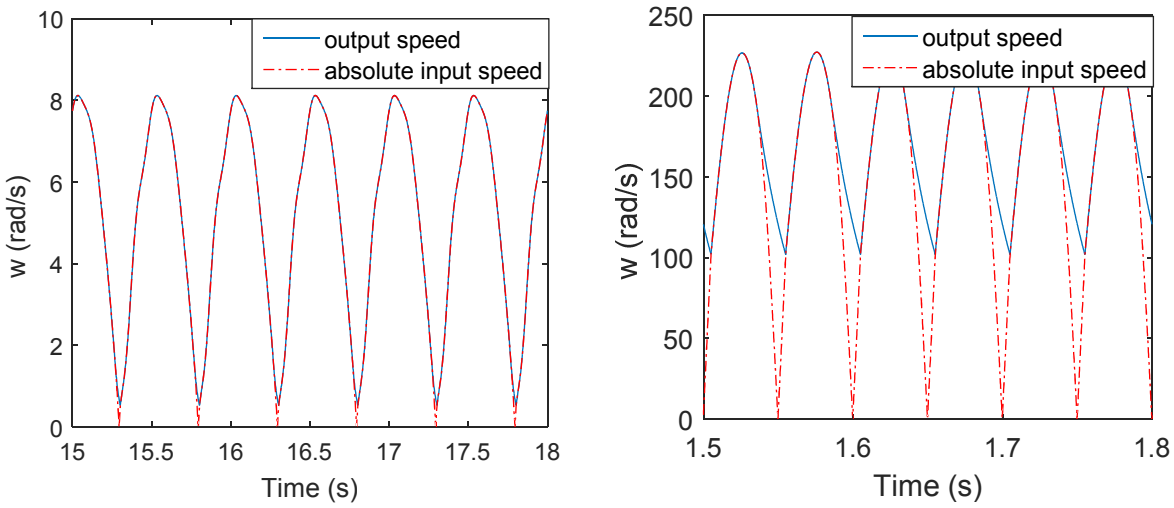

(a) (b)

Figure 5.4 Time response of MMR-based suspension under sinusoid excitations with different excitation frequencies : (a) 1Hz, (b) 10Hz

As mentioned before, MMR shock absorber can be seen as a NonMMR shock absorber plus a disengaged working process. The disengagement happens when the output rotational speed is larger than the input rotational speed. Figure 5.4 shows the time responses of the input velocity and the output velocity of the motion rectifier, under sinusoid excitations of different frequencies. We can see that when the excitation frequency is higher, the motor shaft is disengaged from the system for a longer period, and the disengaged ratio becomes larger, which is consistent with the experimental results in Chapter 4. When the MMR mechanism is disengaged, the large inerter force cannot be transferred to the car body or the wheel. We have concluded that the large inerter

force at high frequencies induces unfavorable performances. Hence, MMR shock absorber performs better than NonMMR shock absorber.

5.2.4 Optimization for ride comfort and road handling

There are two main design parameters in MMR-based suspension system, equivalent inertance $m_e$and equivalent damping coefficient c_e. The equivalent inertance can be varied by changing the gear ratio in the MMR shock absorber system and the equivalent damping coefficient can be varied by changing the external resistance in the energy-harvesting circuit, as described in Equation (4.16). The ride comfort can be optimized by properly designing the equivalent inertance and equivalent damping. In this section, we optimize the equivalent inertance m_e and equivalent damping coefficient c_e in MMR-based shock absorber to achieve optimal ride comfort first. Then, the overall suspension dynamic performance is optimized, considering the tradeoff between the ride comfort and road handling.

As presented previously, MMR shock absorber is more applicable to heavy-duty vehicles, like trucks. Hence, we selected a reference truck to optimize the ride comfort performance by optimizing the equivalent inertance and damping ratio. The fixed parameters of the vehicle model are cited from those of Truck 2 in Table 5.2: M_s = 4500 kg, M_{us}= 500 kg, K_{us}= 2000 kN/m.

The trucks' stiffness ratio r_k of tire stiffness to suspension stiffness varies from 1.14 to 5, and the damping ratio ζ varies from 0.05 to 0.34 in [51-64]. However, we optimized MMR-based regenerative suspension in a stiffness ratio range of 1 to 10, to present a more comprehensive understanding of the dynamics in a wider stiffness ratio range. The optimal ride comfort provided by MMR-based regenerative suspension can be calculated using each stiffness ratio, and comparing this with the ride comfort of traditional vehicles shows the scale of improvement. Traditional vehicles' ride comfort is calculated using different damping ratios, and the comparison is shown in Figure 5.5. The optimal ride comfort of MMR-based suspension is denoted as $\ddot{z}_2$. The ride comfort of the traditional vehicle is denoted as $\ddot{z}_{2r}$.

Figure 5.5(a) shows the optimal damping ratio and optimal equivalent inertance of MMR shock absorber achieving optimal ride comfort under various stiffness ratios. When the stiffness ratio is small, both the parameters are better to be designed as large values. When the stiffness ratio gets

larger, both the parameters should be designed as small values. Figure 5.5(b) shows the improvement provided by the optimal MMR-based suspension. For example, when the damping ratio is 0.11 and stiffness ratio is 5, the improvement of the MMR-based suspension over the traditional vehicle is 13%. Additionally, the improvement becomes the largest when the damping ratio and stiffness ratio of the traditional vehicle are both small.

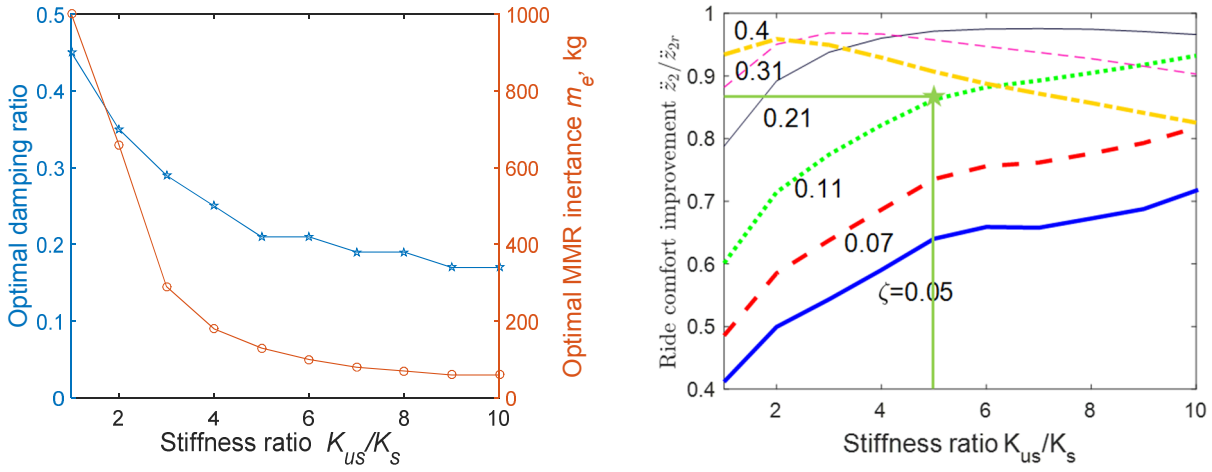

(a) (b)

Figure 5.5 Optimal parameters of MMR shock absorber for ride comfort when installed on vehicles with various stiffness ratio; (b) Ride comfort improvement of MMR-based suspension over traditional vehicle with different damping ratio ζ

As shown in Figure 5.5, optimal road handling and optimal ride comfort performance cannot be achieved simultaneously with one set of the design parameters m_e and c_e. Considering the trade-off between ride comfort and road handling, this multi-objective mixed performance optimization problem is solved by calculating the Pareto-optimal solutions [64]. Some advanced optimization methods are proposed to obtain the Pareto solutions, like NSGA-II [65].

The results are shown in Figure 5.6, which is in the non-dimensional form. The y-axis represents the MMR-based suspension's sprung mass acceleration ($\ddot{z}_2$) over the traditional vehicle sprung mass acceleration ($\ddot{z}_{2r}$), and the x-axis represents the relative dynamic/static tyre load (μ/μ_r). Obviously, the curve at the lower left corner in Figure 5.6(a) represents the best trade-off between ride comfort and road handling, which is also the Pareto-optimal set in Figure 5.6(b).

According to Figure 5.6(b), MMR-based shock absorber can greatly improve the ride comfort and road handling performances by properly designing the equivalent damping and equivalent inertance. The greatest improvements for ride comfort and road handling appear on point B and point A, and the values are, respectively, 12.2% and 19.5%. Since the ride comfort and road handling are in conflict, a weight $\delta\epsilon(0,1)$ is always introduced when the suspension is designed, as shown in Figure 5.6(b). The choice of the weight can be based on the road roughness, normally a smaller δ for worse roads and a larger δ for good roads [65]. The relevant road profile estimation can be found in [65-66]. Therefore, as the Pareto-solution set and the corresponding parameters are both obtained, it is very convenient to design an MMR-based regenerative suspension for different weights, as shown in Figure 5.6(b).

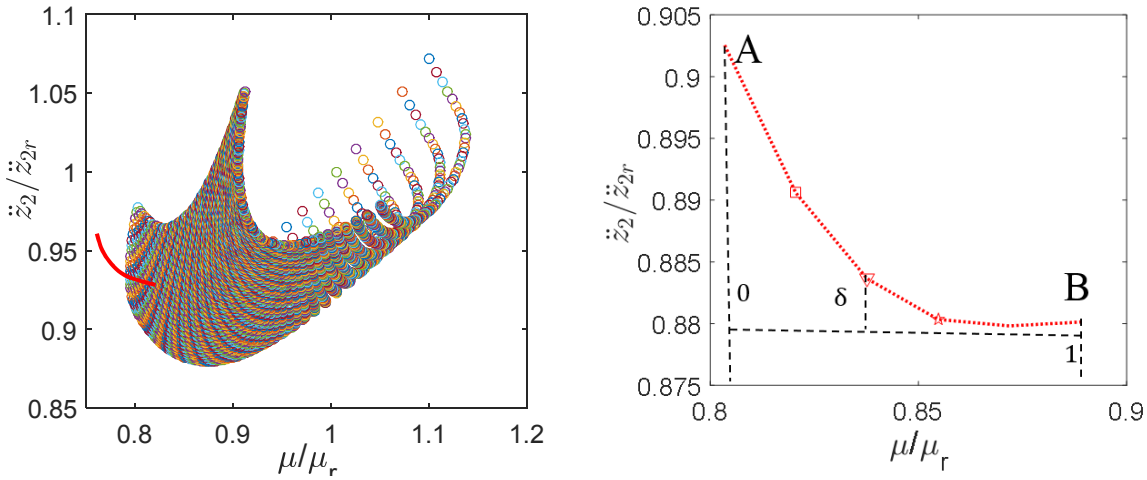

(a) (b)

Figure 5.6 (a) Performance indices under various parameters; (b) Pareto-optimal sets for the ride comfort ($\ddot{z}_2$) – road handling (μ) problem

5.3 A Novel Force-Tracking Control for the Vehicle Suspension with a MMR-Based Regenerative Electromagnetic Shock Absorber

5.3.1 A suboptimal semi-active control method for the engaged system

When the system is in the engaged stage, the force of the shock absorber is $F_e = m_e \frac{d^2x}{dt^2} + c_e \frac{dx}{dt}$, where m_e is the fixed equivalent inertance caused by the rotational inertia of the generator. c_e is the adjustable damping tuned by the external load. Then, the control problem in the engaged stage become a linear suspension damping control problem subject to a semi-active damping constraint. Then, a new control algorithm in a similar sense of clipped-optimal control can be employed to control the system during the engaged period.

The control model can be formed into linear state space by setting the damping force $c_e(\dot{z}_1 - \dot{z}_2)$ in Equation (5.2) as the control input u. The dynamics of the engaged system in Equation (5.2a) can be written as,

$$\dot{x} = A_e x + B_{eu} u + B_{ew} w \tag{5.7}$$

where $= [x_1, x_2, x_3, x_4]' \in R^4$, $x_1 = z_2 - z_1$ is the suspension deflection, $x_2 = \dot{z_2}$ is the sprung mass velocity, $x_3 = z_1 - z_0$ is the tire deflection, $x_4 = \dot{z_1}$ is the unsprung mass velocity, w is the velocity excitation $\dot{z_0}$, and

$$A_e = M^{-1}K, \qquad B_{eu} = M^{-1}H, \qquad B_{ew} = M^{-1}G$$

$$M = \begin{bmatrix} 1 & 0 & 0 & 0 \\ 0 & M_s + m_e & 0 & -m_e \\ 0 & 0 & 1 & 0 \\ 0 & -m_e & 0 & M_{us} + m_e \end{bmatrix}, \qquad K = \begin{bmatrix} 0 & 1 & 0 & -1 \\ -K_s & 0 & 0 & 0 \\ 0 & 0 & 0 & 1 \\ K_s & 0 & -K_{us} & 0 \end{bmatrix}$$

$$\mathrm{H} = [0, -1, 0, 1]^T, \qquad G = [0, 0, -1, 0]^T$$

The controlled output y_e of the engaged system involving the sprung mass acceleration, suspension deflection, and tire deflection is defined as

$$\mathrm{y}_e = [\ddot{z}_2 \quad (z_2 - z_1) \quad (z_1 - z_0)] = C_e x + D_e u \tag{5.8}$$

where

$$C_e = \begin{bmatrix} A_e(2,:) \\ 1 \quad 0 \quad 0 \quad 0 \\ 0 \quad 0 \quad 1 \quad 0 \end{bmatrix}, \qquad D_e = \begin{bmatrix} B_{eu}(2,:) \\ 0 \\ 0 \end{bmatrix}$$

and $A_e(2,:)$ and $B_{eu}(2,:)$ denote the second row of A_e and B_{eu}, respectively.

To deal with these three performance requirements, a quadratic performance index is defined as

$$\mathrm{J} = \lim_{T\to\infty} \int_0^T \mathrm{y}_e{}^T \Lambda \mathrm{y}_e \, dt \tag{5.9}$$

where Λ contains the weights among sprung mass acceleration, suspension deflection, and tire deflection. The performance index (5.9) can be rewritten as

$$\mathrm{J} = \lim_{T\to\infty} \int_0^T x^T Q x + 2x^T N u + u^T R u \, dt \tag{5.10}$$

where $Q = C_e{}^T \Lambda C_e$, $N = C_e{}^T \Lambda D_e$ and $R = D_e{}^T \Lambda D_e$.

If ignoring the constraint on the semi-active damping of the engaged system, the aforementioned problem is a linear quadrative regulation problem and an optimal control can be derived as [67]

$$u^* = -R^{-1}\left(B_{eu}{}^T P + N^T\right)x \tag{5.11}$$

where P is the solution of the following algebraic Riccati eauation(ARE)

$$A_e P + P A_e - (P B_{eu} + N) R^{-1} (P B_{eu} + N)^T + Q = 0 \tag{5.12}$$

As shown in [11], the optimal solution for a semi-active damping force involves time-varying Riccati equations and no analytical solution can be obtained. However, suboptimal control law, the clipped optimal method, is a good approximate solution in practice. There, when the suspension system with the MMR-based shock absorber is engaged, a new clipped optimal control law considering the inertance of the generator is given by

$$u = \begin{cases} u_{min}, & u^* < u_{min} \\ u^*, & else \\ u_{min}, & u^* > u_{max} \end{cases} \tag{5.13}$$

where $u_{min} = c_{min}|\dot{z}_2 - \dot{z}_1|$ and $u_{max} = c_{max}|\dot{z}_2 - \dot{z}_1|$, c_{min} and c_{max} are the minimum and maximum equivalent damping coefficients of the proposed shock absorber, as have been experimentally characterized in Figure 4.12.

5.3.2 A passive control method for the disengaged system

As introduced before, when the system is in the disengaged stage, the force of the shock absorber is zero $F_d = 0$. Hence, we connect an constant external resistor to the generator of the proposed shock absorber. The dynamics of the disengaged system in Equation (5.2b) can be written as,

$$\dot{x} = A_d x + B_d w \tag{5.14}$$

where

$$\mathrm{A_d} = \begin{bmatrix} 0 & 1 & 0 & -1 \\ -\frac{\mathrm{K_s}}{\mathrm{M_s}} & 0 & 0 & 0 \\ 0 & 0 & 0 & 1 \\ \frac{\mathrm{K_s}}{\mathrm{M_{us}}} & 0 & -\frac{\mathrm{K_{us}}}{\mathrm{M_{us}}} & 0 \end{bmatrix}, \qquad \mathrm{B_d} = \begin{bmatrix} 0 \\ 0 \\ -1 \\ 0 \end{bmatrix}$$

The controlled output y_d of the disengaged system involving the sprung mass acceleration, suspension deflection, and tire deflection is defined as

$$y_d = [\ddot{z}_2 \quad (z_2 - z_1) \quad (z_1 - z_0)] = C_d x + D_d w \tag{5.15}$$

where

$$C_d = \begin{bmatrix} A_d(2,:) \\ 1 & 0 & 0 & 0 \\ 0 & 0 & 1 & 0 \end{bmatrix}, \qquad D_d = \begin{bmatrix} B_d(2,:) \\ 0 \\ 0 \end{bmatrix}$$

and $A_d(2,:)$ and $B_d(2,:)$ denote the second row of A_d and B_d, respectively.

Therefore, a new control strategy named Force-Tracking combining the control methods in both engaged period and disengaged period of the system is proposed.

5.4 Numerical Analysis of the Proposed Force-Tracking Control

This section numerically analyzes the suspension performance when the proposed control algorithm is applied to control the proposed shock absorber on the vehicle suspension system. In addition, this section compares the controlled performance to the uncontrolled performance to verify the effectiveness of the proposed control algorithm.

Figure 5.7 shows the frequency response comparisons among traditional shock absorber, nonMMR shock absorber, MMR-based shock absorber and MMR-based shock absorber controlled by the force tracking semi-active damping control strategy. The simulation parameters are based on the parameters of Truck 2 summarized in Table 5.2 with additional equivalent inertance 250kg for nonMMR and MMR-based shock absorber. The minimum damping and maximum damping of the semi-active MMR-based shock absorber are set to be 30 kNs/m and 2 kNs/m. The weighting matrix Λ in the performance index (5.9) is set to balance the ride comfort and road handling performance of MMR-based vehicle suspensions, which is

$$C_d = \begin{bmatrix} 1 & 0 & 0 \\ 0 & 11000 & 0 \\ 0 & 0 & 1000 \end{bmatrix}$$

The results in Figure 5.7(a) show that the MMR-based shock absorber is more effective in reducing the second resonant peak of the chassis acceleration in frequency domain, as compared to NonMMR shock absorber. In addition, the passive MMR and nonMMR shock absorbers both increase the second resonant peak compared to the conventional oil damper.

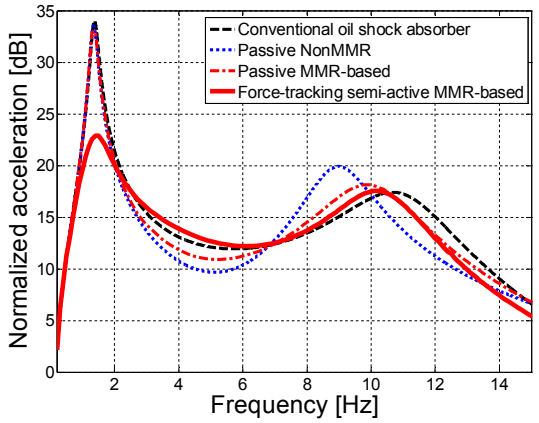

(a)

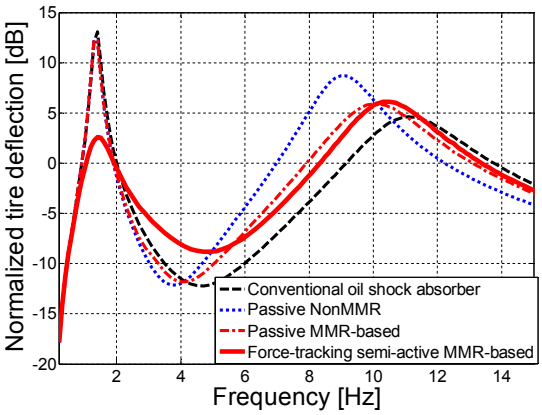

(b)

Figure 5.7 Frequency response comparisons among traditional shock absorber, nonMMR shock absorber, MMR-based shock absorber and MMR-based shock absorber controlled by force tracking control strategy. The equivalent inertance is 250kg for nonMMR and MMR shock absorbers.

However, by using the proposed MMR-based shock absorber in which the damping coefficient is adjustable, we can apply a semi-active control method to it to improve the suspension performance

especially for ride comfort and road handling. Shown in Figure 5.7(a), the semi-active MMR shock absorber significantly reduces the first resonant peak of chassis acceleration. This also proves the effectiveness of the proposed force tracking semi-active control method for the proposed MMR-based shock absorber. Since ride comfort and road handling are two trade-offs of the suspension performance, the semi-active MMR-based shock absorber also results in a slightly deteriorated road handling performance, as shown in Figure 5.7(b).

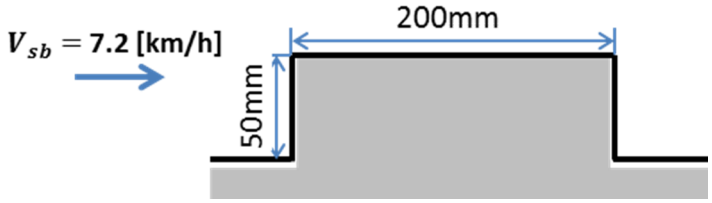

Figure 5.8 Speed bump dimensions

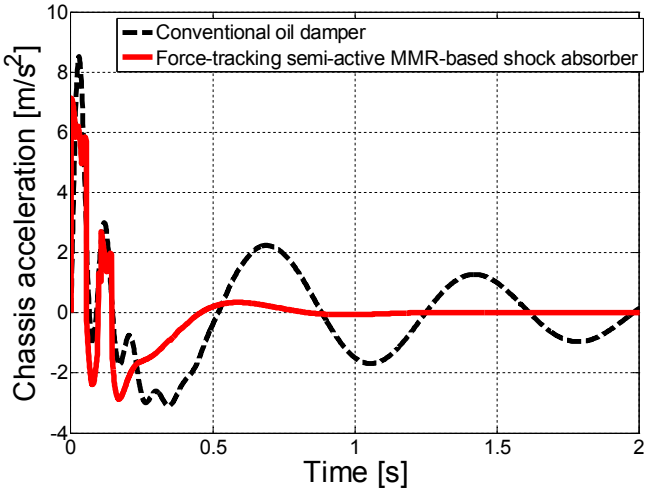

Figure 5.9 Speed bump response for the MMR-based shock absorber

The real road disturbances experienced by vehicle suspension systems include road obstacles and regular unevenness. A vehicle passing over a speed bump 0.05m high and 0.2m wide at 7.2 km/h (4.5 mph) was taken as a bump test to study the characteristics of the MMR-based shock absorber in time domain. The dimensions of the speed bump are depicted in Figure 5.8. The speed bump responses for different type of shock absorbers are shown in Figure 5.9. Figure 5.9 shows that the semi-active MMR-based shock absorber can significantly reduce the sprung mass

acceleration compared to the conventional oil damping in suspension systems. This conclusion agrees with the conclusion from Figure 5.7.

5.5 Using SH-PDD as Tracking Target in the engaged MMR-based suspensions

The tracking target of the force-tracking control proposed in Section 5.4 is essentially a semi-active control method. Therefore, this section replace the tracking target of the force-tracking control with the SH-PDD proposed in Chapter 2. Figure 5.10 shows the frequency response comparisons among traditional shock absorber, nonMMR shock absorber, MMR-based shock absorber and MMR-based shock absorber controlled by the force tracking semi-active damping control strategy and the SH-PDD.

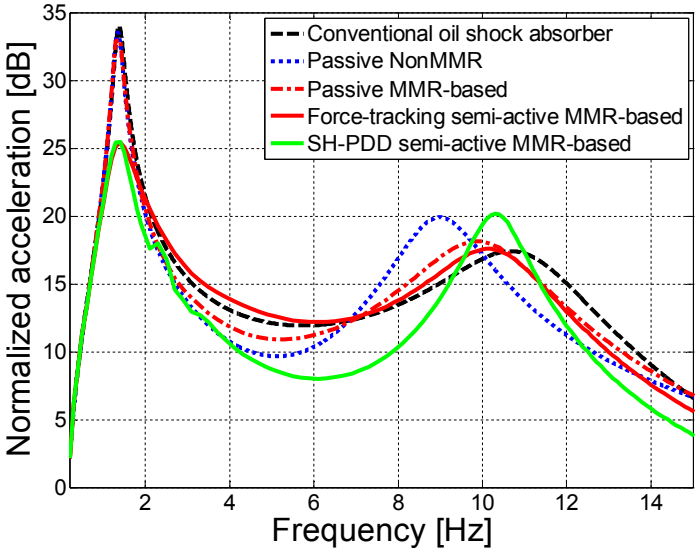

Figure 5.10 Frequency response comparisons among traditional shock absorber, nonMMR shock absorber, MMR-based shock absorber and MMR-based shock absorber controlled by force tracking control strategy and the SH-PDD. The equivalent inertance is 250kg for nonMMR and MMR shock absorbers.

The results in Figure 5.10 show that the MMR-based shock absorber controlled by SH-PDD significantly reduces the chassis acceleration between the first and second chassis resonance. However, as compared to Force-tracking control, SH-PDD slightly increases the second resonant

peak, which may deteriorate ride comfort during high-frequency suspension vibrations. The overall performance in Figure 5.10 proves the effectiveness of the proposed SH-PDD semi-active control method for the proposed MMR-based shock absorber.

5.6 Chapter Summary

This chapter studies the influences of the proposed MMR-based shock absorber on suspension performances and the optimization of the parameters of the MMR-based shock absorbers. The MMR-based shock absorber can improve vehicle ride comfort over the traditional shock absorber if the equivalent inertance is properly designed. The MMR-based shock absorber can provide a larger inertance range for ride comfort improvement. When the MMR-based shock absorber is installed on a light-damped, heavy vehicle, both ride comfort and road handling can be improved simultaneously, if the equivalent inertance is properly designed. For example, in the above Truck 2 case, the inertance should be in the range of 0-1800kg, to obtain better ride comfort and road handling than the traditional shock absorber. This range becomes wider when the suspension spring becomes stiffer.

A new control algorithm is proposed to control the proposed shock absorber considering its unique dynamics. The results show that the controlled proposed shock absorber can potentially improve ride comfort compared to conventional oil dampers.

6 Computation-efficient Framework for the Integrated Design of Vibration Systems

6.1 Chapter Introduction

This chapter proposes a new integrated design method to simultaneously optimize the coupled structural parameters and controllers of mechanical systems by combining decentralized control techniques and Riccati-based control theories. The proposed integrated design method aims at minimizing the closed-loop H_2 norm from the disturbance to the system cost. The integrated design problems have been formulated in the cases of full state feedback controllers and full order output feedback controllers. We extend the current LTI control system to a more general framework suitable for the needs of integrated design, where the structural design is treated as a passive control optimization tackled by decentralized control techniques with static output feedback, while the active controller is optimized by solving modified Riccati equations. By using this dual-loop control system framework, the original integrated design problem is transferred to a constrained structural design problem with some additional Riccati-equation based constraints simultaneously integrating the controller synthesis. This reduces the independent design variables from the structural design parameters and the parameters of the controller to the structural design parameters only. As a result, the optimization efficiency is significantly improved. Then the constrained structural design problem is reformed as an unconstrained optimization problem by introducing Lagrange multipliers and a Lagrange function. The corresponding optimal conditions for the integrated design are also derived, which can be efficiently solved by gradient-based optimization algorithms. Later, the design examples, an active-passive vehicle suspension system, are presented. This method can be applied to the integrated design of the vehicle suspension system with the controllable regenerative shock absorbers to achieve enhanced vibration mitigation performances. More generally, this method can also be utilized to design general linear vibration systems equipped with controllers, which improves the scientific value of this dissertation.

6.2 The Integrated Structure and State-feedback Controller (ISSC) Design Problem

6.2.1 Problem formulation

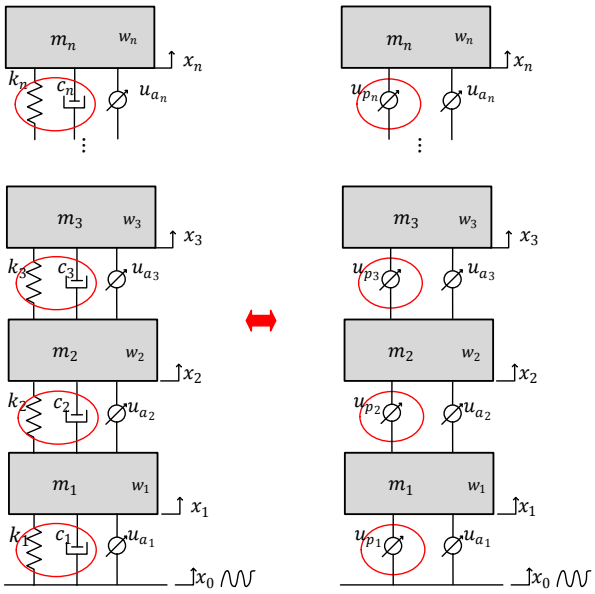

Figure 6.1. (a)A typical linear mechanical system; (b) its integrated design configuration.

Figure 6.1(a) shows a typical linear mechanical system with active controllers in which both the passive elements, including springs and dampers, and the active controllers are to be designed. Generally, the mass elements are predetermined with some other specifications like material, size, cost and others, so we consider them as the fixed parameters in the system in this chapter. In order to simultaneously design the passive elements and the active controllers in Figure 6.1(a), we reconfigure the system in Figure 6.1(b), where the reaction forces generated by the passive elements to be designed are replaced by the passive control forces u_p. Therefore, we cast the original mechanical system into an extended LTI frame by using its equivalent configuration shown in Figure 6.1(b).

$$\begin{cases} \dot{x} = Ax + B_1 w + B_2 u_p + B_3 u_a \\ z = C_1 x + D_{11} w + D_{12} u_p + D_{13} u_a \\ y_p = C_2 x + D_{21} w \end{cases} \tag{6.1}$$

where $x = [x_1, \dot{x_1}, \cdots, x_n, \dot{x_n}]' \in \mathbb{R}^{2n}$is the state vector ([]′denotes the transpose of the vector or

matrix), $w = [x_0, w_1, w_2 \cdots, w_n]' \in \mathbb{R}^{n+1}$ is the external disturbance, $u_p = [u_{p_1}, u_{p_2}, \cdots, u_{p_n}]' \in \mathbb{R}^n$ is the reaction forces provided by the passive elements to be optimized, $u_a = [u_{a_1}, u_{a_2}, \cdots, u_{a_n}]' \in \mathbb{R}^n$ is the control forces of the active controllers, $z \in \mathbb{R}^{n_z}$ is the system output cost. The 'virtual' output measurement y_p represents the feedback vectors of the passive elements to be designed. For instance, when installed between two connecting terminals of a mechanical system, springs produce force feedbacks proportional to the relative displacements of these terminals using stiffness coefficients, and dampers produce force feedbacks to the relative velocities using damping coefficients. Based on the geometry of mechanical systems, we can write y_p as a linear combination of the states and inputs [68]. It should be noted that y_p is a 'virtual' measurement which is not measured and is only used for designing the passive elements. In the case shown in Figure 6.1(b), y_p can be written as

$$y_p = [x_1 - x_0, \dot{x}_1 - \dot{x}_0, x_2 - x_1, \dot{x}_2 - \dot{x}_1, \cdots, x_n - x_{n-1}, \dot{x}_n - \dot{x}_{n-1}]' \tag{6.2}$$

Therefore, u_p can be expressed as

$$u_p = F_p y_p \tag{6.3}$$

where the passive feedback gain F_p is a decentralized block-diagonal matrix composed of the structural design parameters. A common form of F_p consisting the spring stiffness and the damping is

$$F_p = \begin{bmatrix} k_1 & c_1 & & & & & \\ & & k_2 & c_2 & \cdots & & \\ & & & & & k_n & c_n \end{bmatrix} \tag{6.4}$$

Once the block-diagonal gain F_p is obtained, the structural design parameters are determined. In contrast to the 'virtual' measurement y_p, the full states x are actually measured to construct the state-feedback controller as

$$u_a = F_a x \tag{6.5}$$

where the state-feedback control gain F_a is to be designed.

Therefore, the integrated structure and state-feedback controller (ISSC) design problem can be formed as minimizing the performance objective by designing the passive feedback gain, F_p, and the state-feedback control gain, F_a, subject to the system dynamics, as stated below

$$\begin{cases} min & J(F_p, F_a) \\ s.t. & (1), (3), (5) \\ & (F_p, F_a) \in (S_p, S_a) \end{cases} \tag{6.6}$$

where $J(F_p, F_a)$ is the performance objective, which is a function of F_p and F_a. S_p is the feasible domain of F_p, which is a set of matrices whose structure is prescribed by (6.4). S_a is the feasible domain of F_a, which is a set of matrices with the appropriate dimensions of the state-feedback control gain F_a. (S_p, S_a) consists of the search space of the optimal solution (F_p, F_a). The ISSC design problem (6.6) is depicted by the dual-loop block diagram shown in Figure 6.2.

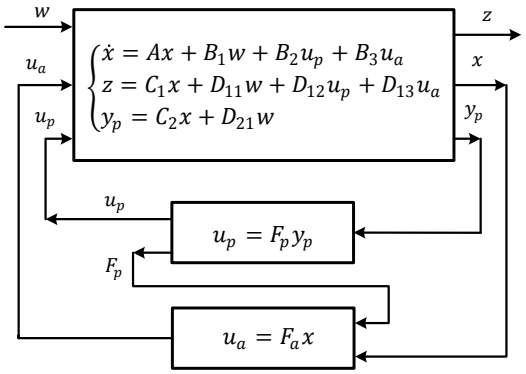

Figure 6.2. Dual-loop block diagram of the integrated structure and state-feedback controller.

6.2.2 The ISSC design problem with H_2 performance criteria

In this chapter, the performance objective $J(F_p, F_a)$ in (6.6) is particularly defined as the H_2 norm of the closed-loop system and aims to be minimized by designing F_p and F_a. Before deriving the optimal solution for the ISSC design problem with H_2 performance criteria, let us review conventional state-feedback control problems first. For a causal LTI system

$$\begin{cases} \dot{\tilde{x}} = \tilde{A}\tilde{x} + \tilde{B}_w\tilde{w} + \tilde{B}_u\tilde{u} \\ \tilde{z} = \tilde{C}\tilde{x} + \tilde{D}_u\tilde{u} \end{cases} \tag{6.7}$$

with a state-feedback controller

$$\tilde{u} = \tilde{F}\tilde{x} \tag{6.8}$$

the system H_2 norm is the L_2 norm of the system's impulse response, or the asymptotic value of the system's cost $\tilde{z}$ variance with unit white noise input $\tilde{w}$ [34].

$$min\ \ J(\tilde{F}) \triangleq \|H_{\tilde{z}\tilde{w}}\|_2^2 = \frac{1}{2\pi}\int_{-\infty}^{\infty} trace[H'_{\tilde{z}\tilde{w}}(j\omega)H_{\tilde{z}\tilde{w}}(j\omega)]d\omega = \int_0^{\infty} trace[h'_{\tilde{z}\tilde{w}}(t)h_{\tilde{z}\tilde{w}}(t)]dt \tag{6.9}$$

A classic Riccati-equation-based theorem (Theorem 1) has been developed to design the H_2 state-feedback control gain $\tilde{F}$ for the system in (6.7), which can be found in Appendix B [34].

With a structured passive controller $u_p = F_p y_p$, the integrated design model in (6.1) can be reformed as

$$\begin{cases} \dot{x} = (A + B_2F_pC_2)x + (B_1 + B_2F_pD_{21})w + B_3u_a \\ z = (C_1 + D_{12}F_dC_2)x + (D_{11} + D_{12}F_pD_{21})w + D_{13}u_a \end{cases} \tag{6.10}$$

To obtain a finite H_2 norm of the system in (6.1), D_{11} has to be zero, which is true for most mechanical systems. Furthermore, y_p is a 'virtual' measurement, therefore the sensing noise term D_{21} can be taken as zero. Thus, applying Theorem 1 to the system in (6.10), the H_2 norm of the system is minimized to

$$min\ \ \|H_{zw}\|_2^2 = trace({B_1}'XB_1) \tag{6.11}$$

with the state-feedback gain

$$F_a(F_p) = -{R_1}^{-1}({B_3}'X + {D_{13}}'(C_1 + D_{12}F_pC_2)) \tag{6.12}$$

where $R_1 = {D_{13}}'D_{13}$ and the symmetric matrix X is subjected to the modified algebraic Riccati equation below

$$\begin{aligned}&\left(A + B_2F_pC_2 - B_3{R_1}^{-1}{D_{13}}'\left(C_1 + D_{12}F_pC_2\right)\right)' X + X\left(A + B_2F_pC_2 - B_3{R_1}^{-1}{D_{13}}'\left(C_1 + \right.\right.\\ &\left.\left.D_{12}F_pC_2\right)\right) - XB_3{R_1}^{-1}{B_3}'X \ + (C_1 + D_{12}F_pC_2)'\left(I - D_{13}{R_1}^{-1}{D_{13}}'\right)(C_1 + D_{12}F_pC_2) = 0\end{aligned} \tag{6.13}$$

From equation (6.12), it is easy to see that the state-feedback control gain F_a is a function of the passive feedback gain F_p. Therefore, the original ISSC design problem in (6.6) with H_2 criteria is equivalent to a constrained structural optimization problem with an additional Riccati-equation based constraint (6.13) simultaneously integrating the controller synthesis, as stated below

$$\begin{cases} min & J(F_p) \triangleq trace({B_1}'XB_1) \\ s.t. & (13)\ and\ F_p \in S_p \end{cases} \tag{6.14}$$

It is worth noting that the reformed ISSC design problem in (6.14) only needs to search through the optimal passive feedback gain F_p with an additional constraint (6.13). This reduces the independent design variables from F_p and F_a to F_p only, therefore significantly improving the optimization efficiency. It should also be noted that the reformed ISSC design problem in (6.14) falls into a modified static output-feedback optimization problem which can be solved by defining a Lagrange function to transfer it from a constrained optimization problem to an unconstrained one. The Lagrange function is defined as

$$\begin{aligned}&\mathcal{L}(F_p, X, P) = trace({B_1}'XB_1) + trace\{[\left(A + B_2F_pC_2 - B_3{R_1}^{-1}{D_{13}}'(C_1 + D_{12}F_pC_2)\right)'X + \\ &X\left(A + B_2F_pC_2 - B_3{R_1}^{-1}{D_{13}}'(C_1 + D_{12}F_pC_2)\right) - XB_3{R_1}^{-1}{B_3}'X \ + (C_1 + D_{12}F_pC_2)'\left(I - \right.\\ &\left.D_{13}{R_1}^{-1}{D_{13}}'\right)(C_1 + D_{12}F_pC_2)]P\}\end{aligned} \tag{6.15}$$

where P is the Lagrange multiplier in a symmetric matrix form. F_p, X, P are the matrix variables to be determined. Then, using matrix calculus, the closed-form gradients of $\mathcal{L}$ can be obtained as

$$\partial\mathcal{L}/\partial F_p = 2(B_2{}'X - D_{12}{}'D_{13}R_1{}^{-1}B_3{}'X + D_{12}{}'\big(I - D_{13}R_1{}^{-1}D_{13}{}'\big)(C_1 + D_{12}F_pC_2))PC_2{}' \quad (6.16)$$

$$\partial\mathcal{L}/\partial P = \big(A + B_2F_pC_2 - B_3R_1{}^{-1}D_{13}{}'(C_1 + D_{12}F_pC_2)\big)'X + X\big(A + B_2F_pC_2 - B_3R_1{}^{-1}D_{13}{}'(C_1 + D_{12}F_pC_2)\big) - XB_3R_1{}^{-1}B_3{}'X + (C_1 + D_{12}F_pC_2)'\big(I - D_{13}R_1{}^{-1}D_{13}{}'\big)(C_1 + D_{12}F_pC_2) \quad (6.17)$$

$$\partial\mathcal{L}/\partial X = P\big(A + B_2F_pC_2 - B_3R_1{}^{-1}D_{13}{}'\big(C_1 + D_{12}F_pC_2\big) - B_3R_1{}^{-1}B_3{}'X\big)' + \big(A + B_2F_pC_2 - B_3R_1{}^{-1}D_{13}{}'\big(C_1 + D_{12}F_pC_2\big) - B_3R_1{}^{-1}B_3{}'X\big)P + B_1B_1{}' \quad (6.18)$$

The gradient $\partial\mathcal{L}/\partial F_p$ is actually the partial derivative of the Lagrange function $\mathcal{L}$ with respect to the structural design variables in F_p, which has the form in (6.4). Therefore, by picking out the entries corresponding to the structural design variables, $\partial\mathcal{L}/\partial F_p$ actually is

$$\partial\mathcal{L}/\partial F_p = 2\Big(B_2{}'X - D_{12}{}'D_{13}R^{-1}B_3{}'X + D_{12}{}'(I - D_{13}R^{-1}D_{13}{}')\big(C_1 + D_{12}F_pC_2\big)\Big)PC_2{}' \odot F_d \quad (6.19)$$

where $\odot$ is the operator of entry-by-entry multiplication of matrix. F_d is a matrix with entry one in the positions corresponding to the structural design variables and zeros for the rest of the entries.

$$F_d = \begin{bmatrix} 1 & 1 & & \\ & & 1 & 1 \\ & & & \ddots \end{bmatrix} \quad (6.20)$$

Hence, Equation (6.19) ensures that $\partial\mathcal{L}/\partial F_p$ has the structure in (6.4), which makes F_p practical to be realized by the aforementioned passive elements. Furthermore, for mechanical systems, the stiffness and damping are nonnegative values which means $F_{pij} \geq 0$ for all i, j. To handle this additional constraint, we can conveniently replace F_{pij} with F_{pij}^2 and make a corresponding modification to the gradients of $\mathcal{L}$. More generally, if we would like to constrain some parameter

F_{pij} to be in some physically achievable interval $[r_1, r_2]$, we can specify F_{pij} with one parameter r as in $F_{pij} = \frac{1}{2}(r_2 + r_1) + \frac{1}{2}(r_2 + r_1)\sin(\alpha r)$, where α is a scaling coefficient chosen to accelerate convergence and the gradient is evaluated using the chain rule. The proposed integrated design method guarantees at least one locally optimal solution for the F_p (Remainder: F_a is a function of F_p). For most linear mechanical systems, we may constrain the structural design parameters to be in some physically achievable interval so that the obtained design solution is desirable in practice.

Thus, the set of necessary conditions for the H_2 optimization of the ISSC design problem in (6.14) are given by

$$(A + B_2 F_p C_2, B_3) \text{ is stabilizable;} \tag{6.21}$$

$$D_{13} \text{ has full column rank;} \tag{6.22}$$

$$\begin{bmatrix} A + B_2 F_p C_2 - j\omega I & B_3 \\ C_1 + D_{12} F_d C_2 & D_{13} \end{bmatrix} \text{ has full column rank for all } \omega; \tag{6.23}$$

$$\partial \mathcal{L}/\partial F_p = 0; \tag{6.24}$$

$$\partial \mathcal{L}/\partial P = 0; \tag{6.25}$$

$$\partial \mathcal{L}/\partial X = 0; \tag{6.26}$$

Requirements (6.21) − (6.23) are extended from the assumptions of the conventional H_2 controller design in Theorem 1, as to enforce the controllability of the mechanical systems and to avoid the singularities of the Riccati-based algorithms. Conditions (6.24)− (6.26) are the optimal conditions for the Lagrange function formed in (6.15).

To solve the nonlinear equation set (6.24)− (6.26) with the additional requirements (6.21)− (6.23), we can employ a gradient-based optimization algorithm, such as steepest-descent, BFGS quasi-Newton methods [69]. The optimization procedures are summarized as follows:

Step 1. Set the initial value of the passive feedback gain F_{p0} for the integrated design problem. Typically, the parameters of the conventional passive system can be a good set of the initial values of the design parameters.

Step 2. Set the stop criterion that the norm of all the entries $\left\| \partial \mathcal{L} / \partial F_{p_{ij}} \right\| \leq \varepsilon$ where ε is a very small positive number. A common value of ε ranges in $[10^{-5}, 10^{-10}]$. The smaller the ε is, the more accurate the result is, while the more computation effort is required.

Step 3. With a given F_p, equations $\partial \mathcal{L}/\partial P = 0$ (6.25) and $\partial \mathcal{L}/\partial X = 0$ (6.26) reduce to two decoupled algebraic Riccati equations. These equations can be solved rapidly for the Riccati matrix X and the Lagrange multiplier P. With a set of F_p, X, P, the gradient $\partial \mathcal{L} / \partial F_p$ can be obtained using Equation (6.19). We can also prove that $\partial \mathcal{L} / \partial F_p$ is equal to the gradient $d(J(F_p))/dF_p$ [68]. If $\partial \mathcal{L} / \partial F_p$ satisfies the stop criterion in *Step 2*, then stop. Otherwise go to *Step 4*.

Step 4. Based on the gradient $\partial \mathcal{L} / \partial F_p$, calculate a search direction D_f and choose a proper step size α based a gradient-based solution method mentioned above. Then update the F_p with $F_p + \alpha D_f$ with the additional requirements (6.21) - (6.23). Then go back to *Step 3*.

After obtaining the optimal passive feedback gain, F_p, for the ISSC design problem (6.14) from *Step 1~4*, the optimal state-feedback gain, F_a, is then constructed by Equation (6.12) and the corresponding closed-loop system is

$$\begin{cases} \dot{x} = \left(A + B_2 F_p C_2 + B_3 F_a\right) x + (B_1 + B_2 F_p D_{21}) w \\ z = (C_1 + D_{12} F_d C_2 + D_{13} F_a) x \end{cases} \tag{6.27}$$

It should be noted that if the aforementioned non-negative constraints are added for the structural design parameters F_p, the additional requirements (6.21) - (6.23) are usually automatically satisfied. It should also be noted that the proposed method is able to design more general linear mechanical systems as long as the system can be written into the dual-loop framework in (6.1). For instance, we can conveniently modify u_p and y_p to design the parallel spring-mass-damper system as well. Similar to the serial spring-mass-damper system in Figure 6.1, we can set u_p as the reaction force of the spring and damper and then modify y_p according to the actual configuration of the parallel spring-mass-damper system. Once the parallel spring-mass-damper system is written into the framework in (6.1), the rest solving procedures remain the same.

6.3 The Integrated Structure and Output-feedback Controller (ISOC) Design Problem

6.3.1 Problem formulation

If some states are not available to be measured in System (6.1), we have to consider the integrated structure and output-feedback controller (ISOC) design problem, in which the observer is also taken into account. For the ISOC design problem, we form the linear mechanical system, shown in Figure 6.1, as

$$\begin{cases} \dot{x} = Ax + B_1 w + B_2 u_p + B_3 u_a \\ z = C_1 x + D_{11} w + D_{12} u_p + D_{13} u_a \\ y_p = C_2 x + D_{21} w \\ y_a = C_3 x + D_{31} w + D_{32} u_p + D_{33} u_a \end{cases} \tag{6.28}$$

where $y_a \in \mathbb{R}^{n_{ya}}$ is the output measurement which is measured to generate the active control force as

$$\begin{cases} \dot{x_G} = A_G x_G + B_G y_a \\ u_a = C_G x_G + D_G y_a \end{cases} \tag{6.29}$$

The passive feedback forces u_p has the same form as that in the ISSC design problem

$$u_p = F_p y_p \tag{6.30}$$

Therefore, the ISOC design problem can be similarly formed as

$$\begin{cases} min & J(F_p, A_G, B_G, C_G, D_G) \\ s.t. & (28), (29), (30) \\ & (F_p, A_G, B_G, C_G, D_G) \in (S_p, S_G) \end{cases} \tag{6.31}$$

where S_G is the feasible domain of (A_G, B_G, C_G, D_G), which is a set of matrices with the appropriate dimensions of the output-feedback controller in (29). The ISOC design problem (6.31) is depicted by the dual-loop block diagram shown in Figure 6.3.

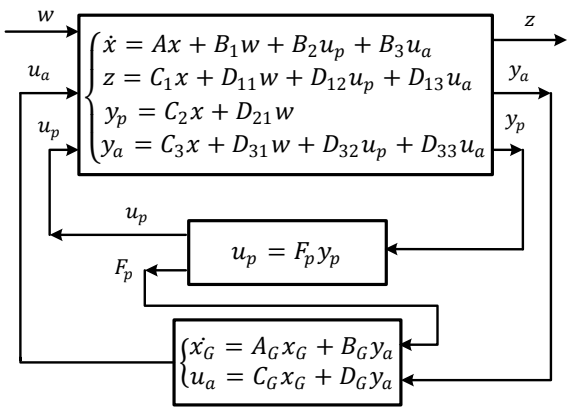

Figure 6.3. Dual-loop block diagram of the integrated structure and output-feedback controller.

6.3.2 The ISOC design problem with H_2 performance criteria

For a causal LTI system with output measurement

$$\begin{cases} \dot{\tilde{x}} = \tilde{A}\tilde{x} + \tilde{B}_w\tilde{w} + \tilde{B}_u\tilde{u} \\ \tilde{z} = \tilde{C}_1\tilde{x} + \tilde{D}_u\tilde{u} \\ \tilde{y} = \tilde{C}_2\tilde{x} + \tilde{D}_w\tilde{w} \end{cases} \tag{6.32}$$

the conventional H_2 output-feedback controller can be designed by using Theorem 2, which can be found in Appendix C. Similarly, the system in (6.28) can be reformed by plugging in $u_p = F_p y_p$

$$\begin{cases} \dot{x} = \left(A + B_2 F_p C_2\right)x + (B_1 + B_2 F_p D_{21})w + B_3 u_a \\ z = (C_1 + D_{12} F_p C_2)x + (D_{11} + D_{12} F_p D_{21})w + D_{13} u_a \\ y_a = C_3 x + D_{31} w + D_{32} u_p + D_{33} u_a \end{cases} \tag{6.33}$$

Here D_{11} and D_{21} can also be taken as zero to obtain a finite H_2 norm of the closed-loop system. Additionally, D_{32} and D_{33} can be assumed to be zero without any loss of generality [34]. Thus, applying Theorem 2 to the system in (6.33), its H_2 norm is minimized to

$$min \ \ \|H_{zw}\|_2^2 = trace\left(\left(C_1 + D_{12}F_pC_2\right)Y\left(C_1 + D_{12}F_pC_2\right)'\right) + trace\big(R_2{}^{-1}(YC_3{}' + B_1D_{31}{}')'X(YC_3{}' + B_1D_{31}{}')\big) \tag{6.34}$$

with the output-feedback controller in (6.29), where

$$\begin{cases} A_G = A + B_2F_pC_2 + B_3F_a + L_aC_3 \\ B_G = -L_a \\ C_G = F_a \\ D_G = 0 \end{cases} \tag{6.35}$$

F_a and X are obtained by Equations (6.12) and (6.13). The observer gain, L_a, is obtained as

$$L_a = -(YC_3{}' + B_1D_{31}{}')R_2^{-1} \tag{6.36}$$

where $R_2 = D_{31}D_{31}'$ and Y is the solution to the modified algebraic Riccati equation below

$$\big(A + B_2F_pC_2 - B_1D_{31}{}'R_2{}^{-1}C_3\big)Y + Y\big(A + B_2F_pC_2 - B_1D_{31}{}'R_2{}^{-1}C_3\big)' - YC_3{}'R_2{}^{-1}C_3Y + B_1(I - D_{31}{}'R_2{}^{-1}D_{31})B_1{}' = 0 \tag{6.37}$$

Since the optimal output-feedback controller in (6.29) is also a function of F_p, the ISOC design problem with H_2 criteria in (6.31) can be similarly reformed as a constrained structural optimization problem with two Riccati-equation based constraints (6.13) and (6.37), as stated below

$$\begin{cases} min & J(F_p) \triangleq trace\left(\left(C_1 + D_{12}F_pC_2\right)Y\left(C_1 + D_{12}F_pC_2\right)'\right) \\ & \quad + trace\big(R_2{}^{-1}(YC_3{}' + B_1D_{31}{}')'X(YC_3{}' + B_1D_{31}{}')\big) \\ s.t. & (13)\ (37)\ and\ F_p \in S_p \end{cases} \tag{6.38}$$

It should be noted that the reformed ISOC design problem in (6.38) reduces the independent design variables from the structural parameters F_p and the active controllers A_G, B_G, C_G, D_G to the

structural parameters F_p only. This significantly reduces the quantity of the independent design variables. The Lagrange function corresponding to the ISOC design problem in (38) is defined as

$$\mathcal{L}(F_p, X, Y, P, Q) = trace\left((C_1 + D_{12}F_pC_2)Y(C_1 + D_{12}F_pC_2)'\right) + trace(R_2{}^{-1}(YC_3' + B_1D_{31}')'X(YC_3' + B_1D_{31}')) + trace\left\{\left[\left(A + B_2F_pC_2 - B_3R^{-1}D_{13}'(C_1 + D_{12}F_pC_2)\right)'X + X\left(A + B_2F_pC_2 - B_3R^{-1}D_{13}'(C_1 + D_{12}F_pC_2)\right) - XB_3R^{-1}B_3'X + (C_1 + D_{12}F_pC_2)'(I - D_{13}R^{-1}D_{13}')(C_1 + D_{12}F_pC_2)\right]P\right\} + trace\left\{\left[(A + B_2F_pC_2 - B_1D_{31}'R_2{}^{-1}C_3)Y + Y(A + B_2F_pC_2 - B_1D_{31}'R_2{}^{-1}C_3)' - YC_3'R_2{}^{-1}C_3Y + B_1\left(I - D_{31}'R_2{}^{-1}D_{31}\right)B_1'\right]Q\right\} \quad (6.39)$$

where X, Y are the Riccati matrices and P, Q are the matrix Lagrange multipliers. F_p, X, Y, P, Q are the matrix variables to be determined to minimize the system H_2 norm. Then using matrix calculus, the closed-form gradients of $\mathcal{L}$ can be obtained as

$$\partial\mathcal{L}/\partial F_p = (2\left(B_2'Q + D_{12}'(C_1 + D_{12}F_pC_2)\right)YC_2' + 2(B_2'X - D_{12}'D_{13}R_1{}^{-1}B_3'X + D_{12}'\left(I - D_{13}R_1{}^{-1}D_{13}'\right)(C_1 + D_{12}F_pC_2))PC_2') \odot F_d \quad (6.40)$$

$$\partial\mathcal{L}/\partial P = \left(A + B_2F_pC_2 - B_3R_1{}^{-1}D_{13}'(C_1 + D_{12}F_pC_2)\right)'X + X\left(A + B_2F_pC_2 - B_3R_1{}^{-1}D_{13}'(C_1 + D_{12}F_pC_2)\right) - XB_3R_1{}^{-1}B_3'X + (C_1 + D_{12}F_pC_2)'\left(I - D_{13}R_1{}^{-1}D_{13}'\right)(C_1 + D_{12}F_pC_2) \quad (6.41)$$

$$\partial\mathcal{L}/\partial Q = \left(A + B_2F_pC_2 - B_1D_{31}'R_2{}^{-1}C_3\right)Y + Y\left(A + B_2F_pC_2 - B_1D_{31}'R_2{}^{-1}C_3\right)' - YC_3'R_2{}^{-1}C_3Y + B_1\left(I - D_{31}'R_2{}^{-1}D_{31}\right)B_1' \quad (6.42)$$

$$\partial\mathcal{L}/\partial X = (YC_3' + B_1D_{31}')R_2{}^{-1}(YC_3' + B_1D_{31}')' + P\left(A + B_2F_pC_2 - B_3R_1{}^{-1}D_{13}'\left(C_1 + D_{12}F_pC_2\right) - B_3R_1{}^{-1}B_3'X\right)' + \left(A + B_2F_pC_2 - B_3R_1{}^{-1}D_{13}'\left(C_1 + D_{12}F_pC_2\right) - B_3R_1{}^{-1}B_3'X\right) \quad (6.43)$$

$$\partial\mathcal{L}/\partial Y = \left(C_1 + D_{12}F_pC_2\right)'\left(C_1 + D_{12}F_pC_2\right) + C_3'R_2^{-1}(C_3Y + D_{31}B_1')X + X(YC_3{}' + B_1D_{31}{}')R_2^{-1}C_3 + \left(A + B_2F_pC_2 - B_1D_{31}{}'R_2{}^{-1}C_3 - YC_3'R_2{}^{-1}C_3\right)'Q + Q(A + B_2F_pC_2 - B_1D_{31}{}'R_2{}^{-1}C_3 - YC_3'R_2{}^{-1}C_3) \quad (6.44)$$

Therefore, the set of necessary conditions for the H_2 optimization of the ISOC problem in (6.38) is

$\left(A + B_2F_pC_2, B_3\right)$ is stabilizable and $(C_3, A + B_2F_pC_2)$ is detectable; (6.45)

D_{13} has full column rank and D_{31} has full row rank; (6.46)

$\begin{bmatrix} A + B_2F_pC_2 - j\omega I & B_3 \\ C_1 + D_{12}F_pC_2 & D_{13} \end{bmatrix}$ has full column rank for all ω; (6.47)

$\begin{bmatrix} A + B_2F_pC_2 - j\omega I & B_1 + B_2F_pD_{21} \\ C_3 & D_{31} \end{bmatrix}$ has full row rank for all ω; (6.48)

$\partial\mathcal{L}/\partial F_p = 0$; (6.49) $\partial\mathcal{L}/\partial P = 0$; (6.50) $\partial\mathcal{L}/\partial Q = 0$; (6.51)

$\partial\mathcal{L}/\partial X = 0$; (6.52) $\partial\mathcal{L}/\partial Y = 0$; (6.53)

Similarly, requirements (6.45) − (6.48) are extended from the assumptions of the conventional H_2 output-feedback controller design in Theorem 2 to ensure that the ISOC design problem is feasible. Then conditions (6.49) ~ (6.53) are used to find the optimal solution to the ISOC problem formed in (6.38). The optimal result of the ISOC problem can be similarly obtained by using the procedures summarized in Section 2. It should be noted that (6.50) and (6.51) are two decoupled Riccati equations in matrix variables X and Y with a given F_p and that (6.52) and (6.53) are two decoupled Riccati equations in matrix variables P and Q with a set of F_p, X and Y. When the optimal passive feedback gain F_p and the optimal active controller (6.29) are obtained, the closed-loop integrated design system with the output-feedback controller is given by

$$\begin{cases} \begin{bmatrix} \dot{x} \\ \dot{x_G} \end{bmatrix} = \begin{bmatrix} A + B_2 F_p C_2 & B_3 C_G \\ B_G C_3 & A_G \end{bmatrix} \begin{bmatrix} x \\ x_G \end{bmatrix} + \begin{bmatrix} B_1 \\ B_G D_{31} \end{bmatrix} w \\ z = [C_1 + D_{12} F_d C_2 \quad D_{13} C_G] \begin{bmatrix} x \\ x_G \end{bmatrix} \end{cases} \tag{6.54}$$

6.4 Applications and Design Examples

6.4.1 Integrated design of an active seat and passive suspension system (ISOC design example)

To illustrate the proposed method, the first example is to redesign an active seat and passive suspension system of a bus by using the proposed integrated design method. The conventional passive seat-suspension system of a bus can be approximated as a 3-DOF system referred to as the nominal passive system shown in Figure 6.4(a). The parameters of the nominal passive system, as listed in Table 6.1, are cited from [70]. To enhance the performance of the vehicle suspension system, an active seat and passive suspension system has been proposed in [71]. In this active seat and passive suspension system, the passive damper under the seat is replaced by an active controller of which the force is adjusted to provide better ride performance, as shown in Figure 6.4(b). For comparison, we design a conventional H_2 output-feedback controller based on the active-seat system with the same passive structural parameters of the nominal passive system. Such a system is referred to as the nominal active system. To further enhance the suspension performance, we redesign the active seat and passive suspension system by using the proposed integrated design method to simultaneously optimize the suspension stiffness k_s^*, the suspension damping c_s^* and the output-feedback controller u_a. Such a system is referred to as the integrated design system shown in Figure 6.4(c). For comparison with the performance of the above nominal passive system and nominal active system, the rest structural parameters of the integrated design system are chosen to be the same as those of the nominal passive system.

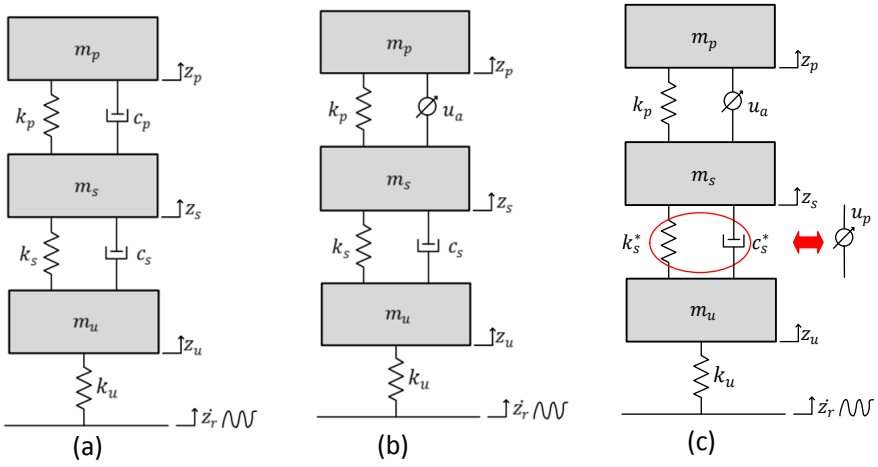

Figure 6.4. (a) Conventional active-passive suspension system (nominal passive system), (b) Conventional passive seat-suspension system (nominal active system), (c) Integrated active-passive suspension system (integrated design system).

Table 6.1. Parameters and nomenclature of the 3-DOF vehicle suspension system

Description	Symbol	Value
Sprung mass	m_s	4500 [kg]
Unsprung mass	m_u	500 [kg]
Mass of seat and driver	m_p	100 [kg]
Stiffness of tire	k_u	1600 [kN/m]
Stiffness of driver's seat	k_p	2.5 [kN/m]
Damping of driver's seat	c_p	1 [kNs/m]
Nominal stiffness of suspension	k_s	300 [kN/m]
Nominal damping of suspension	c_s	20 [kNs/m]
Integrated stiffness of suspension	k_s^*	To be optimized
Integrated damping of suspension	c_s^*	To be optimized
Road velocity disturbance	$\dot{z}_r$	White noise

Vehicle suspensions are disturbed by white-noise road unevenness $\dot{z}_r$. Therefore, to effectively improve the performance of the active-passive suspension system, we can cast the integrated design of the suspension system as an ISOC problem, which minimizes the closed-loop H_2 norm from $\dot{z}_r$ to the cost z. In this system, u_a is the control force implemented by the active actuator under the seat. The output measurement y_a is the relative velocity of the seat and sprung mass with taking into account sensing noises

$$y_a = \dot{z_p} - \dot{z_s} + 0.1w_s$$

where w_s is the sensing noise. u_p is the reaction force of the suspension's spring and damper, which can be written as

$$u_p = k_s^*(z_s - z_u) + c_s^*(\dot{z}_s - \dot{z}_u)$$

Hence, the corresponding y_p is written as

$$y_p = [z_s - z_u \quad \dot{z_s} - \dot{z_u}]'$$

and F_p is composed of the stiffness and damping of the suspension to be designed

$$F_p = [k_s^* \quad c_s^*]$$

Since vehicle suspensions intend to improve ride comfort, decrease system stroke and maintain the contact between the tire and road, the weighted cost is chosen to be [72]

$$z = E[z_u - z_r \quad z_p - z_u \quad \ddot{z}_p]'$$

where E is the weighting matrix

$$E = \begin{bmatrix} e_1 & 0 & 0 \\ 0 & e_2 & 0 \\ 0 & 0 & e_3 \end{bmatrix}$$

Here, we choose them to be [72]

Weights	e_1	e_2	e_3
Value	1100	110	1

Defining the system states

$$x = [z_u - z_r \quad \dot{z}_u \quad z_s - z_u \quad \dot{z}_s \quad z_p - z_s \quad \dot{z}_p]'$$

and using the proposed method, we can obtain the optimal parameters of the suspension stiffness and the damping coefficient

$$F_p = [k_s^* \quad c_s^*] = [126.3\text{kN/m} \quad 24.40\text{kNs/m}]$$

and the optimal controller in the form of the transfer function from y_a to u_a

$$G(s) = \frac{(1.4s^5 + 69.21s^4 + 4312s^3 - 3114s^2 - 286100s - 439000) \times 10^5}{s^6 + 118.2s^5 + 7554s^4 + 265800s^3 + 488600s^2 + 7.074 \times 10^6\, s + 9.875 \times 10^6}$$

To show the high efficiency of the proposed integrated design method over BMI-based methods, we choose the well-cited BMI-based method proposed in [74] as a benchmark to compare with the proposed method. In this example problem, there are only two independent design variables to be optimized by using the proposed method, which are the suspension stiffness k_s and the damping c_s. However, the benchmark method needs to optimize 51 design variables consisting of 2 structural design parameters and 49 design parameters of the active controllers (A_G, B_G, C_G, D_G). Therefore, the computational efficiency can be significantly improved by using the proposed integrated design method due to largely reducing the number of the independent design variables. It should be noted that the optimal results obtained by the proposed method and the benchmark method are the same as expected.

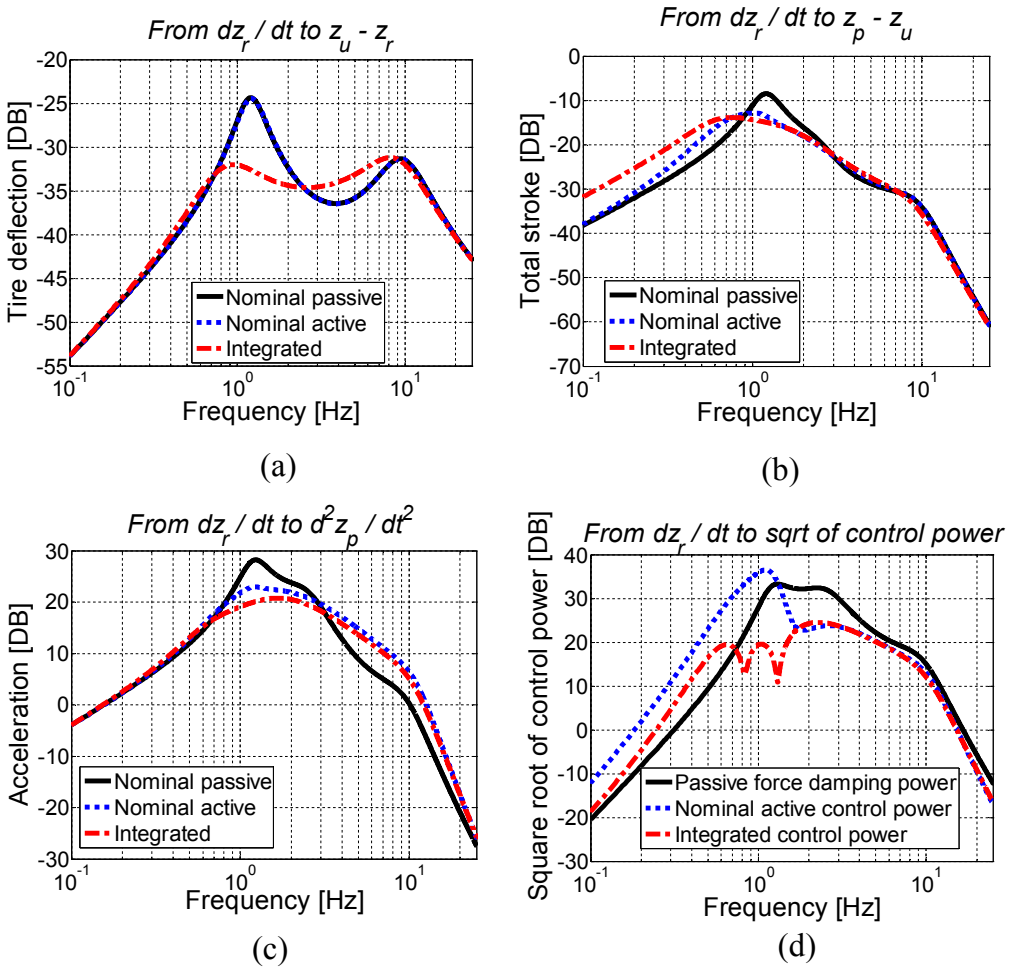

Figure 6.5. (a) Frequency response from road velocity $\dot{z_r}$ to tire deflection $(z_u - z_r)$. (b) Frequency response from road velocity velocity $\dot{z_r}$ to total stroke $(z_p - z_u)$. (c) Frequency response from road velocity $\dot{z_r}$ to seat accelerations $\ddot{z_p}$. (d) Frequency response from road velocity $\dot{z_r}$ to square root of control power $\sqrt{u_a\,(\dot{z}_p - \dot{z}_s)}$.

The H_2 output-feedback controller of the nominal active system is also designed based on the weighted cost z defined above. The frequency responses of the integrated design, from the disturbance $\dot{z}_r$ to the tire deflection $z_u - z_r$, to the total stroke $z_p - z_u$, to the seat accelerations $\ddot{z}_p$ and to the square root of the control power $\sqrt{u_a(\dot{z}_p - \dot{z}_s)}$, are plotted in Figure 6.5 in comparison with those of the nominal passive system and the nominal active system. Their corresponding H_2 performances are summarized in Table 6.2. As a comparison from Figure 6.5 and Table 6.2, it is clear that the integrated design outperforms the nominal passive system and the

nominal active system in terms of all the performance of interest. In addition to regular road unevenness, the analysis of the vehicles rolling over the speed bump is also carried out to show the advantage of the integrated design. The dimensions of the speed bump is shown in Figure 6.6(a). Figure 6.6(b)~(d) plot the speed bump responses when the vehicle rolls over the speed bump at 4 [m/s]. As expected, the integrated design system achieves the best performance in terms of faster convergence to its equilibrium and smaller peak values of the response.

Table 6.2, Performance of the integrated active-passive suspension system

Performance	Integrated optimal	Nominal active	Nominal passive
under unit intensity white noise disturbance $\dot{z_r}$			
Total weighted H_2 norm $\left\|H_{\dot{z_r}\to z}\right\|_2$	**211.068**	221.769	224.081
RMS Tire deflection, $\left\|H_{\dot{z_r}\to(z_u-z_r)}\right\|_2$ [m]	**0.136**	0.1430	0.1431
RMS Total stroke, $\left\|H_{\dot{z_r}\to(z_p-z_u)}\right\|_2$ [m]	**0.375**	0.378	0.4771
RMS Acceleration, $\left\|H_{\dot{z_r}\to\ddot{z_p}}\right\|_2$ [m/s^2]	**27.053**	32.307	37.567
under unit magnitude sinusoid disturbance $\dot{z_r}$			
Peak magnitude of tire deflection [m]	**-31.187 [dB]**	-24.433 [dB]	-24.343 [dB]
Peak magnitude of total stroke [m]	**-13.820 [dB]**	-12.817 [dB]	-8.465 [dB]
Peak magnitude of acceleration [m/s^2]	**20.784 [dB]**	22.962[dB]	28.221[dB]

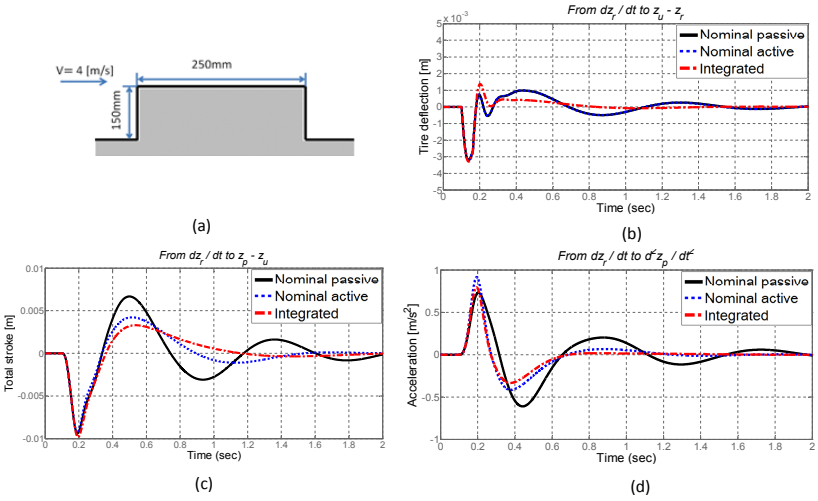

Figure 6.6. The system response of the vehicle passing through a speed bump. (a) Speed bump dimensions. (b) Response of tire deflection$(z_u - z_r)$. (c) Response of total stroke $(z_p - z_u)$. (d) Response of seat acceleration $\ddot{z_p}$.

In practice, it is difficult to make the design parameters exactly equal to their desired values. Therefore, to study the sensitivity of each design parameter to the overall performance of the integrated active-passive suspension system, we plotted Figure 6.7 to show the changes of the total weighted H_2 norm $\left\|H_{\dot{z}_r \to z}\right\|_2$ with the changes of design parameters from 0.5 to 1.5 times of their optimal values. As shown in Figure 6.7, the optimal structural parameters and controllers obtained using the proposed integrated design method can achieve the minimum closed-loop H_2 norm. Any bias of the structural parameters will increase the closed-loop H_2 norm. Therefore, we can conclude that the obtained result is the optimal result. It can also be seen that the suspension k_s is less sensitive to the overall system performance while c_s is more sensitive. The insensitivity of the suspension stiffness, k_s, can allow us to design the system with more flexibilities. It should be noted that the proposed method is also able to design other integrated system, like the active-passive building with tuned mass damper system [75].

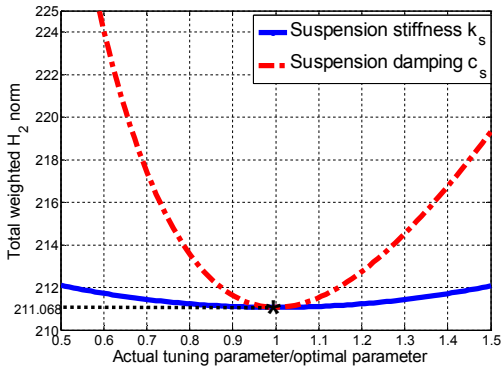

Figure 6.7. The performance of the vehicle suspension system to the changes of the independent design variables: the suspension stiffness k_s and the suspension damping c_s.

6.5 Chapter Summary

By combining decentralized control techniques and Riccati based control theories, this chapter proposes an efficient integrated design method to simultaneously optimize the coupled structural design parameters and controllers of linear mechanical systems, which aims at minimizing the closed-loop H_2 norm. By developing a dual-loop control system framework, the original integrated design problem is transferred to a constrained structural design problem with some additional

Riccati-equation-based constraints simultaneously integrating the controller synthesis. This reduces the independent design variables from the structural design parameters and the parameters of the controller to the structural design parameters only. In the first design example, the quantity of original independent design variables is reduced from 51 to 2 by using the proposed method. As a result, the optimization efficiency is significantly improved. Then, the constrained structural design problem is reformed as an unconstrained optimization problem by introducing Lagrange multipliers and a Lagrange function, which can be efficiently solved by gradient-based optimization algorithms. In the design example of the active-passive vehicle suspension system, we show that the performance of the integrated design is significantly improved in terms of ride comfort, suspension stroke and tire contact. Compared to conventional systems, the RMS value of the seat acceleration of the integrated design system is approximately reduced by 16.4%, which results in enhanced ride comfort. This method can be applied to the integrated design of the vehicle suspension system with the controllable regenerative shock absorbers to achieve enhanced vibration mitigation performances. More generally, this method can also be utilized to design general linear vibration systems equipped with controllers, which improves the scientific value of this dissertation.

7 Conclusion and Future work

Up to now, the following conclusions can be drawn from the work accomplished in this dissertation.

1. Through the numerical and experimental verification, this dissertation proves that the regenerative electromagnetic damper or shock absorber is able to effectively mitigate the vibration of vibration systems. It can act as a traditional viscous damper when connected to a constant external resistive load. Moreover, the vibration mitigation performance can be further improved when the regenerative electromagnetic damper is connected to a high-order electrical impedance. Meanwhile, the regenerative electromagnetic damper or shock absorber is able to harvest the vibration energy otherwise dissipated by the traditional viscous damper.

2. The regenerative electromagnetic shock absorber can also work as a semi-active controllable damper when its external electrical load is being adjusted. A new suspension damping control algorithm is proposed to control the electromagnetic shock absorber in improving the performance of vehicle suspensions. The experiment of controlling vehicle suspensions with the electromagnetic shock absorber has been conducted on a scaled quarter car test rig, which verifies the function of the regenerative electromagnetic shock absorber in semi-actively controlling vehicle suspension systems.

3. A novel mechanical-motion-rectifier-based (MMR-based) regenerative shock absorber using ball-screw mechanism is proposed in this dissertation. Compare to existing linear electromagnetic shock absorbers, the proposed one is able to provide large damping force and increase generated power density. Extensive theoretical and experimental analysis is conducted to characterize the superior characteristics of the proposed shock absorber. The result shows that the proposed regenerative shock absorber can also work as a controllable damper connecting with different resistive loads. Meanwhile, it has higher energy harvesting efficiency and power density.

4. The coupled dynamics of the suspension system with the proposed MMR-based shock absorber is explored and optimized. Meanwhile, a new control algorithm is proposed to control the proposed

shock absorber considering its unique dynamics. The results show that the controlled proposed shock absorber can potentially improve ride comfort compared to conventional oil dampers.

5. A new integrated design framework is proposed in this dissertation, which aims to design the structural parameters and the controllers of mechanical systems at the same time. This method can be applied to the integrated design of the vehicle suspension system with the controllable regenerative shock absorbers to achieve enhanced vibration mitigation performances. More generally, this method can also be utilized to design general linear vibration systems equipped with controllers, which improves the scientific value of this dissertation.

The future work is summarized as follows.

1. Experimentally implement the semi-active control strategy based on the optimized shock absorber and demonstrate improved performance of the semi-active MMR-based shock absorber in vehicle suspension systems.

2. Design energy-harvesting circuits using novel dc-dc converters and integrate the proposed shock absorber into real vehicle systems.

References

[1] Kareem, A., Kijewski, T. and Tamura, Y., "Mitigation of motions of tall buildings with specific examples of recent applications", *Wind and Structures*, vol. 2, no. 3, pp. 201-251, 1999.

[2] Schwartz, T.A., "When bad things happen to good buildings", *Architecture Week*, 2001.

[3] U.S. Department of energy [Online]. Available: http://www.fueleconomy.gov/FEG/atv.shtml

[4] Karnopp, D., Crosby, M., and Harwood, R. A., "Vibration control using semi-active suspension control," *Journal of Engineering for Industry*, vol. 96, pp. 619-626, 1974.

[5] Sammier, D., Sename, O., and Dugard, L., "Skyhook and H_∞ control of semi-active suspensions: some practical aspects," *Vehicle System Dynamics*, vol. 39, no. 4, pp. 279-308, 2003.

[6] Savaresi, S.M., Silani, E., and Bittanti, S., "Acceleration-Driven-Damper (ADD): An optimal control algorithm for comfort-oriented semi-active suspensions," *Journal of dynamic systems, measurement, and control*, vol. 127, no. 2, pp. 218-229, 2005.

[7] Savaresi, S.M., and Spelta, C., "Mixed Sky-hook and ADD: approaching the filtering limits of a semi-active suspension," *Journal of Dynamic Systems, Measurement, and Control*, vol. 129, no. 4, pp. 382-392, 2007.

[8] Morselli, R., and Zanasi, R., "Control of Port Hamiltonian systems by dissipative devices and its application to improve the semi-active suspension behavior," *Mechatronics*, vol.18, no. 7, pp. 364-369, 2008

[9] Ahmadian, M., Song, X., and Southward, S.C., "No-Jerk Skyhook control methods for semi-active suspensions," *ASME Journal of Vibration and Acoustics*, vol. 126, no. 4, pp. 580-584, 2004

[10] Valasek, M., Novak, M., Sika, Z., and Vaculin, O., "Extended ground-hook: new concept of semi-active control of truck's suspension," *Vehicle System Dynamics*, vol. 27 no.5-6, pp. 289-303, 1997.

[11] Tseng, H. E. and Hedrick, J. K., "Semi-active control laws-optimal and sub-optimal," *Vehicle System Dynamics*, vol. 23, no. 1, pp. 545-569, 1994.

[12] Giorgetti, N., Bemporad, A., Tseng, H. E., and Hrovat, D., "Hybrid model predictive control application towards optimal semi-active suspension," *International Journal of Control*, vol. 79, no. 5, pp. 521-53, 2006.

[13] Poussot-Vassala, C., Senamea, O., Dugarda, L., Gsprb, P., Szabb, Z., and Bokorb, J., "A new semi-active suspension control strategy through LPV technique," *Control Engineering Practice*, vol. 6, no. 12, pp. 1519-1534, 2004.

[14] Karnopp, D., "Permanent magnet linear motors used as variable mechanical dampers for vehicle suspensions," *Vehicle System Dynamics*, vol. 18, no. 4, pp.187–200, 1989.

[15] Goldner, R.B., Zerigian, P. and Hull, J.R., "A preliminary study of energy recovery in vehicles by using regenerative magnetic shock absorbers," Paper SAE 2001-01-2071, SAE/DOE Government/Industry Meeting, Washington, DC, 2001.

[16] Gupta, A., Jendrzejczyk, J.A., Mulcahy, T.M. and Hull, J.R., "Design of electromagnetic shock absorbers," *International Journal of Mechanics and Materials in Design*, vol. 3, no. 3, pp. 285–291, 2006.

[17] Martins, I., Esteves, J., Marques, G.D. and Silva, F.P.D., "Permanent-magnets linear actuators applicability in automobile active suspensions," *IEEE Transaction on Vehicular Technology*, vol. 55, no. 1, pp. 86–94, 2006.

[18] Zuo, L., Scully, B., Shestani, J. and Zhou, Y., "Design and characterization of an electromagnetic energy harvester for vehicle suspensions," *Smart Material and Structures*, vol. 19, no. 4, pp. 045003, 2010.

[19] Chen, C. and Liao, W.H., "A self-sensing magnetorheological damper with power generation," *Smart Material and Structures*, vol. 21, no. 2, pp. 025014, 2012.

[20] Tang, X., Lin, T. and Zuo, L., "Design and optimization of a tubular linear electromagnetic vibration energy harvester," *IEEE/ASME Transactions on Mechatronics*, vol. 19, no.2, pp.615-622, 2014.

[21] Zhang, Y., Huang, K., Yu, F., Gu, Y., and Li, D., "Experimental verification of energy-regenerative feasibility for an automotive electrical suspension system," *Vehicular Electronics and Safety. ICVES. IEEE International Conference on*, pp. 1-5, 2007.

[22] Kawamoto, Y., Suda, Y., Inoue, H. and Kondo, T., "Electro-mechanical suspension system considering energy consumption and vehicle maneuver," *Vehicle System Dynamics*, vol. 46, no. S1, pp.1053-1063, 2008.

[23] Cassidy, I.L., Scruggs, J.T., Behrens, S. and Gavin, H.P. "Design and experimental characterization of an electromagnetic transducer for large-scale vibratory energy harvesting applications," *Journal of Intelligent Material Systems and Structures*, vol. 22, no.17, pp.2009-2024, 2011.

[24] Li, Z., Zuo, L., Luhrs, G., Lin, L. and Qin, Y.X. "Electromagnetic energy-harvesting shock absorbers: design, modeling, and road tests," *Vehicular Technology, IEEE Transactions on*, vol. 62, no. 3, pp.1065-1074, 2013.

[25] Maravandi, A., and Mehrdad M., "Regenerative shock absorber using a two-leg motion conversion mechanism," *Mechatronics, IEEE/ASME Transactions on*, vol. 20, no. 6, pp. 2853-2861, 2015.

[26] Li, Z., Zuo, L., Kuang, J. and Luhrs, G., "Energy-harvesting shock absorber with a mechanical motion rectifier," *Smart Materials and Structures*, vol. 22, no.2, pp.025008, 2012.

[27] Fang, Z., Guo, X., Xu, L. and Zhang, H., "Experimental study of damping and energy regeneration characteristics of a hydraulic electromagnetic shock absorber," *Advances in Mechanical Engineering*, vol. 5, pp. 943528, 2013.

[28] Xu, L., Liu, Y., Guo, S., Guo, X. and Zuo, L., "Damping characteristics of a hydraulic electric rectifier shock absorber and its effect on vehicle dynamics," *In ASME 2015 International Design Engineering Technical Conferences and Computers and Information in Engineering Conference*, pp. V003T01A009-V003T01A009, 2015.

[29] Zuo, L. and Zhang, P.S., "Energy harvesting, ride comfort, and road handling of regenerative vehicle suspensions", *Journal of Vibration and Acoustics*, vol. 135, no. 1, p.011002, 2013.

[30] Tang, X. and Zuo, L., "Simultaneous energy harvesting and vibration control of structures with tuned mass dampers", *Journal of Intelligent Material Systems and Structure*, vol. 23, no. 18, pp. 2117-2127, 2012.

[31] Lefeuvre, E., Audigier, D., Richard, C., and Guyomar, D., "Buck-Boost Converter for Sensorless Power Optimization of Piezoelectric Energy Harvester," *IEEE Transaction on Power Electronics*, vol. 22, no. 5, pp. 2018–2025, 2007.

[32] Dow, W.G., Fundamentals of Engineering Electronics, Wiley, 1937.

[33] Ni, T., Zuo, L., and Kareem, A., "Assessment of Energy Potential and Vibration Mitigation of Regenerative Tuned Mass Dampers on Wind Excited Tall Buildings," *ASME Design Engineering Technical Conferences*, Washington DC, August 28–31, 2011.

[34] Zhou, K., Doyle, J. C., and Glover, K., "Robust and Optimal Control," Prentice-Hall, Englewood Cliffs, NJ, 1995.

[35] Asami, T., Nishihara, O., and Baz, A. M., "Analytical Solutions to H_∞ and H_2 Optimization of Dynamic Vibration Absorber Attached to Damped Linear Systems," *ASME Journal of Vibration and Acoustics*, vol. 124, pp.67–78, 2002.

[36] Gradshtenyn, I.S., and Ryzhik, I.M., "Table of Integrals Series, and Products", Academic Press, Inc., 1994.

[37] Tang, X., and Zuo, L., "Vibration Energy Harvesting from Random Force and Motion Excitations", *Smart Material and Structures*, vol. 21, no. 7, pp. 075025, 2012.

[38] Zuo, L., and Nayfeh, S.A., "Low order continuous-time filters for approximation of the ISO 2631-1 human vibration sensitivity weightings," *Journal of Sound and Vibration*, vol. 265, no. 2, pp. 459-465, 2003.

[39] Poussot-Vassal, C., Savaresi, S. M., Spelta, C., Sename, O., and Dugard, L., "A methodology for optimal semi-active suspension systems performance evaluation." *Decision and Control (CDC), 49th IEEE Conference on*, pp. 2892-2897, 2010.

[40] Poussot-Vassal, C., Spelta, C., Sename, O., Savaresi, S.M., "Survey and performance evaluation on some automotive semi-active suspension control methods: A comparative study on a single-corner model," *Annual Reviews in Control*, vol. 36, no. 1, pp. 148-160, 2012.

[41] Silveira, M., Wahi, P. and Fernandes, J.C.M. "Effects of asymmetrical damping on a 2 DOF quarter-car model under harmonic excitation," *Communications in Nonlinear Science and Numerical Simulation*, vol. 43, pp.14-24, 2017.

[42] Zuo, L., and Nayfeh, S.A., "Structured H2 optimization of vehicle suspensions based on multi-wheel models," *Vehicle System Dynamics*, vol. 40, no. 5, pp. 351-371, 2003.

[43] Taghirad, H.D., and Esmailzadeh, E., "Automobile passenger comfort assured through LQG/LQR active suspension," *Journal of Vibration and Control*, vol. 4, no. 5, pp. 603-618, 1988.

[44] Hong, K.S., Sohn, H. C., Hedrick, J. K., "Modified Skyhook control of semi-active suspensions: A new model, gain scheduling, and hardware-in-the-loop tuning," *Journal of Dynamic Systems, Measurement, and Control*, vol.124, pp. 158-167, 2002

[45] Zuo, L. and Zhang, P., "Energy harvesting, ride comfort, and road handling of regenerative vehicle suspensions," *Journal of Vibration and Acoustics*, vol. 135, no. 1, pp. 01100, 2013.

[46] Smith, M.C., "Synthesis of mechanical networks: the inerter", *Automatic Control, IEEE Transactions on*, vol. 47, no. 10, pp.1648-1662, 2002.

[47] Smith, M.C. and Wang, F.C., "Performance benefits in passive vehicle suspensions employing inerters", *Vehicle system dynamics*, vol. 42, no. 4, pp.235-257, 2004.

[48] Shigley, J.E., "Shigley's mechanical engineering design", Tata McGraw-Hill Education, 2011.

[49] El Hawary, M.E., "Principles of electric machines with power electronic applications", Prentice Hall, 1986.

[50] Liu, Y. and Zuo, L., "Mixed Skyhook and PDD: a new low-jerk semi-active suspension control based on power flow analysis," *Journal of Dynamic Systems, Measurement, and Control*, vol. 138, no. 8, pp. 081009, 2016.

[51] Sekulić, D. and Dedović, V., "The effect of stiffness and damping of the suspension system elements on the optimisation of the vibrational behaviour of a bus," *International Journal for Traffic and Transport Engineering*, vol. 1, no. 4, pp.231-244, 2011.

[52] Cole, D.J. and Cebon, D., "Truck suspension design to minimize road damage," *Proceedings of the Institution of Mechanical Engineers, Part D: Journal of Automobile Engineering*, vol. 210, no. 2, pp.95-107, 1996.

[53] ISO 8608: Mechanical vibration—Road surface profiles—reporting of measured data, 1995.

[54] Agostinacchio, M., Ciampa, D., and Olita, S., "The vibrations induced by surface irregularities in road pavements–a Matlab approach", *European Transport Research Review*, vol.6, no.3, pp.267-275, 2014.

[55] Sun, L. and Deng, X., "Predicting vertical dynamic loads caused by vehicle-pavement interaction", *Journal of transportation engineering*, vol.124, no. 5, pp.470-478, 1998.

[56] Gillespie, T. and Karamihas, S., "Simplified models for truck dynamic response to road inputs", *International Journal of Heavy Vehicle Systems*, vol. 7, no. 1, pp.52-63, 2000.

[57] Leming, S.K. and Stalford, H.L., "Bridge weigh-in-motion system development using superposition of dynamic truck/static bridge interaction", *Proceedings of the American Control Conference*, Denver, Colorado, pp. 815-820, 2003.

[58] Park, S., Popov, A., and Cole, D., "Influence of soil deformation on off-road heavy vehicle suspension vibration", *Journal of Terramechanics*, vol. 41, no.1, pp. 41-68, 2004.

[59] Sun, L., Cai, X., and Yang, J., "Genetic algorithm-based optimum vehicle suspension design using minimum dynamic pavement load as a design criterion," *Journal of Sound and Vibration*, vol.301, no.(1-2), pp.18-27, 2007.

[60] Belay, A., Obrien, E., and Kroese, D., "Truck fleet model for design and assessment of flexible pavements", *Journal of Sound and Vibration*, vol.311, no. (3-5), pp. 1161-1174, 2008.

[61] Kropáč, O., and Múčka, P., "Effects of longitudinal road waviness on vehicle vibration response," *Vehicle System Dynamics*, vol.47, no.2, pp.135-53, 2009.

[62] Besinger, F., Cebon, D., and Cole, D., "Damper models for heavy vehicle ride dynamics", *Vehicle System Dynamics*, vol. 24, no. 1, pp.35-64, 1995.

[63] Türkay, S., and Akçay, H., "A study of random vibration characteristics of the quarter-car model", Journal of Sound and Vibration, vol. 282, no. (1-2), pp.111-124, 2005.

[64] Madavan, N.K., "Multi-objective optimization using a Pareto differential evolution approach", *IEEE Congress on Evolutionary Computation*, Moffett Field, CA, pp.1145-1150, 2002.

[65] Qin, Y., Dong, M., Langari, R., Gu, L., and Guan, J., "Adaptive hybrid control of vehicle semi-active suspension based on road profile estimation," *Shock and Vibration*, pp.1-13, 2015.

[66] Qin, Y., Dong, M., Zhao, F., Langari, R., and Gu, L., "Road profile classification for vehicle semi-active suspension system based on adaptive neuro-fuzzy inference system", *IEEE 54th Annual Conference on Decision and Control (CDC)*, Osaka, Japan, pp. 1533-1538, 2015

[67] Chen, M.Z., Hu, Y., Li, C. and Chen, G., "Performance benefits of using inerter in semi-active suspensions," *IEEE Transactions on Control Systems Technology*, vol. 23, no. 4, pp.1571-1577, 2015.

[68] Zuo, L., and Nayfeh, S., "Design of passive mechanical systems via decentralized control techniques," *In Proceedings of the 43rd AIAA/ASME/ASCE/AHS/ASC Structures, Structural Dynamics, and Materials Conference*, 2002

[69] Bertsekas, D. P., Nonlinear programming. Belmont: Athena scientific, 1999.

[70] Zuo, L., "Effective and robust vibration control using series multiple tuned-mass dampers," *Journal of Vibration and Acoustics*, vol. 131, no. 3, pp. 031003, 2009

[71] Maciejewski, I., "Control system design of active seat suspensions." *Journal of Sound and Vibration*, vol. 331, no. 6, pp.1291-1309, 2012.

[72] Tseng, H. E. and Hedrick, J. K., "Semi-active control laws-optimal and sub-optimal," *Vehicle System Dynamics*, vol. 23, no. 1, pp. 545-569, 1994.

[73] Zuo, L. and Cui, W., "Dual-functional energy-harvesting and vibration control: electromagnetic resonant shunt series tuned mass dampers," *Journal of vibration and acoustics*, vol. 135, no. 5, pp. 051018, 2013.

[74] Lu, J. b. and Skelton. R. E., "Integrating structure and control design to achieve mixed H_2/H_∞ performance," *International Journal of Control*, vol. 73, no. 16, pp. 1449-1462, 2000.

[75] Nishimura, I., Yamada, T., Sakamoto, M., and Kobori, T., "Control performance of active-passive composite tuned mass damper," *Smart Materials and Structures*, vol.7, no. 5, pp. 637-653, 1998.

[76] Roberts, J.B. and Spanos, P.D., "Random vibration and statistical linearization", New York, 1990.

[77] Adhikari, S., Friswell, M.I., and Inman, D.J., "Piezoelectric Energy Harvesting from Broadband Random Vibrations," *Smart Materials and Structures*, vol.18, no. 11, pp.115005, 2009.

Appendices

Appendix A: MS response integration of a sixth order system

$$I_6 = \int_{-\infty}^{+\infty} \left| \frac{(j\alpha)^5 B_5 + (j\alpha)^4 B_4 + (j\alpha)^3 B_3 + (j\alpha)^2 B_2 + (j\alpha) B_1 + B_0}{(j\alpha)^6 A_6 + (j\alpha)^5 A_5 + (j\alpha)^4 A_4 + (j\alpha)^3 A_3 + (j\alpha)^2 A_2 + (j\alpha) A_1 + A_0} \right|^2 d\alpha = \frac{\pi}{A_6} \frac{Num_6}{Den_6} \quad \text{(A.1)}$$

where,

$$Num_6 = -\mathrm{B}_5^2(-\mathrm{A}_6\mathrm{A}_3\mathrm{A}_1\mathrm{A}_0 + \mathrm{A}_6\mathrm{A}_2\mathrm{A}_1^2 - \mathrm{A}_5^2\mathrm{A}_0^2 + 2\mathrm{A}_5\mathrm{A}_4\mathrm{A}_1\mathrm{A}_0 + \mathrm{A}_5\mathrm{A}_3\mathrm{A}_2\mathrm{A}_0 - \mathrm{A}_5\mathrm{A}_2^2\mathrm{A}_1 - \mathrm{A}_4^2\mathrm{A}_1^2 - \mathrm{A}_4\mathrm{A}_3^2\mathrm{A}_0 + \mathrm{A}_4\mathrm{A}_3\mathrm{A}_2\mathrm{A}_1) + \mathrm{A}_6(\mathrm{B}_4^2 - 2\mathrm{B}_3\mathrm{B}_5)(\mathrm{A}_4\mathrm{A}_1^2 + \mathrm{A}_3^2\mathrm{A}_0 - \mathrm{A}_1\mathrm{A}_2\mathrm{A}_3 - \mathrm{A}_0\mathrm{A}_1\mathrm{A}_5) - \mathrm{A}_6(\mathrm{B}_3^2 - 2\mathrm{B}_2\mathrm{B}_4 + 2\mathrm{B}_1\mathrm{B}_5)(-\mathrm{A}_6\mathrm{A}_1^2 - \mathrm{A}_5\mathrm{A}_3\mathrm{A}_0 + \mathrm{A}_5\mathrm{A}_2\mathrm{A}_1) + \mathrm{A}_6(\mathrm{B}_2^2 - 2\mathrm{B}_1\mathrm{B}_3 + 2\mathrm{B}_0\mathrm{B}_4)(\mathrm{A}_6\mathrm{A}_3\mathrm{A}_1 + \mathrm{A}_5^2\mathrm{A}_0 - \mathrm{A}_5\mathrm{A}_4\mathrm{A}_1) + \mathrm{A}_6(2\mathrm{B}_0\mathrm{B}_2 - \mathrm{B}_1^2)(\mathrm{A}_6\mathrm{A}_5\mathrm{A}_1 - \mathrm{A}_6\mathrm{A}_3^2 - \mathrm{A}_5^2\mathrm{A}_2 + \mathrm{A}_3\mathrm{A}_4\mathrm{A}_5) + \frac{\mathrm{A}_6}{\mathrm{A}_1}\mathrm{B}_0^2(\mathrm{A}_6^2\mathrm{A}_1^2 + \mathrm{A}_6\mathrm{A}_5\mathrm{A}_3\mathrm{A}_0 - 2\mathrm{A}_6\mathrm{A}_5\mathrm{A}_2\mathrm{A}_1 - \mathrm{A}_6\mathrm{A}_4\mathrm{A}_3\mathrm{A}_1 + \mathrm{A}_6\mathrm{A}_3^2\mathrm{A}_2 - \mathrm{A}_5^2\mathrm{A}_4\mathrm{A}_0 + \mathrm{A}_5^2\mathrm{A}_2^2 + \mathrm{A}_5\mathrm{A}_4^2\mathrm{A}_1 - \mathrm{A}_2\mathrm{A}_3\mathrm{A}_4\mathrm{A}_5) \quad \text{(A.2)}$$

$$Den_6 = A_0^2A_5^3 + 3A_0A_1A_3A_5A_6 - 2A_0A_1A_4A_5^2 - A_0A_2A_3A_5^2 - A_0A_3^3A_6 + A_0A_3^2A_4A_5 + A_1^3A_6^2 - 2A_1^2A_2A_5A_6 - A_1^2A_3A_4A_6 + A_1^2A_4^2A_5 + A_1A_2^2A_5^2 + A_1A_2A_3^2A_6 - A_1A_2A_3A_4A_5 \quad \text{(A.3)}$$

The integral in (A.1) can also be expressed in a more elegant form using the determinant of certain matrices, which can be derived following the method in [76-77].

Appendix B: H_2 state-feedback controller design for a LTI system [34]

Theorem 1: Given a LTI system (6.7) with the following assumptions:

$(\tilde{A}, \tilde{B}_u)$ is stabilizable; (B.1)

$\widetilde{D}_{\mathrm{u}}$ has full column rank; (B.2)

$$\begin{bmatrix} \tilde{A} - j\omega I & \tilde{B}_{\mathrm{u}} \\ \tilde{\mathrm{C}} & \widetilde{D}_{\mathrm{u}} \end{bmatrix} \text{ has full column rank for all } \omega; \tag{B.3}$$

The H_2 norm from $\tilde{w}$ to $\tilde{z}$ of system (7) is minimized to

$$J(\tilde{F}) = \|H_{\tilde{z}\tilde{w}}\|_2^2 = trace(\tilde{B}_w{}' K \tilde{B}_w) \tag{B.4}$$

with a state-feedback controller of the form in (8), where the state-feedback gain is

$$\tilde{F} = -\left(\widetilde{D}_u{}' \widetilde{D}_u\right)^{-1} (\tilde{B}_u{}' K + \widetilde{D}_u{}' \tilde{C}) \tag{B.5}$$

where K is subjected to the algebraic Riccati equation

$$\begin{aligned} &\left(\tilde{A} - \tilde{B}_u \left(\widetilde{D}_u{}' \widetilde{D}_u\right)^{-1} \widetilde{D}_u{}' \tilde{C}\right)' K + K \left(\tilde{A} - \tilde{B}_u \left(\widetilde{D}_u{}' \widetilde{D}_u\right)^{-1} \widetilde{D}_u{}' \tilde{C}\right) \\ &\quad - K \tilde{B}_u \left(\widetilde{D}_u{}' \widetilde{D}_u\right)^{-1} \tilde{B}_u{}' K + \tilde{C}' \left(I - \widetilde{D}_u \left(\widetilde{D}_u{}' \widetilde{D}_u\right)^{-1} \widetilde{D}_u{}'\right) \tilde{C} = 0 \end{aligned} \tag{B.6}$$

Appendix C: H_2 Output-feedback controller design for a LTI system [34]

Theorem 1: Given a LTI system (6.32) with the following assumptions:

$$(\tilde{A}, \tilde{B}_u) \text{ is stabilizable and } (\tilde{C}_2, \tilde{A}) \text{ is detectable;} \tag{C.1}$$

$$\widetilde{D}_u \text{ has full column rank and } \widetilde{D}_w \text{ has full row rank;} \tag{C.2}$$

$$\begin{bmatrix} \tilde{A} - j\omega I & \tilde{B}_u \\ \tilde{C}_1 & \widetilde{D}_u \end{bmatrix} \text{ has full column rank for all } \omega; \tag{C.3}$$

$$\begin{bmatrix} \tilde{A} - j\omega I & \tilde{B}_w \\ \tilde{C}_2 & \widetilde{D}_w \end{bmatrix} \text{ has full row rank for all } \omega; \tag{C.4}$$

The H_2 norm from $\widetilde{w}$ to $\tilde{z}$ of system (6.32) is minimized to

$$J\left(\tilde{A}_k, \tilde{B}_k, \tilde{C}_k, \widetilde{D}_k\right) = \|H_{\tilde{z}\widetilde{w}}\|_2^2 = trace\left(\tilde{C}_1 S \tilde{C}_1{}'\right) + trace(\widetilde{D}_w{}' \widetilde{D}_w \tilde{L}' K \tilde{L}) \tag{C.5}$$

with the output-feedback controller

$$\begin{cases} \dot{\tilde{x}}_k = \tilde{A}_k \tilde{x}_k + \tilde{B}_k \tilde{y} \\ \tilde{u} = \tilde{C}_k \tilde{x}_k + \widetilde{D}_k \tilde{y} \end{cases} \tag{C.6}$$

where

$$\begin{cases} \tilde{A}_k = \tilde{A} + \tilde{B}_u \tilde{F} + \tilde{L} \tilde{C}_2 \\ \tilde{B}_k = -\tilde{L} \\ \tilde{C}_k = \tilde{F} \\ \widetilde{D}_k = 0 \end{cases} \tag{C.7}$$

$\tilde{F}$ and K are obtained by Equation (A5) and (A6). The observer gain $\tilde{L}$ is constructed as

$$\tilde{L} = -(S\tilde{C}_2{}' + \tilde{B}_w \widetilde{D}_w{}')\left(\widetilde{D}_w{}' \widetilde{D}_w\right)^{-1} \tag{C.8}$$

where S is subjected to the algebraic Riccati equation

$$\begin{aligned} &\left(\tilde{A} - \tilde{B}_w \widetilde{D}_w{}' \left(\widetilde{D}_w{}' \widetilde{D}_w\right)^{-1} \tilde{C}_2\right) S + S \left(\tilde{A} - \tilde{B}_w \widetilde{D}_w{}' \left(\widetilde{D}_w{}' \widetilde{D}_w\right)^{-1} \tilde{C}_2\right)' \\ &-S\tilde{C}_2{}' \left(\widetilde{D}_w{}' \widetilde{D}_w\right)^{-1} \tilde{C}_2 S + \tilde{B}_w \left(I - \widetilde{D}_w{}' \left(\widetilde{D}_w{}' \widetilde{D}_w\right)^{-1} \widetilde{D}_w\right) \tilde{B}_w{}' = 0 \end{aligned} \tag{C.9}$$